Departamento de Ingeniería Informática y Telecomunicación
Escuela Politécnica Superior
Universidad Autónoma de Madrid

Registration and 3D Reconstruction of Histological Sections: Application to Mammary Gland Development

Presentada por: Ignacio Arganda-Carreras
Dirigida por: Dr. D. Carlos Ortiz-de-Solorzano y Dr. D. José María Carazo

Para la obtención del grado de
Doctor en Informática y Telecomunicación
por la Universidad Autónoma de Madrid
Escuela Politécnica Superior
Cantoblanco, Madrid, España
Mayo 2009

Contents

To my beloved parents,
brother and sister.

Agradecimientos

"Cuando uno está agradecido por algo demasiado bueno para un simple gracias, escribir es menos insatisfactorio que hablar - así al menos no escucha cuán inadecuadas son las palabras."

George Eliot

La mayoría de las tesis doctorales se extienden en el tiempo, ésta además lo hizo en el espacio. Han sido muchos los lugares recorridos y muchas las personas conocidas, así que espero no dejarme a nadie por agradecer y que se me sepa perdonar si eso sucede.

En primer lugar quiero dar las gracias a Carlos Ortiz-de-Solorzano, mi director de tesis. Carlos me embarcó en este viaje en el que ha sido mi guía y, puedo decirlo con mucho orgullo, mi amigo. Todavía tiene que explicarme cómo encaja un informático recién licenciado que habla francés y sabe de Inteligencia Artificial en su perfil de informático que habla inglés y se maneja en el campo de tratamiento de imagen... Sólo espero haber estado a la altura de sus expectativas.

También quiero agradecer a mi co-director de tesis, José María Carazo, y a mi tutor en la escuela, Roberto Marabini, por toda su confianza y apoyo desde la Unidad de Biocomputación del CNB.

Los primeros desarrollos y experimentos de este trabajo de tesis tuvieron lugar en el Ortiz-de-Solorzano's lab del Lawrence Berkeley National Laboratory (Berkeley, CA). Todos los miembros del grupo contribuyeron enormemente al trabajo, tanto en su aspecto biológico como informático. Especialmente, Rodrigo Fernández-González, que fue un hermano mayor para mí y me enseñó todo lo que necesitaba saber para desenvolverme tanto en el laboratorio como con el nuevo idioma y la nueva ciudad. Siempre estuvo (y aún

está) ahí cuando lo necesito, dispuesto a ayudarme con una sonrisa. Nunca podré estarle lo suficientemente agradecido. Ouahiba Laribi, Cris Luengo, Abbey Hartland y Adam Idica hicieron mi vida de expatriado muy sencilla, dentro y fuera del laboratorio.

Carlos Óscar S. Sorzano y Jan Kybic son los responsables de que me sumergiera en el mundo de las B-splines y el registro elástico de imágenes. Jan me acogió gentilmente durante tres meses en su laboratorio en Praga, donde aprendí muchísimo y disfruté trabajando con él y sus estudiantes, Jan Petr y Juan David García-Arteaga, dos personas maravillosas que guardo como amigos. Carlos Óscar es sencillamente un genio con alma de comediante malagueño del que siempre tendré cosas que aprender. Él me animó a continuar su trabajo de registro de imágenes y nunca ha parado de ayudarme con cualquier aspecto técnico de la tesis.

Parte del trabajo también se desarrolló durante diferentes estancias en el nuevo grupo de Carlos, la Unidad de Morfología e Imagen del CIMA, en la Universidad de Navarra, donde Ignacio Fernández-García siempre guarda un chiste en la manga para alegrar el día. Thomas Pengo y Xabier Artaechevarría compartieron conmigo sus conocimientos y experiencias como ingenieros en un grupo bio-médico y juntos aprendimos a sobrevivir en una ciudad pequeña. Arrate Muñoz-Barrutia ha colaborado conmigo desde que la conocí en 2006 y ha sido siempre un gran apoyo a nivel técnico y humano. Es tan buena científica como persona, y puedo decir sin equivocarme que es de las mujeres más inteligentes que conozco.

Quiero dar las gracias también al grupo de Biocomputación del CNB, al que he pertenecido durante todo el periodo del doctorado. A los que están y a los que estuvieron: Mónica, Natalia, Javi, Jesús, Yacob, Roberto, Carmen, Sjors, Isa, Marta, Joan, Federico, Johan, Rocío, José Ramón... ¡A todos! Y en especial a Ana, mi compañera en el "exilio" de la Escuela Politécnica, que me ha tenido que sufrir cada día desde el otro lado de la mesa y a la que extrañaré allá donde vaya. No quiero olvidarme de María y Blanca, ex secretaria y secretaria del grupo, que han hecho siempre desde el cariño que cada uno de mis viajes y papeleos fueran más sencillos, y que son el auténtico motor de la unidad.

En la Escuela Politécnica conté con el apoyo de excelentes personas y profesionales. Con los miembros del Grupo de Tratamiento de Imágenes (Chema, Juan Carlos, Álvaro, Javi, Víctor, etc.) compartimos más que un laboratorio. Carlos del Cacho ha estado siempre ahí, dentro y fuera de la escuela. Daniel y José Miguel Hernández-Lobato aguantan con paciencia infinita todas mis consultas técnicas y todavía no me han reprochado que les convenciera para hacer al doctorado. Iván Dotú, Manuel Cebrián y Manuel

García-Herranz me acostumbraron demasiado bien a desahogarme en frente de un café. Las secretarias del departamento, Juana Calle y Marisa Moreno, son un ejemplo de trabajo bien hecho, eficiencia e implicación, y encima han acabado por conocernos a todos los estudiantes de doctorado.

En el último año he tenido la fortuna de entrar a formar parte del grupo de colaboradores de *Fiji*[1], de lo que estaré eternamente agradecido a Albert Cardona y Johannes Schindelin. Ellos son los responsables de que extendiera mis métodos al mundo de la neurociencia y del código abierto, y, en general, de que no me volviera loco con Java. No quiero dejar de dar las gracias por su ayuda a los demás "fijiers", especialmente a Benjamin Schmid (responsable del maravilloso *ImageJ 3D viewer*[2]) y a los Stephan, Saalfeld y Preibisch, con los que es siempre un placer programar, aunque sea hasta altas horas de la noche y con cervezas de por medio.

Aprovecho esta sección del documento para dedicar de forma más personal el trabajo de todos estos años:

En primer lugar, se lo dedico a mis padres, Carmen y Justo, y a mis hermanos, Ernesto y Sara. Espero que os haga sentir la mitad de orgullosos de lo que yo me siento de vosotros.

Al resto de mi familia, en especial a mis tíos Ana y Tito, mis abuelos Paquito y Lala, mi super-primo Jorge y mi segunda madre Esther y Manolo, que por tenerme más cerca han sufrido y disfrutado conmigo de todos los diferentes momentos que conlleva un trabajo de investigación como este. Paquito, creo que sin tu labor de abuelo-chófer, esta tesis no habría sido nunca posible...

A todos mis amigos, de aquí, de allí y de un poco más allá. Al grupo de estudiantes internacionales y amigos de Berkeley: Óscar (que vino con Carlos), Yalda, Akiko, Stefan, Meti, Medya, Mario, Giulia, Carles, Cèline, Mona, Raquel, Antonio, tantos... A Gilda, que fue mi soporte durante los primeros años. A los amigos de Praga: Jeff, Mattia, Sophie... Los de Pamplona: Iban, David, Mikel... Mis amigos de Sanse, los de toda mi vida: Rubén, Sergio, Diego, Manolo, Juanjo, Carratalá, Alba, David... Los del departamento de Ernesto: Nico, Luisfer, Alberto, Jose... Los del de Sara: Marta (cuántas cosas te debo...), Bea, Alfonso, Amanda, Judith (mi intercambio Rantanplán), Ileana, Santi... A los del piso: Pamela, Matteo, Marta, Lucía y sobre todo, a Ana, la persona más generosa que conozco y que me regaló un sitio fantástico para vivir, en su propia casa... A Helenita, que me acompañó en este camino hasta hace poco y sufre más que yo cuando

[1] `http://pacific.mpi-cbg.de/wiki/index.php/Main_Page`
[2] `http://132.187.25.13/home/?category=Download&page=Viewer3D`

me rechazan un artículo. A Vicente, Borja y Andrea, cómo voy a echar de menos nuestras cenas de domingo viendo series y divagando sobre lo divino y lo humano... A Noe que se nos fue a Mallorca. A Marta y Sergi, mis referencias de todos los días, mi segundo aliento... Todos y todas han contribuido con su ánimo y su cariño a que yo esté aquí ahora escribiendo estas líneas.

A todos ellos y ellas, gracias.

Ignacio Arganda Carreras, en Madrid, mayo de 2009

Acknowledgments

"When one is grateful for something too good for common thanks, writing is less unsatisfactory than speech - one does not, at least, hear how inadequate the words are."

George Eliot

All PhD thesis tend to go on longer time than expected, this one got longer in space too. There have been many places and many people, so I hope to mention everyone and to be forgiven if that does not happen.

First of all, I would like to thank Carlos Ortiz-de-Solorzano, my thesis advisor. Carlos boarded me in this travel where he has been my guide and, I can proudly say, my friend. He still has to explain me how a freshly graduated computer scientist, French-speaker and with some knowledge of Artificial Intelligence fits in his idea of computer scientist, English-speaker and Image Processing expert... I just hope to have fullfilled his expectations.

I would like to thank as well my thesis co-advisor, José María Carazo, and my tutor at the school, Roberto Marabini, for all their trust and support from the Biocomputing Unit at the CNB.

The first developments and experiments of this thesis work took place in the Ortiz-de-Solorzano's lab at the Lawrence Berkeley National Laboratory (Berkeley, CA). All group members contributed to the work in both its biological and computing sides. Especially Rodrigo Fernández-González, who was like an older brother to me and taught me everything I needed to know to cope with the lab, the new language and the new city. He was (and is still) there whenever I need him, always willing to help with a smile. I will always be grateful to him. Ouahiba Laribi, Cris Luengo, Abbey Hartland and Adam Idica made my expat life very easy, inside and outside the lab.

Carlos Óscar S. Sorzano and Jan Kybic are responsible for me diving into the world of B-splines and elastic image registration. Jan gently hosted me for three months in his lab in Prague, where I learned a lot and enjoyed working with him and his students, Jan Petr and Juan David García-Arteaga, two wonderful people I still keep as friends. Carlos Óscar is simply a genius with Malagueno comedian soul from who I will always have something to learn. He encouraged me to go on with his work on image registration and he has never stopped helping me with any technical aspect of my thesis.

Part of this work was developed during different stays in the new Carlos' group, the Cancer Imaging group at CIMA, in Navarra University, where Ignacio Fernández-García always had a joke to cheer everyone up. Thomas Pengo and Xabier Artaechevarría shared with me their knowledge and experience as Engineers in a biomedical lab and together we learned how to survive in a small town. Arrate Muñoz-Barrutia has collaborated with me since I met her in 2006 and has always been of great technical and human support. She is as good scientist as person, and I can say without error she is one of the most intelligent women I ever met.

I would like to thank everyone from the Biocomputing Unit at the CNB, my Spanish group during all the PhD period. Everyone who is or was there: Mónica, Natalia, Javi, Jesús, Yacob, Roberto, Carmen, Sjors, Isa, Marta, Joan, Federico, Johan, Rocío, José Ramón... Everyone! And especially Ana, my "exile"-mate at the polytechnic school, who suffered me from the other side of the table and who I will miss whenever I go. I do not want to forget María and Blanca, the group secretaries, who always carefully made my trips and paper work very simple, and are the true engine of the group.

At the polytechnic school I had the support of excellent people and professionals. With the Image Processing group (Chema, Juan Carlos, Álvaro, Javi, Víctor, etc.) we shared more than just a lab. Carlos del Cacho was always there, inside and outside the school. Daniel and José Miguel Hernández-Lobato have infinite patience to answer each of my technical questions and they haven't complained yet for me convincing them to join the PhD program. Iván Dotú, Manuel Cebrián and Manuel García-Herranz got me used to take my frustration out in front of a coffee. The Computer Science department secretaries Juana Calle and Marisa Moreno are an example of work well done, efficiency and involvement, and above all of that, they managed to know all the PhD students in the department.

Last year I luckily joined the group of *Fiji*[3] collaborators, for what I will be always grateful to Albert Cardona and Johannes Schindelin. They are

[3] `http://pacific.mpi-cbg.de/wiki/index.php/Main_Page`

responsible for me extending my methods to the world of Neuroscience and open source code, and, in general terms, for me not getting crazy with Java. I would like to thank too the rest of "fijiers" for their help, especially Benjamin Schmid (the father of the wonderful *ImageJ 3D viewer*[4]) and the Stephan, Saalfeld and Preibisch, with whom it is always a pleasure to program, even at late night and with some beers.

I would like to take advantage of this section of the document to dedicate in a more personal way the work of all these years:

First of all, I dedicate it to my parents, Carmen and Justo, and to my siblings, Ernesto and Sara. I hope this thesis will make you feel at least half of proud I feel of you.

To the rest of my family and especially to my uncle and aunt, Tito and Ana, my grandparents, Paquito and Lala, my super cousin Jorge, my "second mother" Esther, and Manolo, who were closer to me and consequently suffered and enjoyed with me the different moments of such a research work. Paquito, I think this thesis would have never been possible without your grandpa-driver work...

To all my friends, from here, from there and from a little bit farther. To the troop of international students and friends in Berkeley: Óscar (who came with Carlos), Yalda, Akiko, Stefan, Meti, Medya, Mario, Giulia, Carles, Cèline, Mona, Raquel, Antonio, so many... To Gilda, who was my support during the first years. To my Prague friends: Jeff, Mattia, Sophie... To the Pamplona ones: Iban, David, Mikel... To my Sanse friends, the lifelong ones: Rubén, Sergio, Diego, Manolo, Juanjo, Carratalá, Alba, David... To the friends in Ernesto's department: Nico, Luisfer, Alberto, Jose... To the ones at Sara's: Marta (how many things I owe you...), Bea, Alfonso, Amanda, Judith (my Rantanplan exchange), Ileana, Santi... To my flatmates: Pamela, Matteo, Marta, Lucía and especially to Ana, the most generous person I know, who gave me a fantastic place to live, in her own house... To Helenita, who shared this path with me until not too long ago and still suffers more than me when I get a paper rejected. To Vicente, Borja and Andrea, how much I'm going to miss our Sunday dinners watching series and wandering about the divine and the human... To Noe, who left to Mallorca. To Marta and Sergi, my everyday references, my second breath... Everyone contributed with his or her affection and encouragement to bring me to this point.

To all of them, thanks.

Ignacio Arganda-Carreras, in Madrid, May 2009

[4] `http://132.187.25.13/home/?category=Download&page=Viewer3D`

Resumen

"Dígame Sr Hoover, ¿cuáles son sus intereses?

Señora, soy ingeniero.

¿En serio? Le había tomado por un caballero."

Herbert Hoover

En el campo del procesamiento de imagen médica, los datos volumétricos generados por métodos de microscopía 3D como resonancia magnética (MRI en sus siglas en inglés), tomografía por emisión de positrones (PET en sus siglas en inglés) y tomografía axial computarizada (CT en sus siglas en inglés) presentan extensas aplicaciones en la visualización y el análisis de órganos. Los métodos de tratamiento de imagen 2D, como por ejemplo la microscopía óptica, generan típicamente series de secciones con una resolución mucho más alta que los escáners de MRI o CT. La reconstrucción tridimensional de esas secciones bidimensionales se ha convertido por lo tanto en una herramienta importante para el estudio de las esctructuras anatómicas en 3D. La principal motivación de este trabajo de tesis es la necesidad de métodos eficientes y automáticos para la reconstrucción de muestras gruesas de tejido desde secciones histológicas teñidas.

La mayoría de los algoritmos que se presentan en este manuscrito, y que son de hecho la principal contribución de esta tesis, están enmarcados en *R3D2*, un sistema para el análisis morfológico y molecular simultáneo de muestras de tejido grueso (Fernandez-Gonzalez et al., 2002; Fernandez-Gonzalez, 2006). Este sistema completamente integrado se compone de un microscopio de campo claro asistido por ordenador y una aplicación JAVA de visualización y análisis que permite una eficiente adquisición, alineamiento,

anotación, reconstrucción tridimensional y ánalisis de las estructuras de interés en secciones gruesas de tejido de diferentes especímenes.

Las principales líneas de trabajo de esta tesis son el **registro de imágenes** y la **reconstrucción 3D**. El registro de imágenes se refire aquí al proceso de transformación de diferentes conjuntos de datos —secciones histológicas en nuestro caso— para llevarlos al mismo sistema de coordenadas. Para lectores interesados es muy recomendable el estudio detallado del campo que llevan a cabo en su artículo Zitová and Flusser (2003). Por lo tanto este proceso, y de hecho nos referiremos a él de este modo en algunos momentos de la tesis, puede llamarse también alineamiento de imágenes. Además, dado el interés general existente en el campo de la Biomedicina hacia los métodos de alinemiento de imágenes, hemos extendido uno de nuestros nuevos métodos de registro de pares de secciones histológicas para poder registrar secuencias enteras de imágenes 2D de todo tipo.

La tesis está organizada del siguiente modo: en el Capítulo 2 se presentan nuevos métodos para el alineamiento de secciones histológicas, primero con una transformación global de cuerpo rígido y después con un refinamiento local basado en la correlación de las imágenes. El Capítulo 3 describe un nuevo método para el alineamiento no lineal de pares de imágenes. El Capítulo 4 extiende el método no lineal para pares de imágenes descrito en el capítulo anterior para alinear secuencias de imágenes 2D. Finalmente, en el Capítulo 5 se presenta el protocolo completo para producir reconstrucciones tridimensionales de secciones histológicas y se muestran diferentes aplicaciones sobre muestras de tejido de glándula mamaria completa..

1 Introduction

"Tell me, Mr Hoover, what are your interests?
Madam, I am an Engineer.
Really? I took you for a gentleman."

Herbert Hoover

1.1 3D data

In medical imaging, volumetric data generated by 3D microscopy methods such as magnetic resonance imaging (MRI), positron emission tomography (PET) and computed tomography (CT) have wide applications in the visualization and analysis of organs. 2D imaging methods, such as optical microscopy, typically generate serial sections with much higher resolution than MRI or CT scans. The 3D reconstruction of these 2D sections has therefore become an important tool for understanding anatomical structures in 3D. The main motivation of this work is the need for efficient and automatic methods to reconstruct thick tissue samples from stainned histological sections.

1.2 R3D2

Most of the algorithms presented in this manuscript —which are indeed the main contribution of this thesis— are framed in *R3D2*, a system for simultaneous morphological and molecular analysis of thick tissue samples

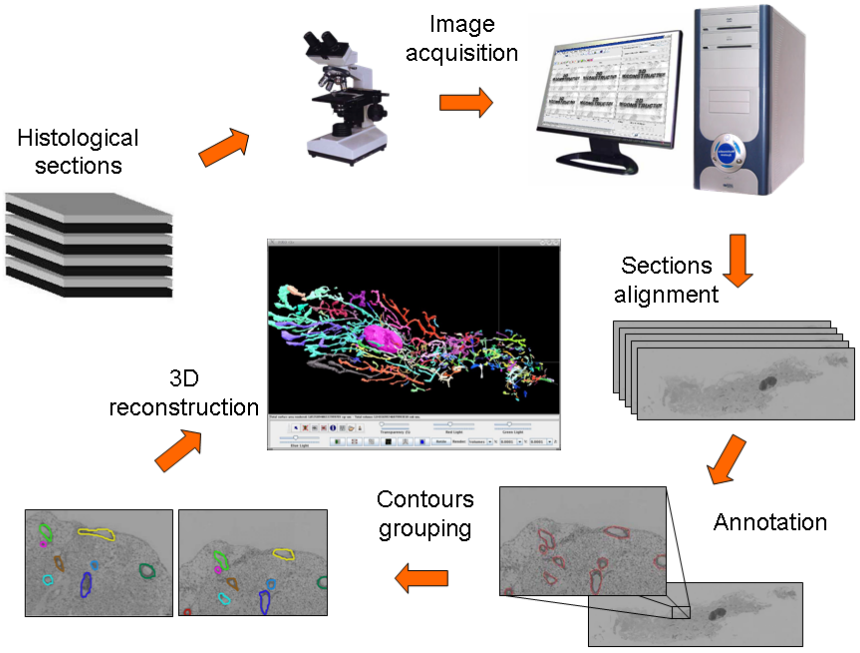

Figure 1.1: 3D reconstruction protocol. The different steps (sectionnig, acquisition, alignment, annotation, markings grouping and reconstruction) are illustrated.

(Fernandez-Gonzalez et al., 2002; Fernandez-Gonzalez, 2006). This completely integrated system is composed of a computer-assisted microscope and a JAVA-based image display, analysis, and visualization program that allows efficient acquisition, alignment, annotation, three-dimensional reconstruction, and analysis of structures of interest in thick sectioned tissue specimens. Figure 1.1 shows a graphical explanation of the protocol followed by the system.

1.3 Objetives of this thesis

The main lines of this thesis work are **image registration** and **3D reconstruction**. Image registration refers to the process of transforming different sets of data —histological sections in our case— into the same coordinate system. We recommend the survey article by Zitová and Flusser (2003) for

a detailed overview. Thus this process can also be called image alignment. Furthermore, and given the general interest in Biomedicine in image alignment methods, we extended one of our novel methods for registering pairs of histological sections to register whole sequences of 2D images of any sort.

This manuscript is organized as follows. Chapter 2 presents new methods to align histological sections, first with a global rigid-body transformation and then with a local correlation-based refinement. Chapter 3 describes a new method for nonlinear registration of image pairs. Chapter 4 extends the nonlinear pairwise registration method described in the previous chapter to align 2D image sequences. Finally, Chapter 5 presents the complete protocol to produce three-dimensional reconstructions from serial sections and shows different applications using mammary gland tissue samples.

2

Rigid and Local Registration

"Computer Science is no more about computers than astronomy is about telescopes."

Edsger W. Dijkstra

Abstract

We present a method for automatically registering 2D images of histological serial sections. This method combines two independent algorithms. The first one consists of a hierarchical, multi-resolution rigid body registration. The second uses non-linear local correlation-based registration to refine the result of the previous algorithm. Both methods present two variants, one that is applied to the gray scale images and makes use of the entire image information, and another one that reuses the result from the segmentation of the most relevant structures in the image. These methods could be applied independently, although are more effective when combined. In this chapter we present the algorithms and evaluate their performance by registering fully sectioned tissue biopsies of human mammary gland and breast cancer tissue samples.

2.1 Introduction and Antecedents

Histological tissue sections are the main source of information in diagnostic Pathology. By carefully evaluating the morphology of the tissues at different levels of resolution, the Pathologist can detect changes in the architecture of

the tissue and relate them to their likely causes. Observing the morphology of the tissue requires appropriate tissue processing and staining. Namely, to preserve the morphology of the anatomical structures, the tissue is first fixed to eliminate autolytic enzymes and avoid bacterial decomposition. After fixation, the tissue is usually embedded in a rigid or semirigid material that gives consistency to the tissue, and allows cutting it into thin slices. Paraffin is the most commonly used embedding product. After embedding, the tissue is cut into thin slices using a microtome. The sections are then attached to glass slides using a mounting agent such as grenetine. The slices dry off and the grenetine works as a tissue adhesive. Then the slides are stained to allow visualization of structures of interest. The user can choose among several staining methods, depending on the tissue source and the structures being observed. Hematoxylin and Eosin (H&E) staining, which labels both the nuclei an cytoplasm of the cells is routinely used when combined architectural and cell level morphological information is required.

To this date, the pathological study of the tissue structure is done in two dimensions, by observing the tissue using a conventional microscope. This causes a loss of the tissue's architectural information, which is reduced to flat samples of complex three-dimensional objects. Very rudimentary three-dimensional information can be obtained by observing multiple —consecutive— tissue sections. This method can only provide very gross, simplified information of the actual tissue structures because of the complexity of the most tissues and the limited ability of the human brain to correctly report topological quantitative 3D information.

We believe that a completely three-dimensional visualization and quantification of the tissue, using computer-based reconstruction of the structures of interest, will refine the histo-pathological diagnosis of the tissues, allowing detection of small morphological changes that would be missed using standard two-dimensional analysis. To this end, we developed a computerized microscopy system (Fernandez-Gonzalez et al., 2002) (called *R3D2*) that semi-automates the tasks involved in reconstructing tissue structures from fully sectioned tissue blocks. The system scans entire sections of tissue and provides a set of interactive tools for registering (Arganda-Carreras et al., 1-5 Sept. 2004) and segmenting (Fernandez-Gonzalez et al., 2004) the images of the scans, to then create 3D surface renderings of the structures of interest.

A topologically accurate rendition of the tissue requires all the images of the sections to be correctly registered (i.e. aligned), to ensure the continuity of the structures crossing several sections. Manually registering each pair of sections is a relatively simple task that involves either manually rotating and translating a half-transparent image over the reference image (Haas and Fis-

cher, 1997; Hofstadler-Deiques et al., 2005), or marking sets of corresponding points on both images and calculating the affine transform that aligns the images (Capuco et al., 2002; Fiala, 2005). However, this fully manual approaches become cumbersome when registering completely sectioned tissue blocks, made of hundreds of sections and adds a component of error to the registration, since the user can bias the registration by incorrectly selecting the fiducial points or the corresponding rotation and translation values. Finally, these approaches are not accurate enough since they assume that the registration between consecutive sections is an affine transformation, typical from rigid bodies. However, the preparation steps may introduce non-linear effects that can not be corrected for using an affine transformation as described by Deverell et al. (1989), Schormann et al. (1995) and Brey et al. (2002). Examples of these effects are missing sections and/or non-linear distorting effects, such as tissue folding, stretching, tearing... To add even more difficulty to the registration, the resolution of the images in the vertical directions (i.e. the distance between sections) is considerably lower in this modality than it is in other 3D imaging modalities. This causes substantial differences between the same structures in consecutive sections and consequently, a more complex registration.

In this chapter we present an automatic registration method that addresses those problems, and that has been implemented in a computationally efficient way to fast and accurately register images of consecutive sections of fully sectioned tissue blocks. A full description of the methods applied in this project is given in Section 2.2. Section 2.2.1 describes the image acquisition process and Sections 2.2.2 and 2.2.3 respectively explain the rigid and local registration methods with their two possible variants. The results from both methods are presented in Section 2.3. Finally, the discussion and conclusion are dealt with in Sections 2.4 and 2.5.

2.2 Methodology

2.2.1 Image Acquisition

We used formalin fixed-paraffin embedded tissue blocks, which contained either entire mouse mammary glands or human tissue biopsies of normal breast tissue and breast tumors. The blocks were fully sectioned at 5 micron thickness and each section stained with H&E. The number of sections per block depended on the thickness of the tissue block, ranging from the low tens to the low hundreds. Low-resolution (2.5x magnification) multiple-snapshot images of all the sections were taken using a computed assisted wide

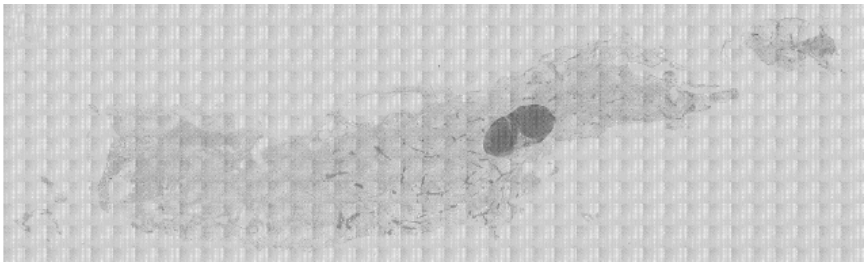

(a)

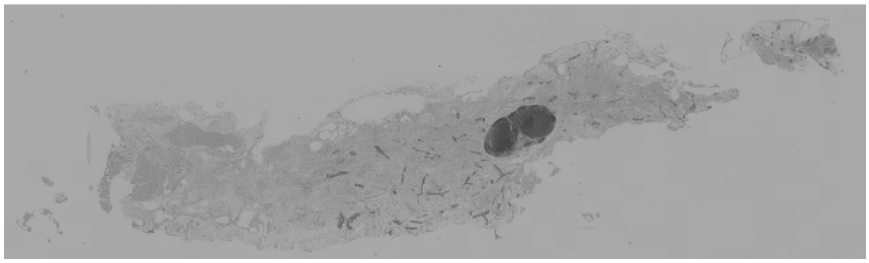

(b)

Figure 2.1: Background correction. 2.1a shows the original image obtained from multiple consecutive snaps shots. 2.1b shows the background corrected version of 2.1a.

field microscope (Fernandez-Gonzalez et al., 2002). The size of the images depended on the size of the tissue sections, typically from 3000×3000 to 5000×5000 pixels. A background correction algorithm was used to correct a mosaic-like effect of the images due to uneven illumination of the field of view of the microscope (see example in Figure 2.1). The sections were saved in either TIFF or ICS (Dean et al., 1990) format (gray scale mode) and grouped in sets of related images that we will refer to as **cases**.

2.2.2 Rigid Registration

A rigid-body registration between two images can be accomplished manually by marking pairs of corresponding points —landmarks— on the images and calculating the rigid-body transformation that minimizes the lineal quadratic distance between the corresponding points of both images. Maurer et al. (1996) demonstrated that the registration error is inversely proportional to the number of fiducial points used to define the transformation. Manually registering all the sections of a entire tissue block could become extremely

tedious when the cases are made of tens to hundreds of sections, even if only a few pairs of points is used to calculate the transformation between each pair of images.

Bossert (2005) proposed a registration method for histological sections where the landmark points are assumed to naturally exist. Therefore, only histological preparations providing nuclei or comparable structures —that extend over several sections and are capable of being extracted using methods of pattern recognition— could be registered by this algorithm.

Two methods appeared recently to automatically extract common features from two images, what could be used for automatic landmarks extraction. These methods are the Scale-Invariant Feature Transform (SIFT) by Lowe (2004) and Multi-Scale Oriented Patches (MOPs) by Brown et al. (2005). However, these methods do not work always on histological sections, since they require a similar histogram in both images, i.e. the same tissue staining, and they are really dependent on the image size and section thickness. Too thick sections make the methods to fail because they are expecting images with very similar objects in different positions.

Automated Image Registration (AIR) by Woods et al. (1998) is an open source collection of C programs and subroutines designed to align images within and across subjects (mainly from positron emission tomography —PET— and magnetic resonance imaging —MRI) and within and sometimes across imaging modalities (PET-MRI). It has been used in some works to register histological sections (Brey et al., 2002). However, it provides a local solution and depends on a set of parameters that need to be tuned for every couple of images. Maes et al. (1997) proposed another method for multimodality image registration on computed tomography (CT), PET and MRI small images (256×256 pixels). They used mutual information or relative entropy as matching criterion and Powell's optimization to find as well a local solution.

Our goal is to automate the rigid-body registration of our large images to achieve a global solution and integrate it in the system. We have done it by combining the original ideas of Borgefors (1988) and Hult (1995), optimized and customized for our histological images. Following them, the automation can be solved using optimization methods over global similarity measures between each pair of images. These similarity measures can be based on the cross-correlation between the images or on distance measures calculated from the structures of interest as defined by the relevant image gradients (Hult, 1995). Due to the large size of the images, we used a hierarchical pyramidal approach to the problem (Borgefors, 1988), by working with different levels of image subsampling. Thus different versions of the images,

of gradually increasing resolution are used. In every level of this pyramid the rigid-body transformation of the source image that better matches the target image is calculated, thus gradually approaching the best registration between the images. In our case, the top of the pyramid corresponds to the most subsampled version of the image, and its bottom to the original image, i.e. the full resolution image. The pyramid has n levels, being 2^{n-1} the subsampling factor on the top level, the first one to be processed, and 2^{i-1} the factor used in the i^{th} level. The start point in each level is the registration result obtained using the previous level. This way the system uses reduced versions of the images thus decreasing significantly memory use. Using subsampled versions of the images introduces an error in the registration that is proportional to the subsampling factor. However, this error decreases in every iteration of the algorithm.

The algorithm used to calculate the optimum registration at each pyramid level (Figure 2.2) works as follows: First both target and source images are subsampled according to the corresponding factor (determined by the pyramid level). Then a Gaussian filter is applied to remove image noise. Next a Sobel operator is applied that calculates 2D gradients of the images, thus detecting the areas with high gradient, which usually correspond to the image edges. To determine the location of the relevant image edges, and create a binary contour map, the images are then binarized applying an auto-thresholding function that assigns white value —255— to the pixels that belong to relevant edges of the images, and black value —0— to all the other pixels. This function is an adaptive threshold based on the work of Otsu (1979). The function sets an initial test threshold value and computes the averages of the pixels below and above this value, and the composite average of both averages. Then the test threshold value is increased iteratively until it is larger than the composite threshold (Rasband, 1997-2009). After thresholding, the distance transform of the target image alone is computed, where pixels corresponding to the edges in the target image will have high pixel values, and the rest of pixels will present gradually smaller values as they are located increasingly and farther from the edges. This is actually the inverse of the classical distance transform, where the pixel values increase with the distance to the edges.

After both target and source images have been processed as described, a matching function is applied between the target image and several rigid-body transformations of the contour image. Let P_c be the set of pixels of the source contour image, P_d the set of pixels of the target distance image, $p_c[i]$ the value of the i^{th} pixel in the contour image and $p_d[j]$ the value of the j^{th} pixel in the distance image. The matching value m of our contour and

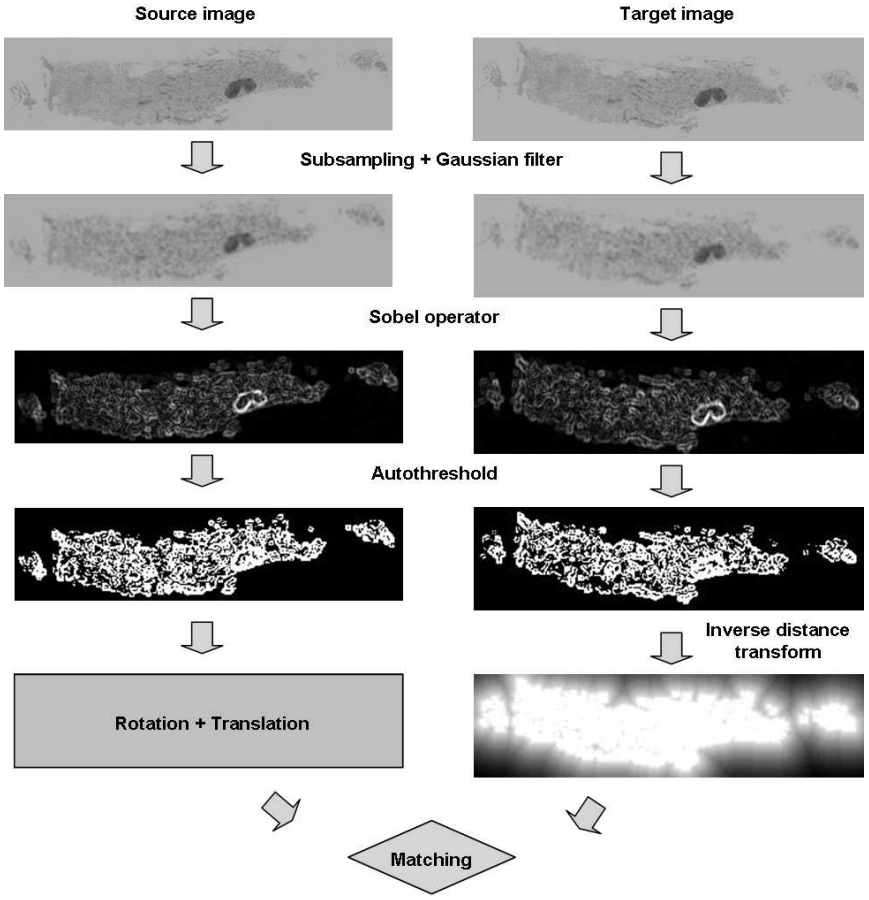

Figure 2.2: Image preprocessing for rigid registration. Both source and target images are subsampled (according to the pyramid level) and filtered with a Gaussian kernel to remove noise, their edges are detected by a Sobel operator, and both images are also binarized by an auto-thresholding function. Then a matching function is applied between the source image after a rigid-body transformation and an inverse distance transform version of the binarized target image.

distance images is defined by

$$m(\alpha, t_x, t_y) = \sum_{p_c[i] \neq 0} p_d[j], \forall p_c \in P_c \tag{2.1}$$

where α, t_x and t_y are the parameters of the rigid transformation applied to the contour image: α is the angle of the rotation, and t_x and t_y are the translations in x- and y- directions. The $(0, 0)$ coordinate for the translations corresponds to the situation where the upper left corner of both images coincides. The value j is the pixel index in the distance image that corresponds to the pixel i in the contour image after applying the rigid-body transformation. Then if pixel i is defined by coordinates $(x_i, y_i, 1)$, the coordinates $(x_j, y_j, 1)$ corresponding to pixel j are calculated by a simple matrix multiplication:

$$\begin{pmatrix} x_j \\ y_j \\ 1 \end{pmatrix} = \begin{pmatrix} cos\alpha & -sin\alpha & t_x \\ sin\alpha & cos\alpha & t_y \\ 0 & 0 & 1 \end{pmatrix} \begin{pmatrix} x_i \\ y_i \\ 1 \end{pmatrix} \tag{2.2}$$

Since not every pair of coordinates in the contour image has a valid pair of coordinates in the distance image after its transformation, the value of the matching function for those coordinates that do not match any pixel in the distance image is set to 0.

Instead of applying all possible rotations and translations to the contour image, to then calculate their matching value, the rotations and translations used depend on the level of the pyramid. This is done to minimize the time used to find the maximum of the matching function. Namely, in the first pyramid level the system checks all possible rotations from $-180°$ to $170°$ in steps of $10°$, performing all possible translations that guarantee at least 50% overlap between contour and distance images, in steps that depend on the image dimensions and resolution. This 50% minimum overlap is achieved by assigning the 25% of the image width and height to the limits in x- and y- translations. Thus the minimum translation value in the x- axis corresponds to -25% the image width and the maximum to $+25\%$ the image width. The same limits apply to the y- direction with the image height. These x and y limits define the space of search for the translations. Since the image is rotated, this space is also transformed in order to preserve the same orientation as the image and guarantee the overlap after the image rotation. The size of the translation steps is determined by the image resolution which is the measure of the pixel information, but also by the image dimensions since an upper limit is imposed in order to avoid large steps in small images.

The maximum of the matching function after trying all possible rotations and translations is then recorded for the pyramid level. The error of this measurement remains under control and will be gradually reduced in the following levels. The alignment (i.e. rotation and translation) that produced the maximum of the matching function in the first pyramid level is then used as the starting point for the second level, where the system reduces the range of translations and rotations to a neighborhood of the previous result. Furthermore, the size of the rotation and translation steps will be decreased in order to refine the previous registration. The neighborhood dimensions are directly related to the size of the steps that were used in the previous level. Thus, if steps of 10° were used in the previous rotation, the new space of search will be a symmetric 20° neighborhood of the best angle obtained in the previous pyramid level. The same rule can be extended to the translation steps taking now into account the correspondent change in the resolution of the image.

The search of the maximum level by level is performed until the error falls under a pre-determined value or until the requested number of pyramid levels is completed. A detailed graphical description of the method is shown in Figure 2.3.

Using this multi-resolution hierarchical algorithm, the best matching is found progressively, by first approaching it by using low-resolution images and large search areas, and then refining it by using high-resolution images and reduced search spaces. Consequently, the reduction of the error in every pyramid level is implicit, since lower levels involve more resolution and therefore more image information. The efficiency of the algorithm is also guaranteed, since the size of the space of search decrease as the size of the subsampled images is increased.

We proposed a variation of the rigid-body registration, called shape rigid registration, which is a natural extension of the method that we just presented. This second method can be used when the images to be registered have been segmented and can be represented as a binary set of contours corresponding to the edges of the structures of interest. Therefore, in the process already described and shown in Figure 2.2, the results of the auto-threshold of the source and target images are replaced by the binary representation of the segmented contours of the images. The rest of the algorithm does not change from what has been already described. This method presents two general advantages over the previous one. First, assuming that the segmented contours correspond only to the relevant structures in the image, the matching between the images will be based only on relevant image information, thus mitigating the effect of noise or artifacts. The second advantage

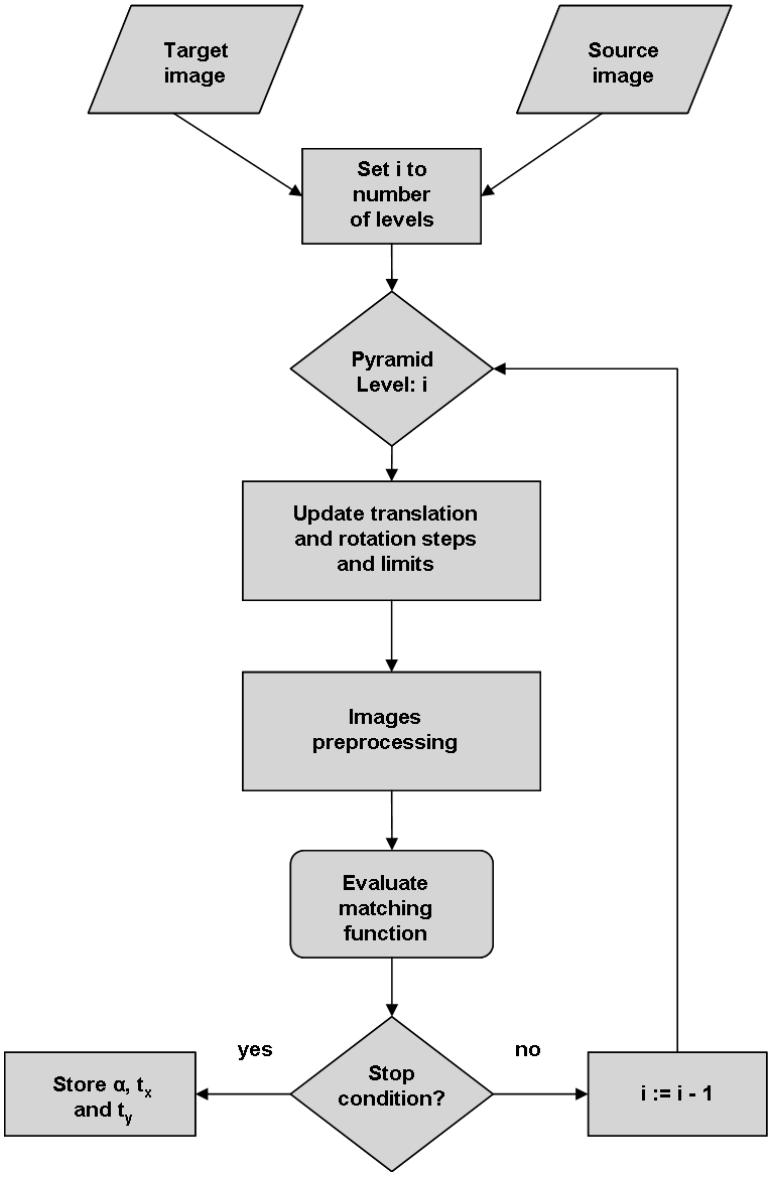

Figure 2.3: Rigid registration algorithm. The method begins by the top of the pyramid and it is iterated until the stop condition is achieved, updating the limits and the steps applied to the rigid-body transformation according to the correspondent pyramid level and the previous parameters.

of this method is its increased efficiency. As the image preprocessing (Figure 2.2) is reduced to the last two steps and the number of multiplications in (2.1) is drastically reduced since most of the pixels in the binary image are black. Memory use can be further reduced by replacing the actual binary images by a chain-code representation of the segmented contours. Figure 2.4 shows the difference between the binary image obtained by the standard rigid registration method and the shape rigid registration method.

Our methods (Arganda-Carreras et al., 1-5 Sept. 2004) parallel the Hierarchical Chamfer Matching Algorithm (HCMA) of Borgefors (1988) and Hult (1995) algorithms. While the HCMA works with the entire grayscale image information but does not specify the way to obtain the contours, Hult method attempts to achieve a binary image containing only the relevant information from the gray scale image, which is ideally the input to HCMA. Both methods begin the search of the optimum registration from predetermined start positions and consequently could converge in local maxima instead of the global maximum of the matching function. Our algorithm (both the standard and the shape-based) instead, guarantees finding a global maximum with an error that is defined by the resolution of the bottom layer of the pyramid.

2.2.3 Local Registration

As already mentioned in the introduction, manual tissue sectioning can produce non-linear deformations in the tissue, such as folding, stretching, tearing... Occasionally also, due to the tissue conditions or improper maintenance of the microtome, some sections can be damaged beyond recovery and have to be disposed, thus introducing gaps in the sequence of sections of the case. All these effects may cause large misalignment between areas of the section that cannot be corrected for solely by applying a global affine transformation. Many non-rigid registration methods have been already proposed in the literature (Dawant, 2002; Lester and Arridge, 1999; Hajnal et al., 2001; Maintz and Viergever, 1998). Specific solutions based on complex transformations, such as elastic registration (Rohr, 2000; Sorzano et al., 2005; Auer et al., 2005) or piecewise registration (Pitiot et al., 2003, 2006), can be too expensive in computation time given the dimensions of the images of our histological sections. Furthermore, this type of methods do not differentiate between what can be consider natural distortions in the tissue —for instance a change in the orientation of a duct— from strong artificial distortions —tissue stretching, folding, etc. Therefore we opted for a local registration solution that can produce accurate results in a reasonable time without

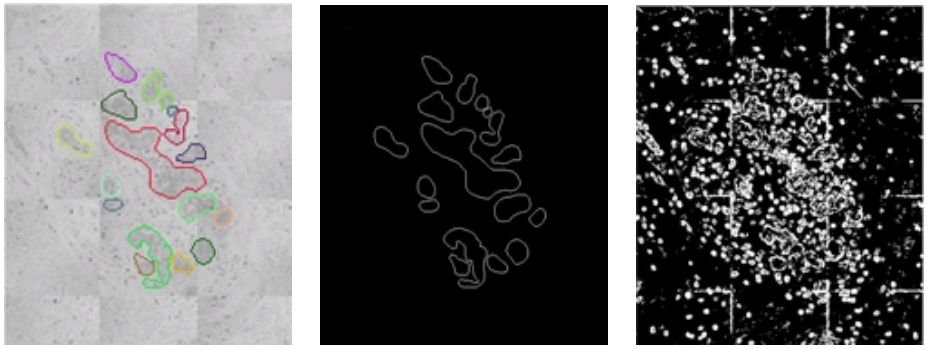

(a) (b) (c)

Figure 2.4: Graphical example of the reduction in complexity of the rigid registration algorithm when using as input a binary image containing only the most representative contours of the structures of interest or containing all the gradient information above a modified Otsu threshold. (2.4a) Histological section image already segmented. The contours from the structures of interest are represented in different colors. (2.4b) Binary image constructed from the contours. (2.4c) Binary image obtained with the pre-processing described in Section 2.2.2 (subsampling and Gaussian filtering, application of the Sobel operator and modified Otsu thresholding).

large image deformations unless they are strictly necessary. The algorithm locally refines the registration in the areas of the structures of interest based on their cross-correlation. This way we preserve the natural deviations on the morphology of the tissue while correcting the misalignments produced during the rigid registration. If the correlation coefficient between the local areas is too large —compared to the average in the group of structures being refined— we substitute the correction vector by the average vector of its neighborhood. Ourselin et al. (2001) proposed a blockmatching strategy that allows to compute local displacements between the sections, but then they collected these local measures to estimate a global rigid transformation, what we already have from the method described in Section 2.2.2.

Our local registration algorithm calculates a common bounding box for area or sub-image of the section and calculates a correction vector for each of these sub-images. The correction vector is calculated using the cross-correlation between the bounding box in the target image and the corresponding bounding box in the source image. This source bounding box is defined from the rigid registration parameters if a previous rigid-body registration has been applied before to the image.

This alignment algorithm uses the Phase Correlation Method (PCM) from Kuglin and Hines (1975), a popular method to calculate translational offsets between images. PCM is based on the Fourier shift theorem which states that a shift between two images results in a linear phase difference in the Fourier transform of both images. Therefore, the correlation between these areas or sub-images can be efficiently calculated in the frequency domain. The result is two new images: modulus and phase. The modulus of the correlation has a peak located a distance that corresponds to the translation of one of the images that would render the best alignment or similarity with the other image. Therefore, the shift vector is obtained by calculating the difference between the coordinates of the center of the image and the coordinates of the brightest peak in the modulus image. A graphical description of this process is shown in Figure 2.5.

Since the dimensions of the sub-images are fixed, parts of one or more structures of interest can belong to different sub-images, causing less accurate results than if the entire structures were inside the same sub-images. Therefore the algorithm makes use of two different window sizes: the sub-image size and the correlation area size. The correlation area is the part of the image centered in the sub-image that is used to calculate the correction vector. Its size must be bigger than the sub-image size in order to avoid the previously mentioned problem. Indeed, this size should equal the estimated maximum error produced during the rigid registration in order to correct the

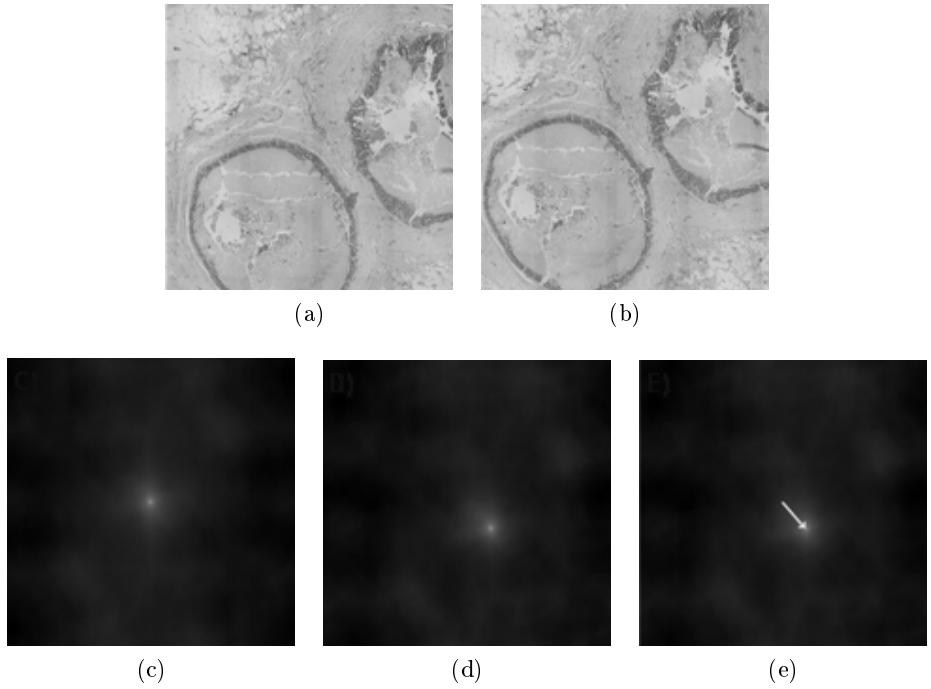

(a) (b)

(c) (d) (e)

Figure 2.5: Image alignment by phase correlation. (2.5a) Selected region of a tissue section. (2.5b) Same region of the tissue section but shifted. (2.5c) Modulus of the autocorrelation image. Note the peak at the image center. (2.5d) Modulus of the cross-correlation between images (2.5a) and (2.5b). Note how the peak is shifted. (2.5e) Correction vector in white.

misalignment introduced in that process.

As in the rigid registration algorithm, the local registration algorithm can be applied to the gray scale image or to the binary image containing only the segmented contours.

At the end of this process there will be a correction vector and a correlation coefficient for every sub-image. The correlation coefficient is calculated between the original reference sub-image and a new target sub-image, which is the result of applying the correction vector to the old target sub-image. Thus the correlation coefficient will provide a measure of the accuracy of the correction vector.

The value of the cross-correlation can be affected by several factors like improper focusing of areas in the same image, differences in the luminosity of the areas, or even the presence of foreign bodies in the tissue. Therefore, two-step filtering is applied to the correction vector list in order to eliminate and recalculate erroneous vectors. The first filter recalculates the vectors whose correlation coefficient lies under a threshold value, that is obtained using the auto-threshold function over the coefficient list. This function is the same one that was used in the rigid registration method, but now applied only to 1D data. The correction vectors that have a low correlation coefficient are then substituted by the average of the vector of a 3×3 neighborhood of the affected window. Thus, vectors with a very low correlation coefficient will not be taken into account. The second filter to be applied to the list of vectors is a mean filter, also with a 3×3 kernel, that will allow smoothing the vector field and reducing the effect of the spurious noise.

2.3 Results

2.3.1 Rigid registration validation

As a first test of the goodness of both standard and shape rigid registration methods, we used synthetic cases, i.e. artificial cases where every section was a rigid-body transformation of the same original section. That allows testing the algorithm's capacity to recover the original alignment and calculating its speed.

A way of qualitatively evaluating the accuracy of the algorithms consists of creating a color image combining both the target and the transformed source image. This color image will have the target image information in the red channel and the source image information in the green channel. The source image was transformed according to the parameters previously obtained in the rigid registration process. That way, overlapping areas will

present yellow color, as it corresponds to aggregation of red and green, while non-overlapping areas will be either green or red. Generating these color images for each pyramid level in the algorithm allow us graphically evaluating the error reduction implicit in each level. Figures 2.6 and 2.7 show this way the results of applying both rigid registration methods to two artificially generated cases.

These synthetic cases were used to empirically calculate the size of the steps to be used in the rigid registration, which depends on the resolution of the images and subsampling factor, and that should provide a good compromise between computational load and accuracy. In our case, the experiments, testing many different step sizes, proved that translation steps of 6 pixels are appropriate for images subsampled by a factor of 16 and that have a resolution of 2.72 microns per pixel. Therefore, this value was fixed and it allowed establishing a proportional relationship between the image resolution (including here the subsampling factor) and the translation step size. For more subsampled and/or lower resolution images this step size must be decreased in order to avoid missing relevant image information, and it can be consequently increased for higher resolution levels. Once the translation steps for the first level are established in this way, the steps of the next levels are calculated by dividing the previous steps by two. This rule was restricted to avoid translation steps smaller than 1 or larger than $1/20^{th}$ of the corresponding image height or width.

Two or three levels were enough to achieve an accurate rigid registration of the cases presented in this chapter. In the first pyramid level, rotation steps of $10°$, with limits of $-170°$ and $180°$ were used. As mentioned before, the translations steps were established empirically, with limits guaranteeing 50% of images overlap as we explained in Section 2.2.2. In the second level, the rotation limits were reduced to the best angle in the first level $\pm 10°$, with steps of $2°$. Finally, in the third level, the rotation limits were reduced to the best angle in the second level $\pm 2°$, with steps of $1°$. The translations steps of each level were calculated as half the step of the previous level. For instance, in the case shown in Figure 2.6, where the images had 2.72 microns per pixel resolution, the translation steps for the rigid registration of the first two sections were as follows: in the first level (with subsampling factor 16), steps of 6 pixels in x- and y-; in the second level (with subsampling factor 8), steps of 3 pixels; and in the third and last level (with subsampling factor 4), steps of 1 pixel. Accordingly, the theoretical maximum error in the third level corresponds to $1°$ of rotation and 4 pixels of translation in every direction, which involves perfect alignment in almost all the synthetic cases.

After proving experimentally the correct operation of both algorithms,

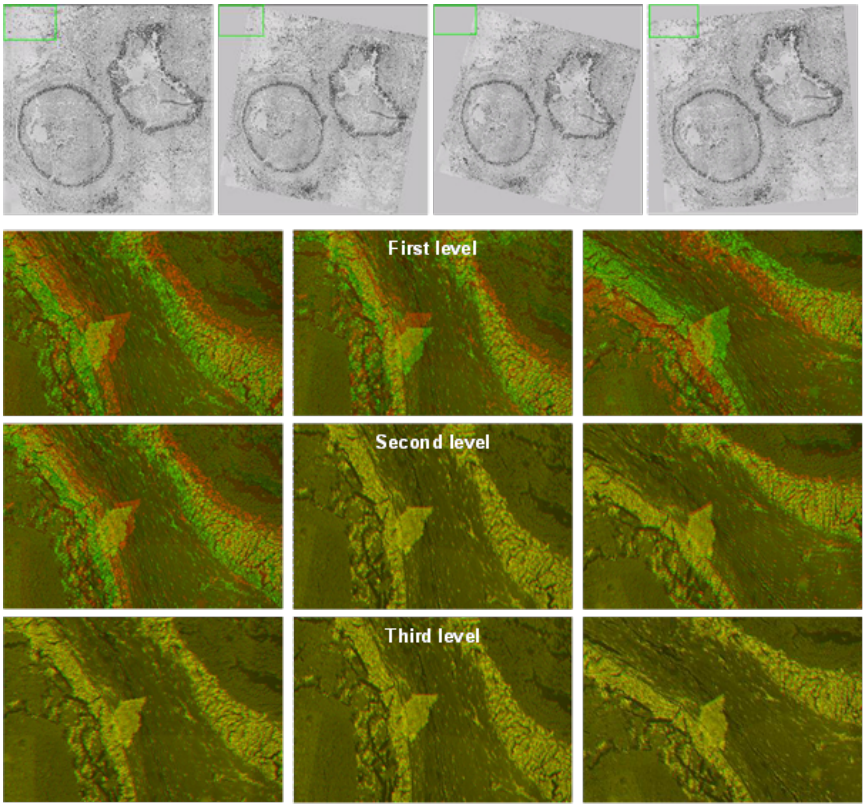

Figure 2.6: Rigid registration results with small rotations. The top row shows the first four sections of the synthetic case created in order to test the algorithms' accuracy. Small angles of rotation and different x- and y-translations were applied to the same image in order to generate the case. Next rows show the zoom over the result color image for each level in the standard rigid registration method and for each pair of sections (from left to right we have the result images from the registration between sections 1-2, 2-3 and 3-4). This image combines the target image in red and the transformed source image in green. Yellow color involves perfect matching, what is practically achieved after 3 levels.

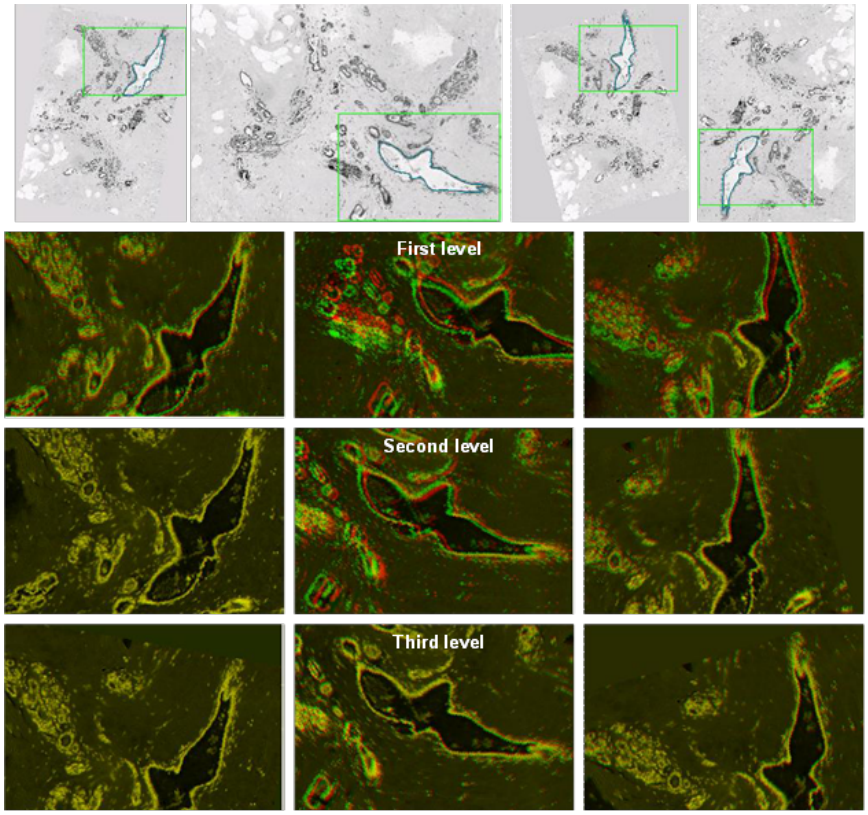

Figure 2.7: Shape rigid registration results with large rotations. The top row shows the first four sections of another synthetic case. Now, larger angles of rotation were applied to the image in order to test the algorithm in extreme conditions. As in Figure 2.6, next rows show the level results of applying the rigid-body alignment for each pair of sections, in this case by the shape registration method. This method makes uses only of the segmentation result, represented in the section images (top row) by blue contours.

they were applied to real mammary gland cases. Contrary to the synthetic cases, the real cases could present substantial differences between sections, therefore the limits in the translations for level 2 and 3 where lightly increased in order to avoid the effect of these differences. Figure 2.8 shows an example of the shape rigid registration of two mammary gland sections and its error evolution.

Both algorithms were written in Java, and run on a PC Pentium IV (2.66GHz, 1GByte of RAM memory) under Linux. The standard rigid registration algorithm takes around 6 minutes to register two typical sections (around 35MB each) with 3 resolution levels, whereas the shape rigid registration uses less than 1 minute to register the same pair of sections also in 3 levels. For most of the cases tested in this work, two algorithm levels provided a rigid-body transformation that matched or was very close to the reachable maximum. For more complex images or synthetic sections, three pyramid levels are recommended.

As a way to quantitatively evaluate the algorithm performance and its error reduction we used a normalized matching value. Let $m(\alpha, t_x, t_y)$ be the final matching value obtained in the corresponding pyramid level, where α corresponds to the final angle of rotation, t_x to the final value for the translation in the x- axis and t_y to the final value for the translation in the y- axis. And let w_c be the number of white —foreground— pixels in the binary contour image obtained from the original target image. Then, the normalized matching value between the target and source images is defined by

$$\overline{m(\alpha, t_x, t_y)} = \frac{m(\alpha, t_x, t_y)}{w_c \cdot 255} \tag{2.3}$$

This value will be always between 0 and 1, and is a pseudo-percentage of the alignment between the images, which allows us quantifying the algorithms accuracy of the registration and also provides a way to compare both algorithms. The normalized matching value will be 0 when none of the contour pixels overlaps any non 0 value in the distance image, and it will be 1 when a perfect matching between contours occurs. Last situation is very unlikely in non-synthetic cases because the contours in consecutive sections normally change.

Table 2.1 shows the evolution of the normalized matching value for both standard and shape rigid registration algorithms when applied to the case whose first four sections are shown in Figure 2.7. The values correspond to the average of the matching values of the entire case. We can observe that the standard method provide lightly less accurate results than the shape

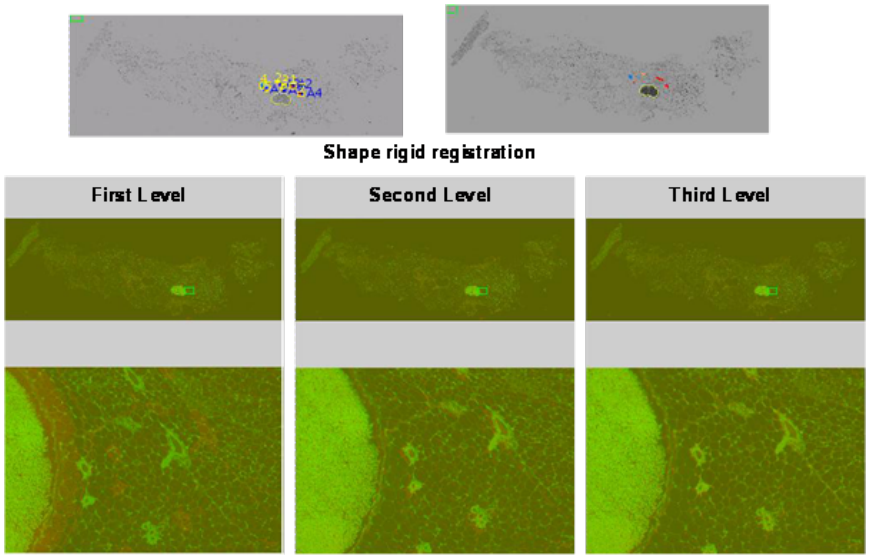

Figure 2.8: Shape rigid registration results on a real case. The top raw shows the two mouse mammary gland sections being registered, where the left image shows the target section and the right image the source one. In this example, the shape rigid registration method was used. The color markings in the gray scale images represent the segmented contours that were used in the registration. The colored squares and letters that appear in the target image are additional information to the sections, which was not used during the registration process. The bottom row shows from left to right the evolution of the error in the three algorithm levels that were used to accomplish the rigid registration. The differences between the results in the second and third level are usually not very significant; they represent scarcely a small refinement to the previous result.

Rigid Registration Method	Level 1	Level 2	Level 3
Standard	0.965780520	0.982260468	0.993172073
Shape	0.986874474	0.994532693	0.996894195

Table 2.1: Comparison between standard and shape rigid registration by the normalized matching value (Case Figure 2.7)

method, as we expected taking into account the elimination of the noise in the shape registration method. We observe also that the differences between the result in the second and the third level are quite small, as we visually noticed first in the color images in Figure 2.8.

2.3.2 Local registration validation

The local registration algorithm was also tested first using artificial cases. In this method, the only way of evaluating the correct operation was either representing the correction vectors over the result color image obtained in the rigid registration, or rendering the sections in three dimensions in order to visualize the improvement in the volume generation. Figure 2.9 show the results obtained applying the local registration method to one of our synthetic cases.

Finally, both versions of the local registration algorithm (registration by gray scale images or by binary contours) were applied to actual cases of mammary gland sections. Different sizes of sub-images and correlation areas were tested. In our cases, given the origin of the images and the distance between their structures, sub-images of 64×64 or 128×128 pixels, and correlation areas of 128×128 or 256×256 pixels provided the most satisfactory results. These sizes must be decided depending on the size of the features of the corresponding images and also on some previous tests. The correlation area should be large enough to cover the maximum error committed during the rigid registration process. However, too large correlation areas would cause the loss of the locality this algorithm was inspired in. Figure 2.10 shows an example of a local registration result and Figure 2.11 shows an example of the improvement in the mesh generation.

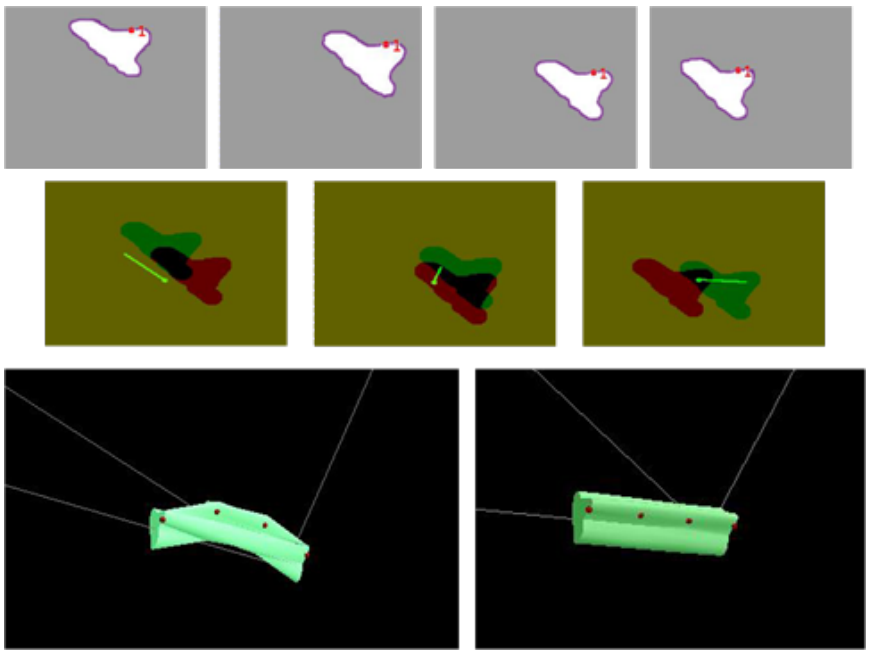

Figure 2.9: Validation of local registration.The top row shows the first four sections of an artificially generated case, which consists of a 256×256 pixel gray scale images with the same white structure linearly shifted to different positions. The segmented contours appear in purple and there is a red point in every contour that allows us better analyzing the results. In this case, only one correlation area was used, whose dimensions correspond to the images dimensions. Thus we can evaluate the goodness of the correction vectors by just comparing them to the original shift vectors that can be calculated subtracting the red points. The second row shows the result color images. As before, the reference image is presented in the red channel, the transformed target image in the green channel, and finally, the correction is painted in light green. The left picture in the bottom row shows the 3D reconstruction of the contours before the local correction. The right picture shows the same volume after applying the correction vector, where an almost perfect alignment is achieved. Notice also the alignment of the four red points, represented in the space by four red spheres.

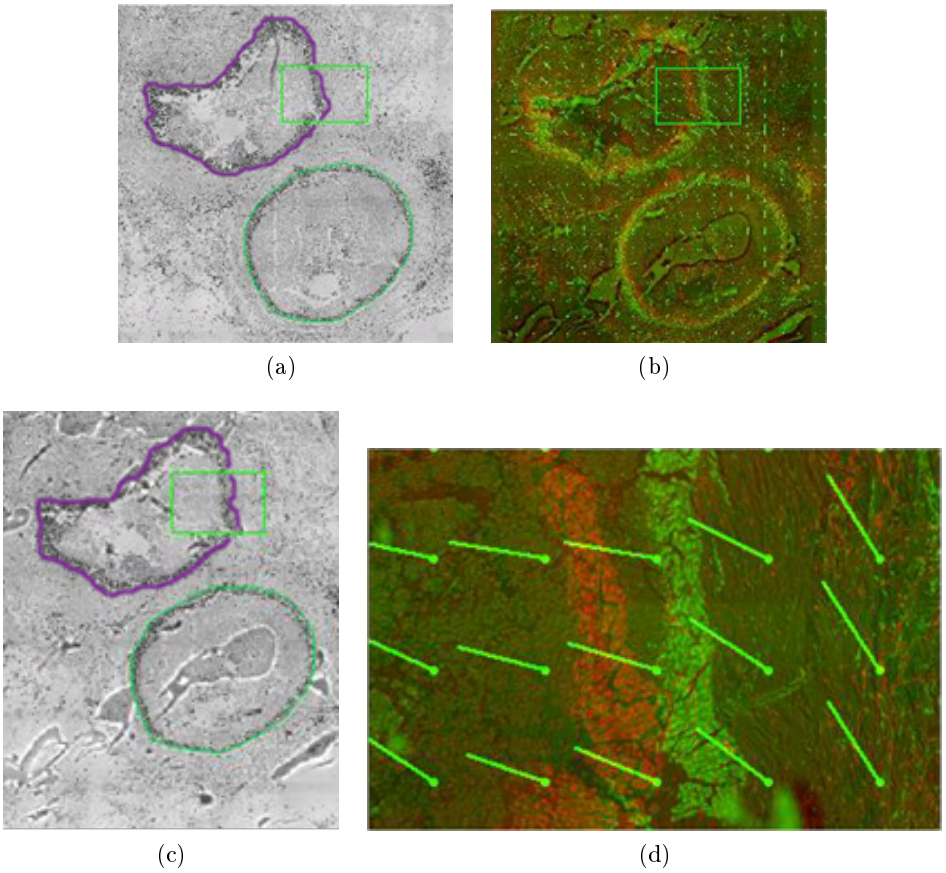

(a) (b)

(c) (d)

Figure 2.10: Local registration results. Pictures 2.10a and 2.10c show respectively the reference and target sections. The segmented contours are represented on purple and green. Pictures 2.10b and 2.10d show the result color image with the correction vectors in light green. For this example, local shape registration was used since this method is very effective in order to remove the effect of strange bodies in the images, as it happened with image 2.10c.

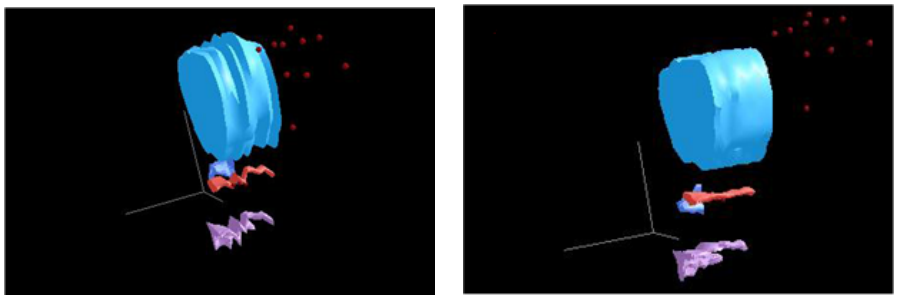

(a) (b)

Figure 2.11: Volumes aligned by local registration. Example of improvement in the three-dimensional reconstruction of the mammary gland morphology. Image 2.11a shows the volume generated from the contours after applying only a rigid-body registration of the sections. A certain zigzag effect in the volumes appears due to the non-linear differences between sections. In image 2.11b, the local registration algorithm has been run over the case and the mentioned effect has disappeared, providing smoother and more realistic 3D representations.

2.4 Discussion

The rigid registration methods presented here perform a global search of the optimum matching value between images. This search is based on a pseudo brute-force strategy, in which a large number of transformations are tested to avoid getting trapped in local matching maxima. Therefore this systematic search could be improved by applying optimization methods that explore the space of search in a faster and more efficiently way. However, the strength of our methods lies precisely in the fact that a global maximum is guaranteed, which does not happen in the original methods (Borgefors, 1988; Hult, 1995) and most of the optimization algorithms presented in the literature.

The large size of our images requires relatively simple and time-saving non-rigid algorithms to correct for local, non-linear registration errors. Volume smoothing algorithms like Laplacian smoothing, improved Laplacian smoothing (Vollmer et al., 1999) or mesh median filtering (Yagou et al., 2002) allow removing the distorting effect in the volumes (see Figure 2.11) with a low computational load, but they do not take into account the global structure of the volumes. However, they can be used at the end of the local refinement process in order to improve the visualization. The two local registration methods presented in this chapter provide very satisfactory results,

but they tend to produce straight and parallel volumes, losing their natural orientation. Therefore, a global inter-section study of the volume through the case is required in order to preserve the original morphology, distinguishing between the natural shifts of the structures in the images and the shifts that are produced due to the misalignment of the sections.

Our local registration methods can be improved if the sub-images used to calculate the local correlation fit the bounding boxes of the contours annotated in the segmentation process. Such improvement is described in Chapter 5, Section 5.2.5.

2.5 Conclusions

We described a complete and automatic algorithm for the registration of microscope images of serial tissue sections. The algorithm is divided in two phases, a first rigid-body registration and a subsequent local refinement. The global maximum of the rigid transformation is guaranteed. Both registration methods present two variants, the first one is based on the gray scale information of the images, and the second one is based on a previous segmentation of the relevant contours in the images. The algorithms presented in this chapter were applied to mammary gland tissue sections but can also be used on other types of tissues and imaging modalities.

Acknowledgments

The work presented in this chapter was supported by the US Department of Defense and California Breast Cancer Research Programs under grants DAMD17-00-1-306 and 8WB-0150 (respectively), by the LBNL Laboratory Directed Research and Development Program, under contract CSLD12 and by the National Institute of Health under grant 1R01HL67465-01.

This research would not have been possible without the help, patience, support, enthusiasm and experience of the whole Ortiz-de-Solorzano's Lab: Fernandez-Gonzalez R., Idica A., Laribi O., Khan S., Hartland A., Ortiz-de-Solorzano C. We would like to express our gratitude to *ImageJ* open source project for provided code (Rasband (1997-2009)) and give special thanks to Yalda Afshar and Cèline Ferré for their patience and English review.

3

Consistent and Elastic Pairwise Registration of Histological Sections Using Vector-Spline Regularization

"Not everything that can be counted counts, and not everything that counts can be counted."

Albert Einstein

Abstract

In this chapter we present a new image registration algorithm for the alignment of histological sections that combines the ideas of B-spline based elastic registration and consistent image registration, to allow simultaneous registration of images in two directions (direct and inverse). In principle, deformations based on B-splines are not invertible. The consistency term overcomes this limitation and allows registration of two images in a completely symmetric way. This extension of the elastic registration method simplifies the search for the optimum deformation and allows in many cases registering with no information about landmarks or deformation regularization. This approach could be used as the first step to solve the problem of group-wise registration.

3.1 Introduction

Studying the three-dimensional organization of complex histological structures requires imaging, analyzing and registering large sets of images taken

from serially sectioned tissue blocks. As explained in Chapter 2, we have developed an integrated microscopy system that automates or greatly reduces the amount of interaction required for these tasks (Fernandez-Gonzalez et al., 2002, 2004) and provides volumetric renderings of the structures in the tissue (see Chapter 5).

Proper section alignment is the first step towards an accurate 3D tissue reconstruction, as it is in other imaging modalities. Image registration methods have been intensively studied in the field of medical imaging, and we refer interested readers to the articles by Maintz and Viergever (1998), Glasbey and Mardia (1998), Lester and Arridge (1999) and Hajnal et al. (2001) for excellent reviews. In our case, we first perform a coarse alignment of the sections using an automatic rigid-body registration method (see Chapter 2, Section 2.2.2 or Arganda-Carreras et al. (1-5 Sept. 2004)). This method can not correct some non-linear distorting effects (e.g. tissue folding, stretching, tearing, etc.) caused by the manual sectioning process. Moreover, the distance between sections causes significant differences between the same structures of interest in consecutive sections, which could be misinterpreted by a complete linear registration process. Therefore, a local (Chapter 2, Section 2.2.3) or non-linear method is strongly needed in order to refine the first registration step. In this chapter we present a new method for elastic and consistent registration of histological sections. All the examples described in the chapter used mammary gland tissue samples; however, the same algorithm could be equally applied to other tissue sources and image modalities, as it is shown in Appendix A.

3.2 Methodology

A key element in any registration algorithm is the method chosen to model the deformation functions. We decided to use splines. Thin-plate splines (TPS) by Bookstein (1989) have been widely used in medical image registration (Rohr et al., 1996; Johnson and Christensen, 2002; Auer et al., 2005; Eriksson and Astrom, 2006). However, TPS have a global support, which is not appropriate to model local image deformations, which are better modeled by using B-splines (Xiao et al., 2002; Xie and Farin, 2004; Loeckx et al., 2004; Sorzano et al., 2005; Zheng et al., 2006). Therefore, we chose to use B-splines for both interpolating the images and modeling the deformation functions. B-splines are computationally light, are differentiable, have good approximation properties and can be used to represent both linear and non-linear transformations, providing close control of the level of detail of the

transformation. Indeed, the properties of B-splines have been largely proved to be very useful when modeling deformations in many biomedical imaging problems; such as tracking the movement of the left ventricle from MRI images (Radeva et al., 1997), reconstructing the 3-D motion of the cardiac cycle (Huang et al., 1999) or modeling the motion of the breast by dynamic MR imaging (Rueckert et al., 1999). Moreover, we use a multiresolution (iterative coarse-to-fine) implementation, which improves the convergence speed and robustness of the algorithm (Unser, 1999).

The registration of a source image with a target image can be defined as the problem of finding a deformation field that transforms coordinates of the target image into coordinates of the source image. The main problem of using B-spline deformation fields is that the estimated field might not be invertible (which is not a problem since depending on the specific case, the true deformation field may not be invertible neither). However, in case it were invertible, the inverse deformation field can be computationally expensive. Either it is invertible or not, it is convenient to have also a way of transforming coordinates in the source image into coordinates of the target. This would define a second deformation field that is close to the inverse of the original field and it has proven to be useful as a way of regularizing the registration problem (Christensen and He, 2001; Avants et al., 2006). This two-way registration is known as **consistent registration**. Avants et al. (2006) achieve the consistency by forcing the deformation field to be a diffeomorphism (continuous, differentiable, and invertible, its inverse must also be continuous and differentiable). This is a too strong constraint for our images, although it has the advantage of not having to compute two separate fields since the diffeomorphism condition automatically guarantees the existence of the deformation inverse. Christensen and He (2001) compute two independent deformations whose composition should be as close as possible to the identity transformation. Thus, one is not the inverse of the other. This closeness to identity is explicitly introduced into the objective function.

In this work we combine the idea of elastic registration using vector-spline regularization (Sorzano et al., 2005) with that of a consistent registration (Christensen and He, 2001). We combine both ideas and extend them in order to overcome their limitations. The standard registration method presented by Sorzano et al. (2005) proposes the calculation of the elastic deformation field trough the minimization of an energy functional composed by three terms: the energy of the similarity error between both images (represented by the pixelwise mean-square distance), the error of the mapping of soft landmarks, and a regularization term based on the divergence and the curl of the deformation to ensure its smoothness. This minimization is opti-

mized by a variant of the robust Levenberg-Marquardt method (Marquardt, 1963).

We transform the energy functional presented by Sorzano et al. (2005) into a new functional that incorporates a factor of the deformation field consistency. Unlike Sorzano et al. (2005), we are now looking for two transformations at the same time (direct and inverse). Therefore, the vectors passed to the Levenberg-Marquardt optimizer are now twice as long. Besides the measurement of dissimilarity between the source and target images (now in both directions) E_{img}, the optional landmark constraint E_{μ} and the regularization term $(E_{div} + E_{rot})$, we add a new energy term E_{cons} that expresses the geometrical consistency between the elastic deformation in one direction (from source to target) and the other direction (from target to source). Therefore, the energy function is now given by

$$E = w_i E_{img} + w_{\mu} E_{\mu} + (w_d E_{div} + w_r E_{rot}) + w_c E_{cons} \tag{3.1}$$

Where w_x are the specific weights given to the different energy terms.

3.3 Consistency Term

The consistency energy represents the geometrical distances between the pixel coordinates after applying both transformations (direct-inverse or inverse-direct), i.e. the amount by which the composed transformation differs from identity. The standard approach by Sorzano et al. (2005) for this type of registration is to find a deformation function

$$g^{+}(x) : \mathbb{R}^2 \rightarrow \mathbb{R}^2. \tag{3.2}$$

This function transforms the source image I_s into an image as similar as possible to the target image I_t. This transformation g^{+} maps coordinates in I_s into coordinates in I_t. Here, following the idea of Christensen and He (2001), we will also simultaneously look for its corresponding inverse function

$$g^{-}(x) : \mathbb{R}^2 \rightarrow \mathbb{R}^2. \tag{3.3}$$

This function maps the coordinates in I_t into coordinates in I_s. Following this notation, our consistency energy term is given by

$$\begin{aligned} E_{\text{cons}} = E^{+}_{cons} &+ E^{-}_{cons} \\ &= \int_{\mathbf{x}\in\mathbb{R}^2} \|\mathbf{x} - g^{-}(g^{+}(\mathbf{x}))\|^2 d\mathbf{x} \\ &\quad + \int_{\mathbf{x}\in\mathbb{R}^2} \|\mathbf{x} - g^{+}(g^{-}(\mathbf{x}))\|^2 d\mathbf{x}. \end{aligned} \tag{3.4}$$

If we approximate the integrals by discrete sums and restrict the integration domain, we obtain

$$E^{+}_{cons} = \frac{1}{\#\Omega^{+}} \sum_{\mathbf{x}\in\Omega^{+}} \|\mathbf{x} - g^{-}(g^{+}(\mathbf{x}))\|^2. \tag{3.5}$$

$$E^{-}_{cons} = \frac{1}{\#\Omega^{-}} \sum_{\mathbf{x}\in\Omega^{-}} \|\mathbf{x} - g^{+}(g^{-}(\mathbf{x}))\|^2. \tag{3.6}$$

Where , Ω^{+}, Ω^{-} define sets of relevant pixels common to the target and source images:

$$\Omega^{+} = \{\mathbf{x} \in \Omega_s \cap \mathbb{Z}^2 : g^{+}(x) \in \Omega_t \cap \mathbb{Z}^2\}. \tag{3.7}$$

$$\Omega^{-} = \{\mathbf{x} \in \Omega_t \cap \mathbb{Z}^2 : g^{-}(x) \in \Omega_s \cap \mathbb{Z}^2\}. \tag{3.8}$$

And where $\#\Omega^{+}$ and $\#\Omega^{-}$ are the number of pixels in the masks.

3.4 Deformation Representation

Following the same idea as Sorzano et al. (2005) we represent the deformation fields as a linear combination of B-splines. For instance, g^{+}:

$$\begin{aligned} g^{+}(\mathbf{x}) &= g^{+}(x,y) \\ &= \left(g^{+}_1(x,y), g^{+}_2(x,y)\right) \\ &= \sum_{k.l\in\mathbb{Z}^2} \begin{pmatrix} c^{+}_{1,k,l} \\ c^{+}_{2,k,l} \end{pmatrix} \beta^3\left(\frac{x}{s_x} - k\right) \beta^3\left(\frac{y}{s_y} - l\right) . \end{aligned} \tag{3.9}$$

Where s_x and s_y are scalars (sampling steps) controlling the degree of detail of the representation of the deformation field.

3.5 Explicit Derivatives

The chosen optimizer uses gradient information. We will now calculate the derivatives of the energy function with respect to all the parameters, starting with E_{cons}. It can be easily shown that the derivative of E^{+}_{cons} with respect to any of the deformation coefficients defining the first component (x in our case) of the direct deformation field g^{+}, is given by

$$\frac{\partial E^{+}_{\text{cons}}}{\partial c^{+}_{1,k,l}} = -2 \sum_{\mathbf{x}\in\Omega^{+}} \left(\mathbf{x} - g^{-}\left(g^{+}(\mathbf{x})\right)\right) \cdot \left(\frac{\partial}{\partial c^{+}_{1,k,l}} \left(g^{-}\left(g^{+}(\mathbf{x})\right)\right)\right) \ . \tag{3.10}$$

Where

$$\frac{\partial}{\partial c^{+}_{1,k,l}} \left(g^{-}\left(g^{+}(\mathbf{x})\right)\right) = \left(\left.\frac{\partial g^{-}_{1}}{\partial x}\right|_{x',y'}, \left.\frac{\partial g^{-}_{2}}{\partial y}\right|_{x',y'} \right) \left.\frac{\partial g^{+}_{1}}{\partial c^{+}_{1,k,l}}\right|_{x,y} \ . \tag{3.11}$$

And where

$$\mathbf{x} = (x, y) \ . \tag{3.12}$$

And

$$(x, y) = g^{+}(x, y) \ . \tag{3.13}$$

Again, following the definition of the transformation function we express its derivative with respect to the coefficients of the first component as

$$\frac{\partial g^{+}_{1}(x,y)}{\partial c^{+}_{1,k,l}} = \beta^{3}\left(\frac{x}{s_x} - k\right) \beta^{3}\left(\frac{y}{s_y} - l\right) \ . \tag{3.14}$$

This derivative is the same in the case of the second component.

The derivative of E^{+}_{cons} with respect to any of the deformation coefficients of the second component of the direct deformation field is calculated in an analogous way.

Let us see now the derivative of E^{+}_{cons} with respect to the coefficients of the first component of the inverse transformation:

$$\frac{\partial E^{+}_{\text{cons}}}{\partial c^{-}_{1,k,l}} = -2 \sum_{\mathbf{x}\in\Omega^{+}} \left(\mathbf{x} - g^{-}\left(g^{+}(\mathbf{x})\right)\right) \cdot \left(\frac{\partial}{\partial c^{-}_{1,k,l}} \left(g^{-}\left(g^{+}(\mathbf{x})\right)\right)\right) \ . \tag{3.15}$$

Where

$$\frac{\partial}{\partial c^{+}_{1,k,l}} \left(g^{-}\left(g^{+}(\mathbf{x})\right)\right) = \frac{\partial}{\partial c^{+}_{1,k,l}} \left(g^{-}(x', y')\right) = \beta^{3}\left(\frac{x'}{s_x} - k\right) \beta^{3}\left(\frac{y'}{s_y} - l\right) \ . \tag{3.16}$$

The derivative of E^{+}_{cons} with respect to any of the deformation coefficients of the second component of the inverse deformation field can be calculated in an analogous way. The derivatives of E^{-}_{cons} are easily inferred in a similar way. We refer to the original article from Sorzano et al. (2005) for the derivatives of E_{img}, E_{μ} and $(E_{\text{div}} + E_{\text{rot}})$.

3.6 Choice of consistency weight w_{c}

Every energy term composing the functional represents a different measure over the images or the deformations and presents different units. Therefore, the terms are not comparable and a weight term is needed. We determined the optimum value experimentally. While value of zero is useful to compare results with the previous algorithm, weight values around 10.0-30.0 often showed the best compromise between the final similarity and the deformations consistency for our images. Higher values make the consistency constraint too rigid and consequently decrease the images similarity. Lower values cause the lack of relevance between g^{+} and g^{-} in the optimization process and thus do not achieve symmetric transformations. Figure 3.1 shows the evolution of the similarity error with respect to w_{c}. The consistency error decreases with the weight but causes a significant increase in the similarity error when approaching to values close to 100.

For the rest of weight terms we refer to Sorzano et al. (2005). From our own experience we recommend to set w_{i} to 1.0 and if necessary, w_{μ} to 1.0 and w_{d} and w_{r} to 0.1.

3.7 Results

3.7.1 Visual evaluation

To evaluate our algorithm we first tested its performance using synthetic images. We applied some known deformations to the images and then checked whether our method could correct the deformation. That also allowed us to compare our algorithm with the standard one from Sorzano et al. (2005). For instance, in Figure 3.2 we have registered a Lena picture with a deformed version of the same image. In this case, the standard method properly registers the deformed image with the original one, but is unable to find the inverse deformation field without using soft landmarks, regularization values and a specific image mask. In the same example, our algorithm finds simultaneously both deformation fields (direct and inverse) using only the

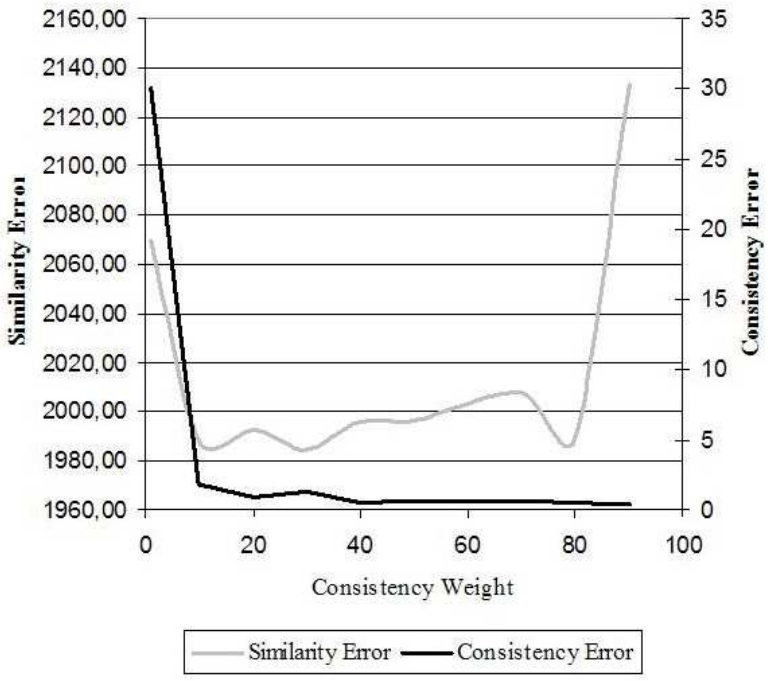

Figure 3.1: Evolution of the similarity and consistency error with increasing values of the consistency weight.

Figure 3.2: From top to down, left to right: source image, target image, registered source image (by the standard method), registered source image (by our new method), registered target image (by our new method)

similarity term and the consistency term of the energy function.

Figures 3.3, 3.4, and 3.5 contain a relevant example of the results obtained applying our algorithm compared to the results obtained with the original method (lacking the consistency term) using two consecutive histological sections from breast cancer tissue.

Figure 3.4 shows the deformation fields calculated with both methods. It is easy to see how our method guarantees the consistency between the direct and the inverse transformation while the traditional method does not.

In Figure 3.5 we show the result of subtracting the deformed source and target images. We can appreciate how for the inverse transformation our method achieves a much better result than the standard method, as we expected by observing the deformation fields on Figure 3.4 These results were also evaluated numerically obtaining an average of similarity error of 31.63 and 32.68 for the deformations calculated with the original method (direct-inverse and inverse-direct) and an average of 31.48 and 31.66 for the deformations of our new method. The differences between the inverse-direct averages provoke visible changes on the registration as shown in the

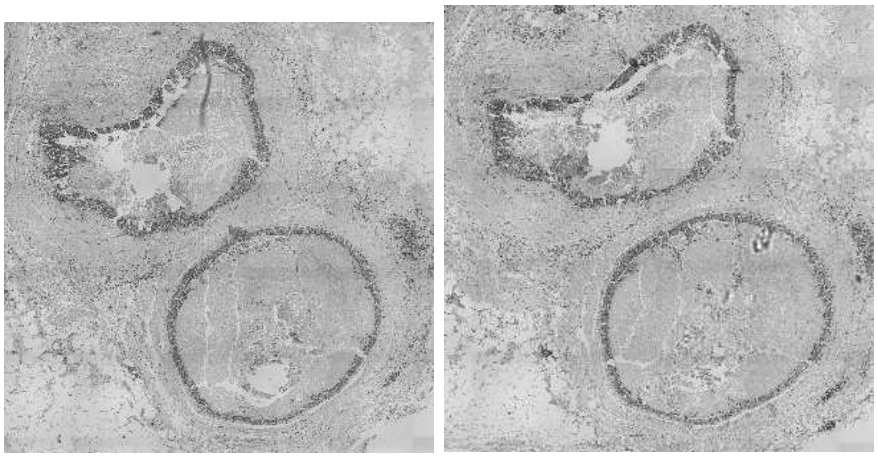

Figure 3.3: Two consecutive histological sections from a human biopsy presenting two big tumors.

deformation fields representations on Figure 3.4.

The gray-scale sample images in Figure 3.3 have respectively 325×325 pixels and 300×312 pixels and it took 18 seconds to properly register them in an Intel Pentium M, 1.60 GHz, 589 MHz, 512MB of RAM memory, under a SuSE Linux system.

Figure 3.6 is another example with breast tissue sample where the standard method is unable to approach any proper deformation between the source and target images based in the images similarity but where our new method achieves easily the right deformation thanks to the consistency term.

As inferred from the experimental results using our bidirectional method, in most cases only the similarity and the consistency term are needed to achieve a proper registration. This involves a simplification of the energy functional to be minimized and therefore, a reduction in the computational time and complexity. At the same time, forgetting about placing soft landmarks in the images allows us reducing the human interaction in the registration process, which is another advantage of our algorithm over the previous method.

3.7.2 Numerical evaluation

We developed a software to help to numerically test the performance of the method. This program can apply five different deformations on an image: elastic, fisheye, perspective, barrel/pincushion and "simile" deformations (see

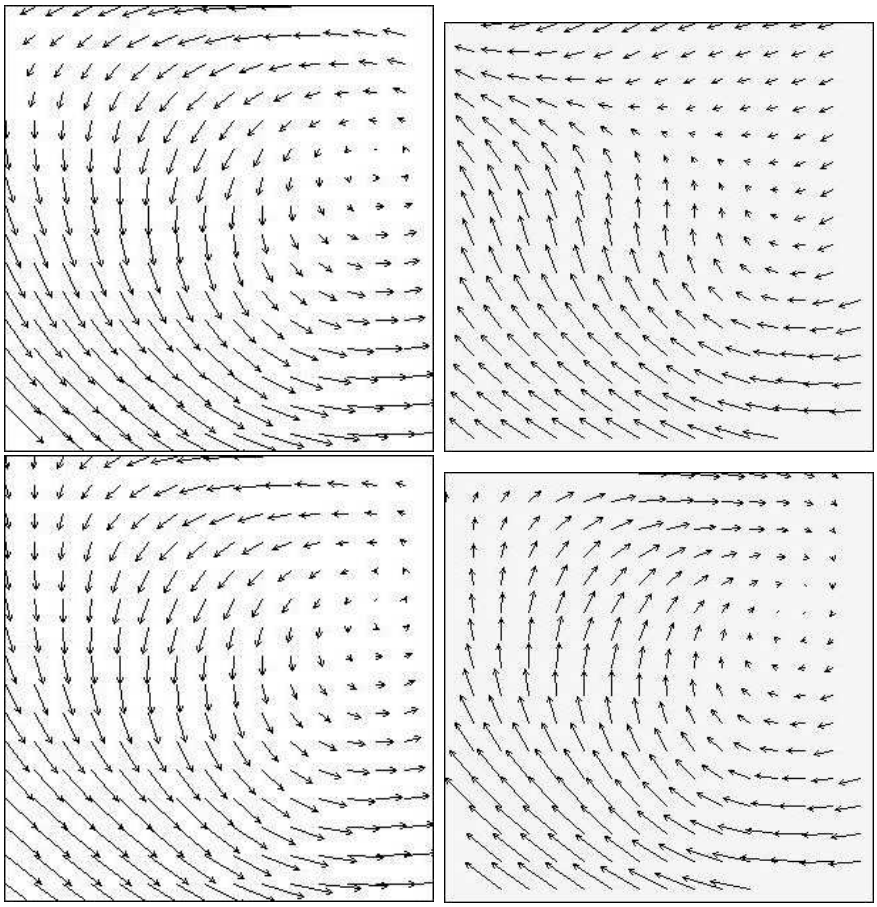

Figure 3.4: Comparison of the deformation fields obtained with the original method described in Sorzano et al. (2005) and our new algorithm over the images in Figure 3.3. The first row shows the deformation when registering image 1 to 2 (left) and image 2 to 1 (right), applying the traditional energy functional. The second row shows the same deformations when using the proposed improvement.

Figure 3.7). This way, we can produce synthetic data sets with known deformations and then apply our registration method to correct them. We measured the accuracy of the registrations using a mean squared distance version of the standard *warping index* (Thévenaz et al., 1998) defined as

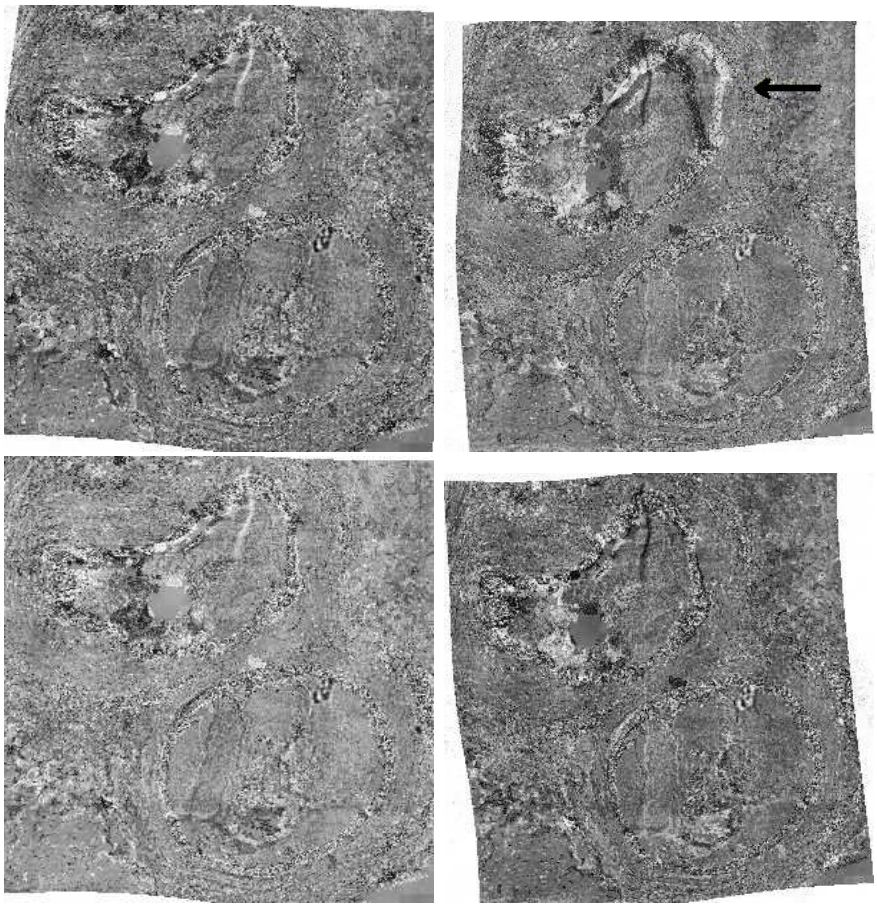

Figure 3.5: The top row shows the subtractions of the deformed images and the target ones in both senses, using the traditional method. The bottom row shows the result when applying our method. The black arrow points the most relevant error committed by the standard method.

$$\varpi = \sqrt{\frac{1}{\| R \|} \sum_{\mathbf{x} \in R} \| \mathbf{x} - g(g^*(\mathbf{x})) \|^2}. \tag{3.17}$$

Where g^* is the synthetic known deformation, g is the deformation in the opposite direction and R is the set of pixels common to both images. The warping index measures the average geometric error —in pixels— between the original transformation and the deformation calculated by our algorithm.

In most cases and for all types of deformations, setting the right parame-

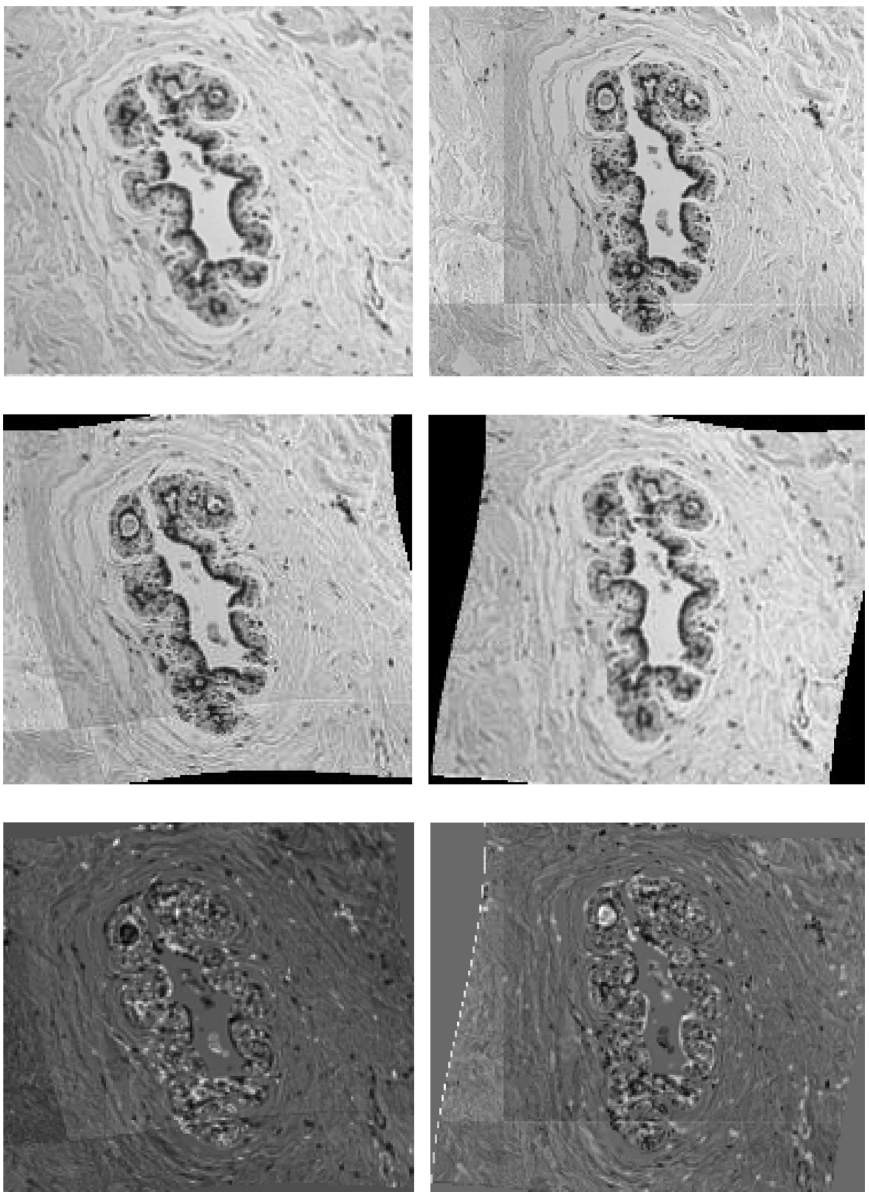

Figure 3.6: Example with two transversal cuts of a mammary duct. From top to down, left to right: source image, target image, registered target image, registered source image, difference source image, difference target image.

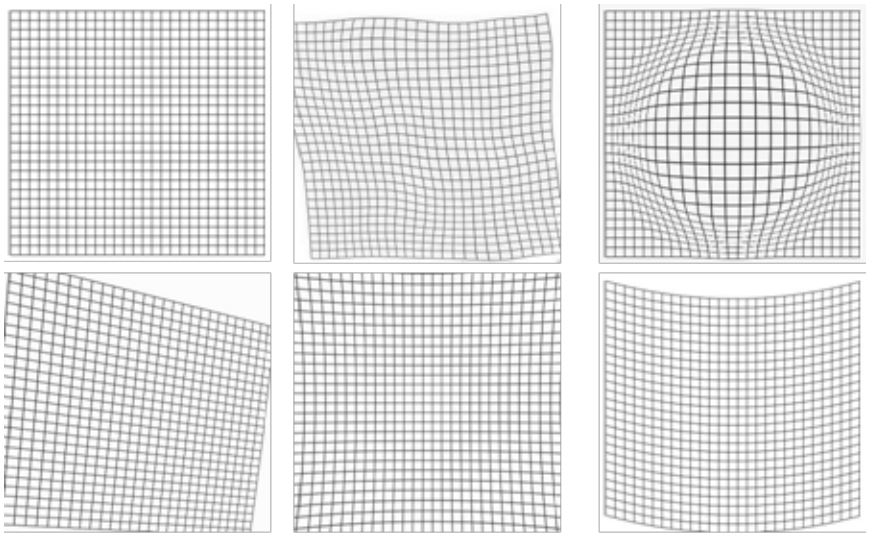

Figure 3.7: Types of artificial deformations to test the registration. From left to right and from top to down: the original grid image and its corresponding elastic, fisheye, perspective, barrel and smile effect examples of deformations.

ters (weights) our method achieves a warping index below 1.0 —i.e. sub-pixel accuracy— without the use of landmarks or regularization.

3.8 Conclusions

A new algorithm for consistent elastic registration has been presented. It combines the ideas of elastic image registration based on B-splines models and consistent image registration. The method improves the results obtained without the consistency factor in the energy function, as it has been qualitative and numerically shown in the results section, and accelerates the search for the optimum.

This consistent and elastic registration method was implemented as an *ImageJ* plugin (Rasband, 1997-2009) called *bUnwarpJ* (from **b**idirectional **unwarp**ing in **J**ava, Arganda-Carreras et al. (2008)). The most up-to-date release of this *ImageJ* plugin and its source code can be freely downloaded from `http://biocomp.cnb.csic.es/~iarganda/bUnwarpJ/`. The software to produce the random image deformations was as well implemented as an *ImageJ* plugin. It is called *SplineDeformationGenerator* and can be found at `http://biocomp.cnb.csic.es/~iarganda/SplineDeformationGenerator/`.

The registration method described in this chapter could be extended, for instance, increasing the number of images involved in the registration to do group-wise registration. For this case, the explicit derivatives must be recalculated and a method for composing the deformation fields needs to be proposed.

4

Non-rigid Consistent Registration of 2D Image Sequences

"Problems worthy of attack prove their worth by fighting back."

Paul Erdos

Abstract

In this chapter we present a novel algorithm for the registration of 2D image sequences that combines the principles of multiresolution B-spline based elastic registration and those of bidirectional consistent registration. In our method, consecutive triples of images are iteratively registered to gradually extend the information through the set of images of the whole sequence. The intermediate results are reused for the registration of the following triple. We choose to interpolate the images and model the deformation fields using B-spline multiresolution pyramids. Novel boundary conditions are introduced to better characterize the deformations at the boundaries. In the experimental section, we quantitatively show that our method is able to recover from barrel/pincushion deformations with subpixel error. Moreover, it is more robust against outliers —occasional random strong noise and large rotations— than the state-of-the-art methods. Finally, we show that our method can be used to realign series of histological serial sections, which are often heavily distorted due to folding and tearing of the tissues.

4.1 Introduction

Registering two images consists in finding a deformation function that maps a given image S onto a target image T. Finding an optimal deformation function requires maximizing a similarity criterion between the intensities of all pixels in both images and/or mapping selected reference —landmark— points. In an ideal situation, the deformation function should be unique and bijective. In other words, it should unequivocally link every pixel in the target image T with a pixel in the source image S. It should also have biological meaning appropriate for the particular image modality and source of misalignment.

The problem of registering pairs of images can be extended to registering sets of spatially, temporally or spectrally related images. The state-of-the-art approaches for this type of registration are: (i) register all images to a reference image or (ii) pairwise register all the images starting from the first image of the sequence. In the first approach all the images in the group are registered to a reference image, which can be a selected image of the group (Marsland et al., 2003; Malandain et al., 2004), an average image (Bhatia et al., 2004) or an iteratively calculated image model (Twining et al., 2005). This is commonly used to locate an image in a normalized reference frame or coordinate system as part of the process of generating anatomical atlases (Bhatia et al., 2004; Twining et al., 2004). In the second approach, the images are registered as a sequence applying pairwise deformation functions. This is more appropriate for sequences of images that change in time, space, wavelength, etc. It has been used, for instance for tracking cardiac motion in MRI images (Radeva et al., 1997; Huang et al., 1999; Rueckert et al., 1999; Ledesma-Carbayo et al., 2005), registering blocks of histological tissue sections (Auer et al., 2005; Wirtz et al., 2005; Arganda-Carreras et al., 2006) or registering multispectral fluorescence microscope images (Matula et al., 2004).

Both approaches bias the registration by assigning special relevance to one of the images in the sequence. An alternative method consist of sequentially registering neighborhoods of images —i.e. subgroups of consecutive images— in order to increase the robustness of the registration and the smoothness of the deformations without assigning an arbitrary normative value to any of the images. For instance, Wirtz et al. (2004) unidirectionally registered neighborhoods of three images. Yushkevich et al. (2006) bidirectionally registered 5-image neighborhoods, after choosing a reference image and removing what they considered bad slices in the sequence. Alternatively, Geng et al. (2005) registered groups of three manifolds , i.e. contours

or surfaces.

The second key element of a registration algorithm is the method used to model the transformation between the source and target images. Some authors proposed using diffeomorphic deformation functions, which are invertible, differentiable and bijective (Avants et al., 2006; Cootes et al., 2004; Rueckert et al., 2006; Grenander and Miller, 1998). This method is fast, efficient and very appropriate when the transformation satisfies the diffeomorphic properties. However, this might not be the case for some large non-linear transformations, such as the ones that can be found in series of manually processed histological sections, which are often heavily folded or torn. An alternative approach (Christensen and Johnson, 2001; Thirion, 1998) consists in jointly estimating the direct (S onto T) and reverse (T onto S) deformations and imposing as a constraint that one be the inverse of the other. This method significantly reduces the registration error and while calculating the direct transformation g^{st} it also provides a deformation g^{ts} that is very similar to the ideal $(g^{st})^{-1}$.

In this work, we build upon and combine the concepts of neighborhood registration (Geng et al., 2005) and consistency (Christensen and Johnson, 2001) in the context of the registration of series of images (Csapo et al., 2007). Namely, we use the general idea of transitivity from computational anatomy suggested by Grenander and Miller (1998), but we do not enforce by definition the invertibility of the anatomical transformations. Instead, we enforce it by approach as proposed by Christensen and Johnson (2001). This way, we can calculate and recover from complex non-invertible distortions, such as those commonly found in histological sections (e.g. tissue folding and tearing). Then, looking for a computationally reasonable compromise solution to the problem of registering image sequences, we use Geng et al. (2005) tri-wise registration concept —originally developed to register triples of contours— apply it to triples of images, and then extend it to register entire image sequences. The propagation of the information through the entire sequence is ensured by the overlap between the image triples and the iterative back-and-forth progression of the algorithm. To register each image triple —which is the building block of the registration of the entire sequence—, we take advantage of the fact, proved by Csapo et al. (2007), that the sequential composition of two transformations is equivalent to the transformation between the first and third member of the triple. This was used by Csapo *et al.* to unidirectionally and non-consistently register sequences of images, and we here extend its use to the bidirectional and consistent registration of triples of images. In summary, we approach the problem of registering series of images by bidirectionally registering consecutive triples of images, to find

a solution that minimizes the overall similarity and consistency errors while keeping acceptable computational speed. The consistency is ensured locally through the registration of groups of three images and globally by spreading the results back and forward in the whole set of images.

In our implementation we estimate the deformation function by minimizing a cost functional made of two terms: a similarity term and a consistency term. We use an efficient Marquardt-Levenberg optimization method (Marquardt, 1963) with Hessian estimation (Press et al., 1992). We use B-splines to interpolate the images and model the deformation functions. B-splines are computationally light, differentiable, have good approximation properties and can be used to represent both linear and non-linear transformations, providing close control of the level of detail of the transformation. Finally, we use a multiresolution (iterative coarse-to-fine) implementation, which improves the convergence speed and robustness of the algorithm (Unser, 1999). Although this method can be applied to many registration problems, we show in particular the benefit obtained by using it to register series of histological sections, which are often affected by dramatic deformations.

The structure of the chapter is as follows. First we describe the previous work in Section 4.2.1, and then we introduce the concept of consistent triwise registration in Section 4.2.2. The two terms of our cost functional are described in Sections 4.2.3 and 4.2.4. The image and deformation representations are presented in Sections 4.2.5 and 4.2.6. Our optimization algorithm is then described in Section 4.2.7 while the multiresolution implementation is presented in Section 4.2.8 and the main outline of our consistent sequential registration method is introduced in Section 4.2.9. Next, we show experimental results, first with synthetic images in Section 4.3.1, and also with real sequences of biological images in Section 5.3.2. We finish with conclusions in Section 5.4.

4.2 Methods

Given three consecutive images of a sequence, our algorithm finds the deformation fields that relate them. This is done by minimizing an energy functional that has two terms: the similarity error $E_{\mathrm{S}}^{T_i}$ between every triple T_i —local group of three consecutive images I_i, I_{i+1}, I_{i+2}— and the consistency error of the corresponding partial deformations $E_{\mathrm{C}}^{T_i}$. The energy functional can be written as

$$E = \sum_{i=1}^{N_S-2} \left(w_{\mathrm{s}} E_{\mathrm{S}}^{T_i} + w_{\mathrm{c}} E_{\mathrm{C}}^{T_i} \right), \tag{4.1}$$

where N_S is the number of images in the sequence and w_s and w_c are the specific weights given to the similarity and consistency energy terms.

4.2.1 Pairwise registration

Our work builds on our previous work (see Chapter 3) and that of others. Namely, we develop on the idea of Unidirectional Pairwise Registration (UPR) (Sorzano et al., 2005; Kybic and Unser, 2003) and of Consistent Pairwise Registration (CPR) (Christensen and Johnson, 2001; Arganda-Carreras et al., 2006).

UPR can be formulated as finding the best deformation function $g(\mathbf{x}) : \mathbb{R}^2 \rightarrow \mathbb{R}^2$ that transforms a source image I_s into a target image I_t. Therefore, the deformed version of the source image, $I_s(g(\mathbf{x}))$, should closely resemble the target image $I_t(\mathbf{x})$.

CPR adds the idea of imposing a consistency constraint by simultaneously calculating the transformations g and h such that g maps I_s to I_t and h maps I_t to I_s subject to the constraint $g \simeq h^{-1}$. The search space is twice as large as in the unidirectional case. However the consistency constraint often allows faster convergence in terms of number of iterations compared to a non-consistent registration, as it will be shown in Section 4.3.1.5.

4.2.2 Consistent Tri-wise Registration

We now extend the previous concepts —UPR and CPR— to the case of simultaneously registering three images. We call it Consistent Tri-wise Registration (CTR). Let I_1, I_2 and I_3 be the images to be registered. We aim at finding the deformation functions

$$g^{ij}(\mathbf{x}) : \mathbb{R}^2 \rightarrow \mathbb{R}^2, \tag{4.2}$$

that map coordinates of I_i into coordinates of I_j. The explicit estimation of g^{13} and g^{31} as described by Geng et al. (2005) improves the consistency of the deformations at expense of increasing the complexity of the optimizer. Instead, looking for a compromise between accuracy and computation time, we decided to use only pairwise transformations (12, 23...) to move through the sequence. This was originally proposed by Csapo et al. (2007), who showed that the composition of the intermediate transformations g^{12} and g^{23}

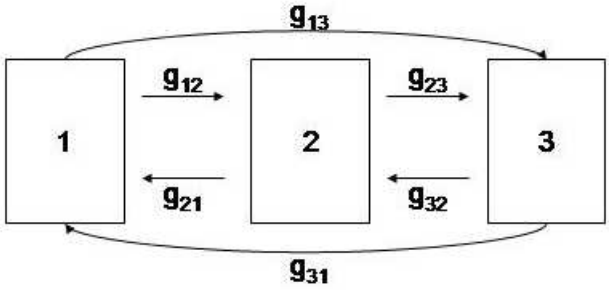

Figure 4.1: CTR scheme. The diagram shows a group of three images and their corresponding transformations. For every pair of images (i and j with $i, j = 1, 2, 3$ and $i \neq j$) there are two functions (g^{ij}, g^{ji}) that map pixel coordinates from image i to image j and vice versa.

makes g^{13} and g^{31} implicitly consistent. Therefore, only g^{12}, g^{21}, g^{23} and g^{32} need to be calculated, as we defined g^{13} and g^{31} by composition, that is $g^{13} = g^{23} \circ g^{12}$ and $g^{31} = g^{21} \circ g^{32}$, i.e. $g^{13}(\mathbf{x}) = g^{23}(g^{12}(\mathbf{x}))$ and $g^{31}(\mathbf{x}) = g^{21}(g^{32}(\mathbf{x}))$. See Figure 4.1 for a graphical description of the transformations involved.

4.2.3 Similarity Error Term

We calculated the similarity between the images as the sum of squared image differences. This is not a critical choice, and other similarity criteria can be used instead, such as mutual information (Pluim et al., 2003; Skouson et al., 2001), cross-correlation (Andronache et al., 2006), etc.

The direct similarity error term E_{S}^{ij} between a source image I_i and a target image I_j is defined as

$$E_{\mathrm{S}}^{ij} = \frac{1}{\#\Omega_{ij}} \sum_{\mathbf{x} \in \Omega_{ij}} \left(I_j(\mathbf{x}) - I_i(g^{ij}(\mathbf{x})) \right)^2 , \tag{4.3}$$

where Ω_{ij} defines a set of relevant pixels common to the images I_i and I_j that can be defined by masks, and where $\#\Omega_{ij}$ is the total number of pixels under the mask.

In the bidirectional case, the similarity error E_{S} between two images I_i and I_j, is defined as $E_{\mathrm{S}} = E_{\mathrm{S}}^{ij} + E_{\mathrm{S}}^{ji}$. Finally, the similarity error for CTR, E_{S} can be written as the sum of the direct, E_{DS}, and the inverse, E_{IS}, similarity errors: $E_{\mathrm{S}} = E_{\mathrm{DS}} + E_{\mathrm{IS}}$ where $E_{\mathrm{DS}} = E_{\mathrm{S}}^{12} + E_{\mathrm{S}}^{23} + E_{\mathrm{S}}^{13}$ and $E_{\mathrm{IS}} = E_{\mathrm{S}}^{21} + E_{\mathrm{S}}^{32} + E_{\mathrm{S}}^{31}$.

Since this similarity measure is sensitive to linear transformations of the image gray values, we assume that all images use a common intensity range, e.g. 0 to 255.

4.2.4 Consistency Term

The consistency error E_{C}^{ij} is the Euclidean distance between a point $\mathbf{x}$ of the source image I_i and the same point after a forward and backward transformation $g^{ji}(g^{ij}(\mathbf{x}))$. Therefore, the consistency error E_{C} between two images I_i and I_j is given by

$$E_{\mathrm{C}} = E_{\mathrm{C}}^{ij} \quad + \quad E_{\mathrm{C}}^{ji}, \tag{4.4}$$

where

$$E_{\mathrm{C}}^{ij} = \frac{1}{\#\Omega_{ij}} \sum_{\mathbf{x}\in\Omega_{ij}} \left\| \mathbf{x} - g^{ji}(g^{ij}(\mathbf{x})) \right\|^2 . \tag{4.5}$$

The UPR energy functional does not have a consistency term.

We now extend the consistency term for groups of three images (CTR method). To this end, we do not need to consider the consistency of g^{13} and g^{31}, since they are defined by composition (see Section 4.2.2) and their consistency is ensured by that of the intermediate deformations fields g^{12}, g^{23}, g^{21} and g^{32}. Therefore, the total consistency term is then given by $E_{\mathrm{C}}^{12} + E_{\mathrm{C}}^{23} + E_{\mathrm{C}}^{21} + E_{\mathrm{C}}^{32}$.

4.2.5 Image Representation

The target image I_j is always evaluated at integer positions while the source image I_i needs to be evaluated at generally non-integer coordinates, $g^{ij}(\mathbf{x})$. We opted for using cubic B-spline interpolation, since it offers a good trade-off between accuracy and speed (Unser et al., 1991). Therefore, we represent the source image I_i as

$$I_i(x, y) = \sum_{k,l\in\mathbb{Z}^2} c_{k,l} \beta^3 \left(\frac{x}{h} - k \right) \beta^3 \left(\frac{y}{h} - l \right), \tag{4.6}$$

where β^3 is a cubic B-spline, $c_{k,l}$ are the B-spline coefficients, and h is a parameter that controls the level of detail of the representation.

4.2.6 Deformation Representation

Taking advantage of the properties of the B-splines (Szeliski and Shum, 1996) we also represent the deformation fields as a linear combination of B-splines:

$$\begin{aligned} g^{ij}(\mathbf{x}) = \quad g^{ij}(x,y) \quad &= \quad \left(g_1^{ij}(x,y) \;\; g_2^{ij}(x,y)\right) \;= \\ &= \quad \sum_{k,l\in\mathbb{Z}^2} \left(c_{1,k,l}^{ij}, c_{2,k,l}^{ij}\right) \beta^3\left(\tfrac{x}{s_x} - k\right) \beta^3\left(\tfrac{y}{s_y} - l\right), \end{aligned} \tag{4.7}$$

where s_x and s_y are the sampling steps that control the degree of detail of the deformation field.

4.2.7 Optimization

To optimize the energy functional, we use a variation of the robust Levenberg-Marquardt method by Thévenaz et al. (1998). This method iteratively updates the deformation coefficients $\mathbf{c} = \mathbf{c}_{mkl}^{ij}$ so that $\mathbf{c}^{(n+1)} = \mathbf{c}^{(n)} + \Delta\mathbf{c}^{(n)}$, where $\Delta\mathbf{c}$ is the solution of $\tilde{H}\Delta\mathbf{c}^{(n+1)} = \nabla E(\mathbf{c}^{(n)})$, n is the iteration number; $\nabla E(\mathbf{c}^n)$ is the gradient of the energy with respect to the deformation coefficients evaluated at $\mathbf{c}^{(n)}$ and $\tilde{H}$ is a modified version of the Hessian matrix H with the diagonal components $\tilde{H}$ calculated as $[\tilde{H}]_{ii} = (1+\lambda)[H]_{ii}$. This algorithm achieves a gradual transition between quasi-Newton and gradient descent steps, controlled by the parameter λ. The parameter λ is adaptively modified according to the ability of $\mathbf{c}^{(n)}$ to minimize the energy functional. If the previous step succeeded to decrease the goal function, then the local model is considered appropriate and more weight is given to the second order information provided by the Hessian. Consequently, the next iterative step of the optimization algorithm will be more Newton-like. If the previous iterative step did not decrease the criterion, the local model is considered inappropriate and the optimization algorithm will retry the last step, thus behaving more like a gradient descent. We compute a Broyden-Fletcher-Goldfarb-Shanno (BFGS) approximation of the Hessian (Press et al., 1992) using the algorithm described by Sorzano et al. (2005). The BFGS approximates the Hessian as a semi-definite matrix, thus assuring the stability of the quasi-Newton optimization algorithm. The Hessian estimated this way is initialized by a diagonal approximation and is updated only on successful estimates $\mathbf{c}^{(n)}$ and when the positive definite quality of the estimated is assured.

Our optimizer makes extensive use of the derivatives of the different energy terms with respect to the deformation coefficients. Since the images

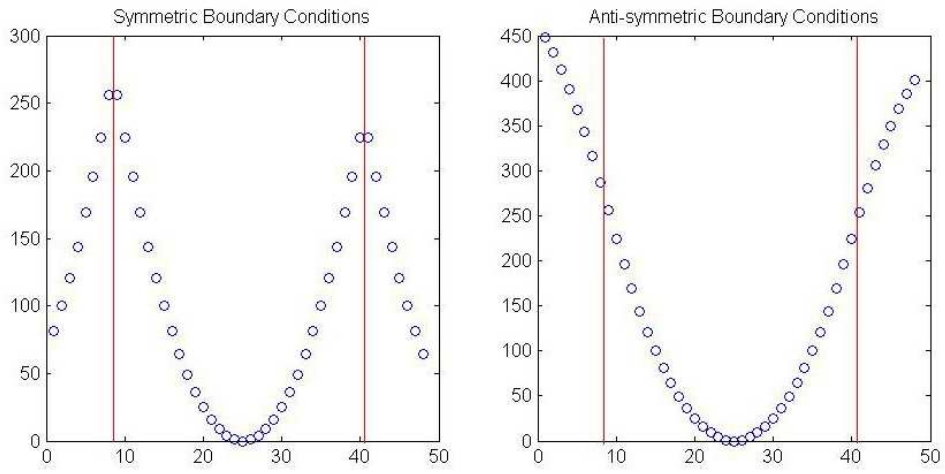

(a) (b)

Figure 4.2: Example of symmetric (4.2a) and anti-symmetric (4.2b) boundary conditions for a quadratic function. Vertical lines represent the boundaries.

and the deformation fields are expressed in B-splines basis, these derivatives can be computed explicitly and efficiently (Appendix B.1.1 and B.1.2).

4.2.8 Multiresolution

All images and deformations are represented using multiresolution pyramids (Unser et al., 1993). The number of B-spline coefficients at pyramid level L is $2^L \times 2^L$ for $L = 0, 1, 2...$ The algorithm starts using low-resolution versions of the images and deformations, finds the minimum of the energy functional and then moves to the next pyramid level, using the deformation obtained in the lower level as the starting point of the next —upper— level. This is repeated until the highest resolution level of the pyramid is reached.

To move between pyramid levels, customized reduction and expansion operators were used (Unser et al., 1993) (see Appendix B.1.3 for a technical explanation), resolved at the image and deformation borders using the appropriate boundary conditions. For the images we used standard symmetric boundary conditions. For the deformation fields, symmetric mirror conditions do not properly account for the deformation trend at the boundaries, and thus we applied anti-symmetric boundary conditions (Figure 4.2).

The following straightforward experiment shows the benefit of using anti-symmetric over symmetric boundary conditions to represent the deformation fields. We first applied a barrel/pincushion (Ma et al., 2003) deformation to a 256×256 pixel image of a uniform grid (Figure 4.3). This type of deformation is very relevant in this context because it preferentially affects the borders of the image. If the input coordinate $\mathbf{x}$ is normalized to lie in $[1, -1] \times [1, -1]$, and if r_{in} is the radius of its polar expression in this coordinate system, then the output radius r_{out} produced by the distortion is $r_{\text{out}} = 1 + k_1 r_{\text{in}}^2 + k_2 r_{\text{in}}^4$. Thus, the type of barrel pincushion deformation is given by the signs of k_1 and k_2. Thus, $k_1 < 0$ and $k_2 < 0$ ($k_1 > 0$ and $k_2 > 0$) generates a barrel (pincushion) deformation. We represented the deformation using 16×16 B-spline coefficients with k_1 and k_2 set to 0.10. Then, we reduced the deformation field to 8×8 coefficients using both symmetric and anti-symmetric boundary conditions and subsequently expanded them back. To compare the effect of the boundary conditions, we calculated the difference between the original and the reduced and then expanded deformation fields, for both the symmetric and anti-symmetric case. Figure 4.4 shows a detail of the upper left corner of the difference image, where the effect of the boundary conditions should be more pronounced. It is clear from the image that anti-symmetric mirror conditions preserve the deformation field better than their symmetric counterpart. Note also that the anti-symmetric boundary conditions force the second derivatives to be zero at the boundary, which is convenient when working with distortions that have small high order derivatives.

4.2.9 Consistent Sequential Registration

We have further extended the idea of CTR to do Consistent Sequential Registration (CSR). To this end, at each resolution level, triples of images are iteratively CTR-registered forward and backward until either the desired degree of accuracy or a maximum number of iterations is reached. Registering backward and forward iteratively refines the intermediate results incorporating contributions of all the members of the sequence to the registration process. See Algorithm 1 for a formal description.

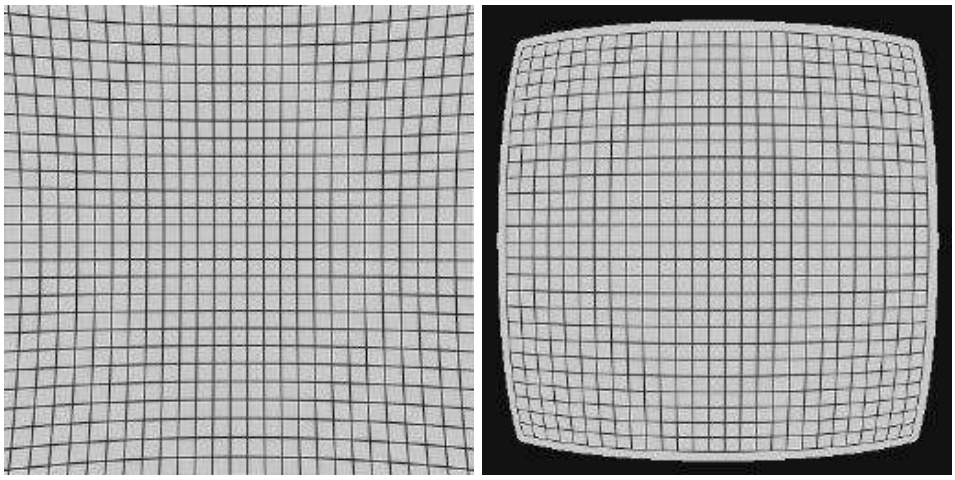

(a) (b)

Figure 4.3: (4.3a) Pincushion distortion ($k_1 = 0.10$ and $k_2 = 0.05$) of a uniform grid and (4.3b) its inverse barrel transformation ($k_1 = -0.10$ and $k_2 = -0.05$).

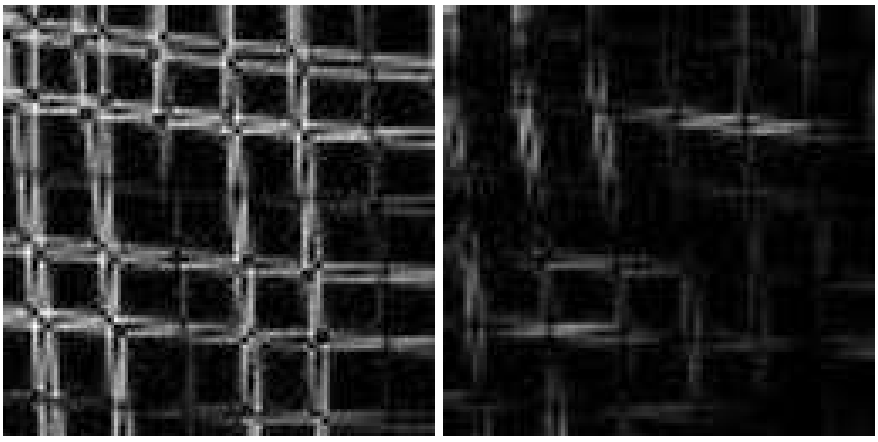

(a) (b)

Figure 4.4: Upper left corner of the difference image between 16×16 B-spline coefficients barrel/pincushion deformation and its 8×8 coefficients reduced and then expanded version using symmetric boundary conditions (4.4a) and anti-symmetric boundary conditions (4.4b).

Algorithm 1: Consistent Sequential Registration method

Input: $S \leftarrow$ A sequence of images I_i, $i = 1...N_S$

Initial transformations: $g_{i,i+1}$, $g_{i+1,i} \leftarrow$ Identity $\forall i \in [1, N_S - 2]$
Auxiliary transformations: g_{12}, g_{21}, g_{23}, $g_{32} \leftarrow$ Identity
foreach *pyramid level* **do**
    while *not (convergence* or max num of iterations) **do**
        for $i := 0$ *to* $N_S - 2$ **do** Forward registration
            $g_{12} \leftarrow g_{i+1,i+2}$, $g_{21} \leftarrow g_{i+2,i+1}$, $g_{23} \leftarrow g_{i+2,i+3}$, $g_{32} \leftarrow g_{i+3,i+2}$
            Do tri-wise registration of I_i, I_{i+1}, I_{i+2} with initial transformations g_{12}, g_{21}, g_{23}, g_{32}
            Save $g_{i,i+1}, g_{i+1,i}$, $g_{i+1,i+2}$, $g_{i+2,i+1}$
        end
        for $i := N_S - 3$ *down to* 0 **do** Backward registration
            $g_{12} \leftarrow g_{i+1,i+2}$, $g_{21} \leftarrow g_{i+2,i+1}$, $g_{23} \leftarrow g_{i+2,i+3}$, $g_{32} \leftarrow g_{i+3,i+2}$
            Do tri-wise registration of I_i, I_{i+1}, I_{i+2} with initial transformations g_{12}, g_{21}, g_{23}, g_{32}
            Save $g_{i,i+1}, g_{i+1,i}$, $g_{i+1,i+2}$, $g_{i+2,i+1}$
        end
    end
end

4.3 Experimental Results

4.3.1 Validation of the method using synthetic images

4.3.1.1 Accuracy

We first tested the performance of our CSR algorithm using synthetic image sets. To this end, we applied twenty known deformations g^* to an image and then performed the registration of the image and all its warped versions. Figure 4.5 shows the image that we used, a standard histology section of human breast epithelium stained with Hematoxylin and Eosin (H&E), captured at 40x magnification.

To deform the images, we used the barrel/pincushion distortion (Ma et al., 2003), which is characteristic of image acquisition and displaying devices such as cameras and monitors. Note that this choice does not favor B-splines, because these distortions can not be exactly represented in a B-spline space. Zero-mean Gaussian noise with standard deviation 0.05 to k_1 and k_2 was added to the images. To register the images we used a 4 level deformation pyramid and a 5 level image pyramid, i.e. a grid of 8×8 B-spline coefficients in the maximum detail level of the deformation pyramid and 16×16 B-spline coefficients in the highest resolution level of the image pyramid. We used 1.0 as similarity weight w_s and 20.0 as consistency weight w_c.

Let g be the transformation function obtained using CSR algorithm. We measured the accuracy of the registration using the standard *warping index* (Thévenaz et al., 1998) defined as

$$\varpi = \sqrt{\frac{1}{\parallel R \parallel} \sum_{\mathbf{x} \in R} \|g(\mathbf{x}) - g^*(\mathbf{x})\|^2}, \tag{4.8}$$

where $\parallel R \parallel$ is the number of image pixels. The warping index measures the average geometric error —in pixels— between the deformation applied to the image and the transformation calculated by our algorithm. The original average warping index of the unregistered images was 4.50 ± 3.50 pixels. The warping index after our sequential registration was 0.07 ± 0.05 pixels, i.e. the error was reduced to subpixel level.

4.3.1.2 Registration of cyclical data

The iterative, bidirectional —forward and backward— way our CSR algorithm aims at the optimum registration transformation, allows information

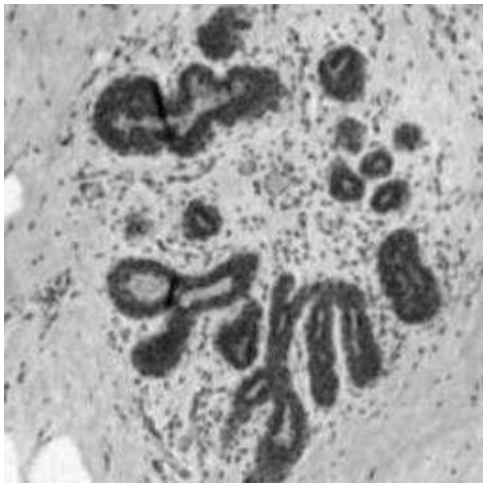

Figure 4.5: H&E stained section of human breast epithelium.

from the whole set of images to be used in the registration process. This makes the algorithm suitable for registering sequences of images, especially if they are cyclical. In order to test this, we used a Macaca fascicularis brain section stained with cholinesterase. We applied 18 rotations to the image at 20 degree intervals, the last image of the sequence therefore being equal to the first one. Then we evaluated the results of the UPR, CPR and CSR algorithms by registering all 18 images and comparing the first and last images. We used $w_s = 1.0$ and $w_c = 10.0$. As expected, our sequential CSR method was more efficient for this type of sequences than the two other algorithms (Table 4.1). Note that the mean squared error (MSE) and the standard deviation (STD) obtained using CSR are half the ones obtained using either UPR or CPR. Furthermore, the CSR maximum intensity difference (MAX) is almost one fourth of the ones obtained using UPR or CPR. Figure 4.6 shows the registration error visually for all three methods. We calculated and compared the percentage of correctly aligned pixels. For this, we converted the RGB images to HSV and set an acceptance threshold value of $\pm\frac{\pi}{25}$ that corresponds to a yellow hue value. CSR outperformed the other two methods: CSR produced 79.28% overlap compared to 55.99% (UPR) and 67.30% (CPR).

	UPR	CPR	CSR
MSE	1494.38	1264.22	**715.24**
Std	2745.29	2559.83	**1499.46**
Min	0	0	**0**
Max	31684	29929	**22201**

Table 4.1: Mean Squared Error (MSE), Standard Deviation (Std), Minimum (Min) and Maximum (Max) intensity difference between the original and the result after the combined rotations from the experiment described in Section 4.3.1.4 for the new algorithm (CSR) and the previous methods (UPR and CPR).

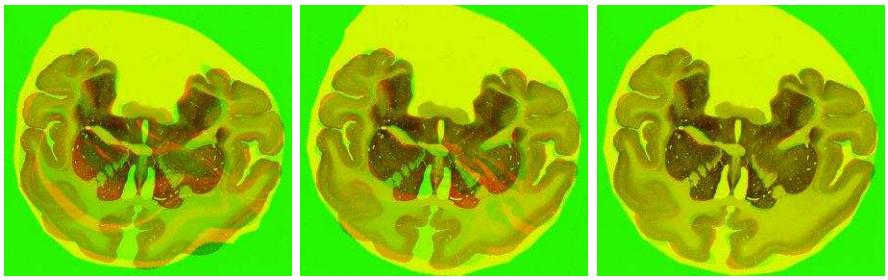

Figure 4.6: Visual estimation of registration accuracy of UPR (left), CPR (middle) and CSR (middle). A cyclical sequence -18 rotations of 20 degrees- of a Macaca fascicularis brain section was registered using the three methods. The original image is shown in green and the final transformed image is in red. Therefore, yellowish areas are regions of perfect overlap while red and green areas represent incorrect alignment.

	Non-CSR	CSR
DSE	60.75 ± 143.50	32.48 ± 4.00
ISE	142.72 ± 255.78	33.72 ± 8.91

Table 4.2: Average and Standard Deviation of the Mean-Squared Error for the direct/inverse similarity (DSE/ISE) for the synthetic experiment of Non-Consistent Sequential Registration (Non-CSR) vs CSR

4.3.1.3 Use of neighbor information

Next we showed the benefits of using versus non using the consistency information. To this end we used the same sequence of Monkey brain sections used in the previous section and registered the sequence in groups of three images, first without consistency and then using our complete CSR algorithm ($w_c = 10.0$). In both cases we used a 4 level multiresolution image pyramid and a 3 level deformation pyramid, with $w_s = 1.0$. As it can be seen in Table 4.2, our method substantially improved the registration results . To estimate the invertibility of the transformations calculated by both methods, we can look at the final (direct and inverse) consistency errors: 2243.50 ± 7387.42 and 2421.08 ± 6678.07 for the non-consistent method and 1.69 ± 1.39 and 1.58 ± 1.16 for our CSR method.

4.3.1.4 Robustness against outliers

To further refine and explain the benefit of using CTR as the building block of CSR, versus using UPR (Sorzano et al., 2005) or CPR (Arganda-Carreras et al., 2006) we used groups of three images where one of the members had been heavily distorted. This way we show the improvement obtained when combining consistency, bidirectionality and groupwise —in this case tri-wise— registration.

First, we used seven groups of three images from the sequence of 20 distorted version of the image in Figure 4.5 used in Section 4.3.1.1 adding random noise (with 50% of randomization, i.e. percentage of affected pixels) to one of the images of each group (see Figure 4.7). Then we registered triples using UPR, CPR and CTR with a 4 level image pyramid and a 5 level deformation pyramid. We used $w_s = 1.0$ and $w_c = 20.0$. The average warping indexes obtained were 14.96 ± 18.72 (UPR), 5.12 ± 5.33 (CPR) and 3.67 ± 3.77 (CTR). This shows the improvement obtained by using a consistent method compared to a non-consistent one, as well as the benefit

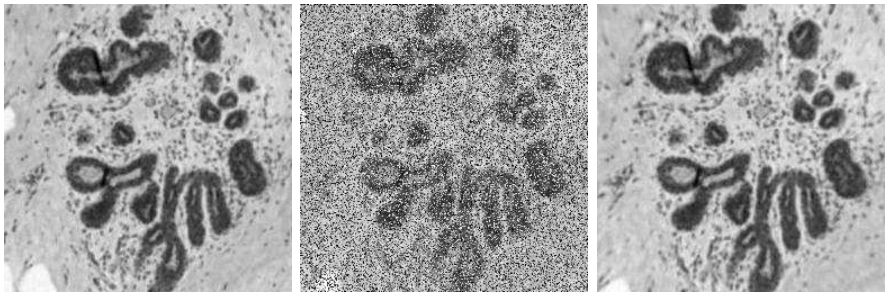

Figure 4.7: Example of triple histology images used in the validation test. A significant amount of random noise was added to the middle image.

of a tri-wise method over a pairwise method when one of the elements in the series is heavily distorted.

Next, we tested the robustness of our algorithm against independent, non-correlated rotations. This is an interesting problem from a practical point of view because it is very common in sequences of manually processed histological sections. We used ten groups of three images taken from a sequence of Macaca fascicularis brain sections stained with cholinesterase (grayscale, 300×282 pixels size). We then rotated one of the images of the triple a random number of degrees, uniformly distributed between 20 and 30. See Figure 4.8 for an example. We used $w_s = 1.0$ and $w_c = 10.0$. The registration results, shown in Table 4.3 confirm that CTR is more robust against outliers than UPR and CPR. Our CTR method achieves the lowest similarity error values while keeping moderate consistency error levels. CPR gives intermediate values for the similarity error while obtaining the best values for the consistency error. This is explained by the fact that CTR jointly minimizes the similarity error of three images (6 dissimilarity measures) and the consistency error of two direct transformations with their corresponding inverse in both directions (4 consistency measures), while in the two equivalent CPRs of the same images, the optimizer minimizes separately the dissimilarity of both pairs of images (4 dissimilarity measures) and their corresponding direct-inverse transformations (4 consistency measures).

4.3.1.5 Effect of the Consistency Term

Finally, we have studied the behavior of the tri-wise algorithm in terms of similarity error and the impact of our consistency term compared to the

Figure 4.8: Example of a triple of Macaca fascicularis brain sections, stained with cholinesterase. The third image of the trio was artificially rotated 25 degrees.

	UPR	CPR	CTR
DSE	543.21 ± 23.10	497.23 ± 97.84	$\mathbf{398.48 \pm 66.29}$
ISE	570.86 ± 30.67	489.65 ± 81.66	$\mathbf{450.29 \pm 51.15}$
DCE	15.28 ± 2.08	$\mathbf{2.15 \pm 1.38}$	8.59 ± 6.86
ICE	14.84 ± 1.28	$\mathbf{2.01 \pm 1.53}$	10.57 ± 4.09

Table 4.3: Average and Standard Deviation of the Mean-Squared Error for the direct/inverse similarity (DSE/ISE) and the direct/inverse consistency (DCE/ICE) for the synthetic rotation experiment described in Section 4.3.1.4 for the new algorithm (CTR) and the previous methods (UPR and CPR).

previously described regularization term by Sorzano et al. (2005). To this end, we used the first triple of the sequence of images described in the previous Section (monkey brain section rotated 0, 20 and 40 degrees). We then applied a tri-wise image registration using a 4 level multiresolution image pyramid, a 3 level deformation pyramid and either:

1. only the similarity term of our energy functional (4.1), or
2. the similarity term plus a vector-spline regularization with two subterms, one based on the gradient of the divergence of the deformation fields and one based on the gradient of their curl (Sorzano et al., 2005), or
3. the similarity term plus our consistency term.

The results of the convergence of the three methods are shown in Figure 4.9. Adding a regularization or consistency term to the energy function increases the complexity of the goal function to be optimized but in return forces the deformations to be smooth, which usually helps reducing the global similarity error E_S. When comparing both scenarios, it is clear that using a consistency term instead of using regularization produces significant improvement in the final value of the similarity error, with the additional advantage of obtaining also the inverse transformations. Additionally, in our case the number of deformation coefficients is sufficiently low so as to not need to be regularized. This is therefore the choice when no prior knowledge about the deformation exists. However, if a priori information about the deformation is known, adding an appropriate regularization term to the energy functional can greatly improve the results (Sorzano et al., 2005).

4.3.2 Experiments with real image sequences

We now show the results of using CSR to align real image sequences.

4.3.2.1 Robustness against non invertible transformations

We first show how CSR can efficiently correct heavy distortions, such as those caused by folding and tearing in histological tissue sections. As a reference, we compare our CSR algorithm with Vercauteren's Diffeomorphic Demons (VDD) method (Vercauteren et al., 2007), a non-parametric diffeomorphic registration algorithm that generalizes Thirion's diffeomorphic demons (Thirion, 1998). We used consecutive 50 nm thick Transmission Electron Microscope (TEM) sections of Lamina tissue from *Drosophila*

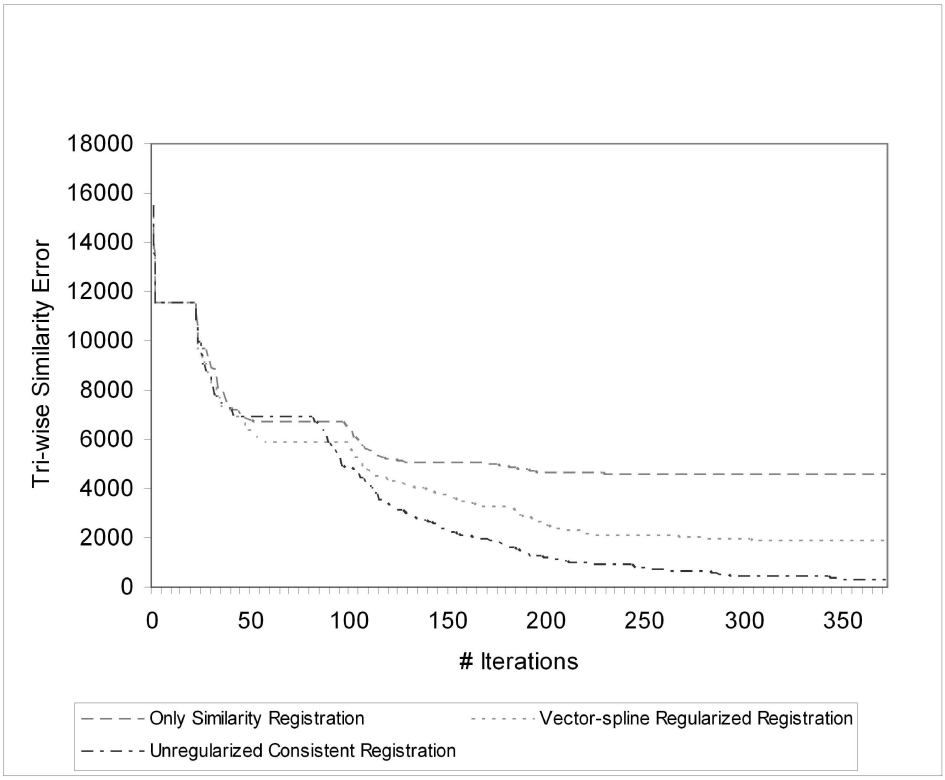

Figure 4.9: Evolution of the similarity error with the number of iterations for the non-regularized non-consistent, regularized non-consistent and non-regularized consistent tri-wise registration of the first image triple used in Section 4.3.1.2.

Melanogaster. All images were acquired at 3500x magnification, 512×512 pixel size. These extremely thin tissue sections are often folded or torn, making the registration a very difficult task. An example of this is shown in Figure 4.10, which shows two consecutive TEM sections, one of them (Figure 4.10b) severely affected by a folding area —black stripe in the middle of the section—. We applied our CSR registration —adding a third section to complete a triple— and then VDD, obtaining a direct similarity error at convergence of 3306.38 (CSR) and 4546.82 (VDD). The corresponding deformation maps (Figure 4.10c and 4.10d) show how the CSR method is able to identify and correct the folding area.

To further compare the performance of CSR with other standard registration methods, we used a set of 14 TEM Lamina sections (512×512 pixel size). The TEM image sequence was registered using CSR, VDD and a combined method consisting of an initial affine registration followed by unidirectional elastic registration with conjugate gradient optimizer (UER), which is part of the open-source toolkit *elastix*. All methods used the same initial conditions: 4 levels of multiresolution image pyramid, 8×8 deformation coefficients at the finest level, and the same stopping threshold (0.01), i.e. desired level of precision (absolute error difference between last and previous level registration). To evaluate the results, several cells of the tissue were manually segmented by an expert. The average cell overlap after registration was $69.86 \pm 34.09\%$ (VDD), $78.48 \pm 17.77\%$ (UER) and $83.91 \pm 6.06\%$ (CSR). If we only consider the image triples containing some torn tissue (as in 4.10b) the improvement of using CSR is even more clear: $11.95 \pm 20.63\%$ (VDD), $51.06 \pm 20.40\%$ (UER), and $76.93 \pm 10.53\%$ (CSR). The result can be visualized by reslicing the sequence of sections and comparing it with the original alignment (Figure 4.11a), the diffeomorphic demons alignment (Figure 4.11b), the UER result (Figure 4.11c) and the CSR result (Figure 4.11d).

These results confirm with real image series our previous results our previous results obtained in synthetic data sets, i.e that CSR is especially beneficial when one or several images of the sequence are heavily distorted.

Figure 4.12 shows the segmented cells —in red— and the sequence of 14 CSR aligned TEM sections from the previous experiment. This way, we can see the segmented cells in a completely aligned 3D environment.

4.3.2.2 Registration of brain histological sections

We finally registered nine consecutive coronal cuts of Macaca fascicularis stained with cholinesterase. The images were grayscale, 300×282 pixels size.

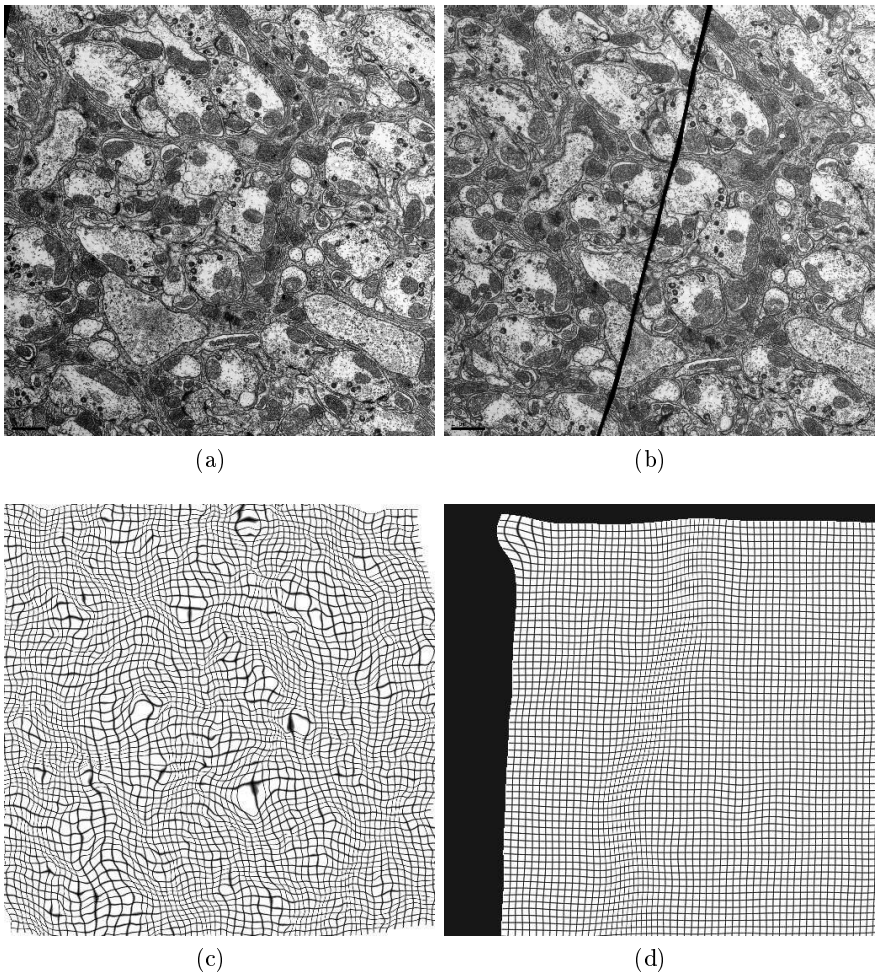

(a) (b)

(c) (d)

Figure 4.10: Correction of heavy distortion. Two consecutive TEM tissue sections (4.10a) where the second one (4.10b) is folded in the middle. (4.10c) Deformation grid after diffeomorphic registration (Vercauteren's method). (4.10d) Deformation grid after CSR.

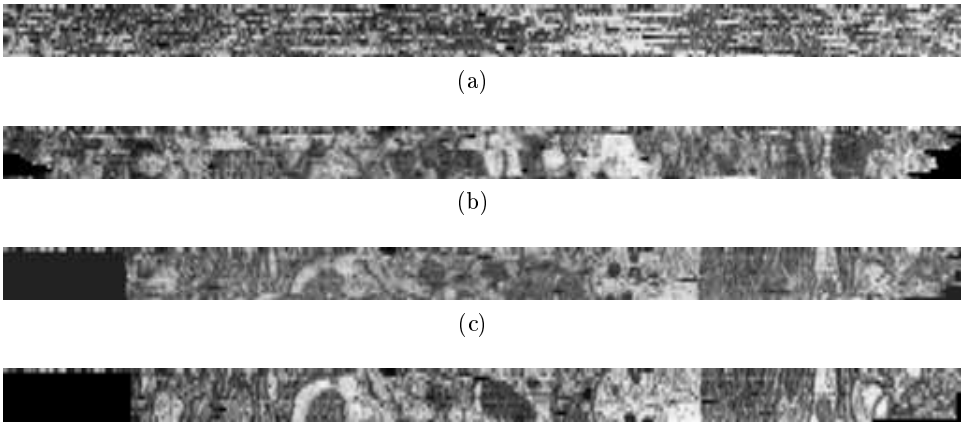

(a)

(b)

(c)

(d)

Figure 4.11: Center section after reslicing the sequence of TEM images from the top of the stack: (4.11a) original misaligned sequence, (4.11b) diffeomorphic demons results, (4.11c) UER results and (4.11d) CSR results.

The registration algorithm used a 5 level multiresolution image pyramid and a 4 level deformation pyramid, with 1.0 as similarity weight and 10.0 as consistency weight. We set empirically the stopping threshold to 0.01 and the maximum number of iterations (i.e. whole sequence registration in the corresponding level) to 10.

This sequence presents challenges to any image registration algorithm since one of the brain slices is badly torn (7th slice) and there are important differences between slices due to the distance between sections. However, our method achieved a very satisfactory result, as can be seen in Figure 4.13. The initial dissimilarity error 2122.00 ± 426.36 was reduced to 375.27 ± 88.97, while VDD and UER only achieved 617.93 ± 348.73 and 610.34 ± 159.32, respectively. This significant difference in the minimization of the similarity error with respect to the previous example is due to the higher level of pyramid resolution and especially to the flat light background of the brain images. The registration time was 90 minutes running on an Intel Pentium M, 1.59 GHz, with 2GB of RAM memory, under Linux SuSE 10.0. The contours of the structures of interest were satisfactorily aligned, as can be seen in Figure 4.14.

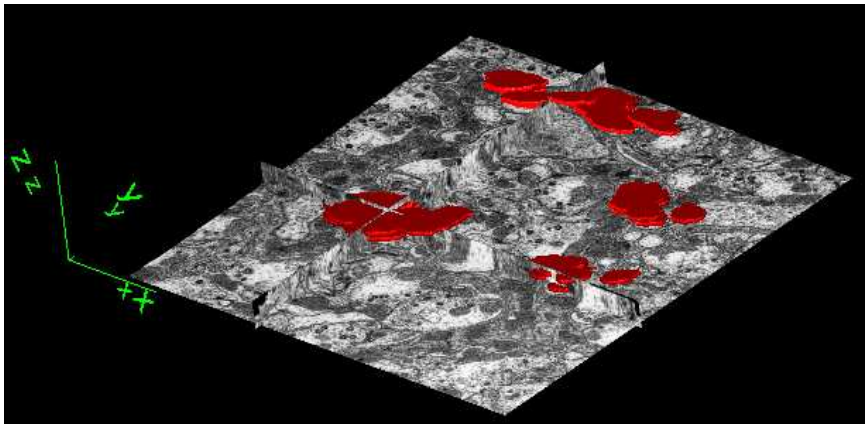

(a)

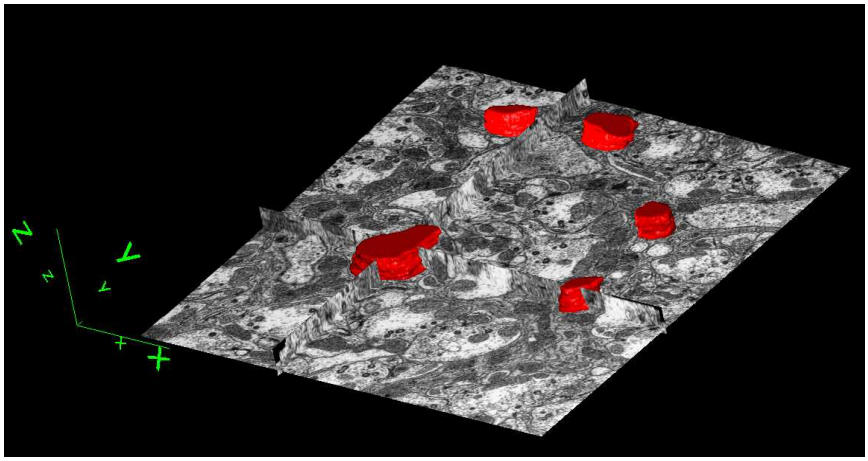

(b)

Figure 4.12: 3D reconstruction of registered Lamina TEM sections with some segmented cells before (4.12a) and after alignment (4.12b). The tissue is displayed in an orthoslice fashion to better appreciate the isosurfaces of the segmented cells (in red).

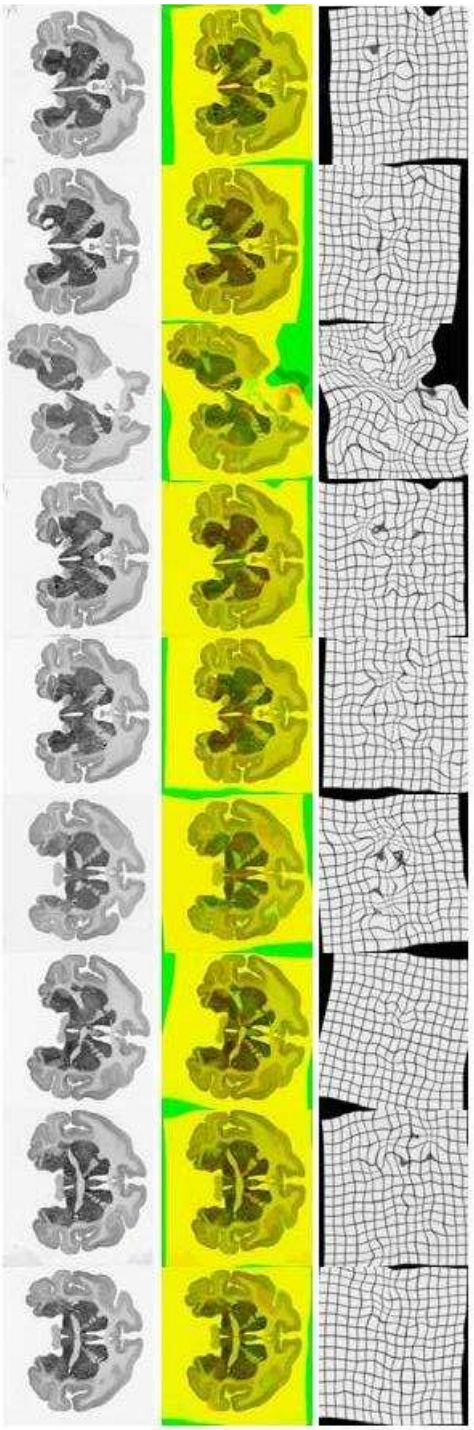

Figure 4.13: Sequence of Macaca fascicularis brain sections stained with cholinesterase. From left to right: original histology sections, RGB images showing some direct and inverse CSR results (yellow color meaning perfect superposition and red and green colors pointing out the misalignment regions) and their corresponding deformation grids.

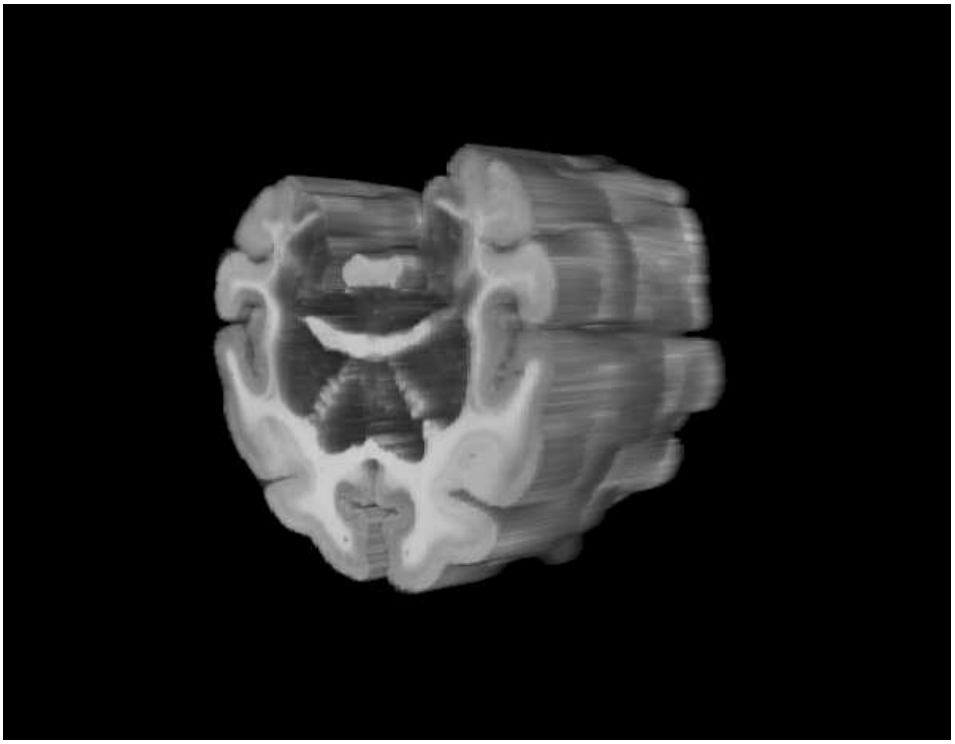

Figure 4.14: 3D reconstruction of registered Macaca fascicularis brain sections stained with cholinesterase.

4.4 Conclusions

We have introduced a novel, automatic landmark-free method for registration of 2D image sequences. Our method uses consistency, elasticity and full bidirectionality to register series of related images in a multiresolution fashion. We have profited from the B-spline theory to implement both images and deformations with multiresolution spline pyramids, which produces a general, flexible and computationally efficient solution to the registration problem. Furthermore, we chose a very powerful optimizer with the BFGS estimation of the Hessian, which combines steepest-descent and quasi-Newton steps in order to speed up convergence. In principle, the deformations represented by B-splines are not invertible, however and thanks to the enforced consistency of the transformation fields, we obtain deformations that are quasi-inverse of each other. Moreover, the method spreads the information from the neighbors through the whole set of images enforcing the consistency of the whole sequence.

As shown in Section 5.3, this algorithm reduces the warping index of synthetic images to sub-pixel level, even when the artificially generated deformation belongs to a space that cannot be exactly represented using B-splines. These results are better than those obtained using classic pairwise unidirectional or bidirectional (consistent) registration algorithms. Besides, we have shown that our algorithm is more robust than those methods against specific image adverse effects such as noise or large rotations. We believe that this increase in robustness is due to the combined use of consistency and global image information, provided the iterative, back and forth tri-wise registration algorithm, which assigns equal relevance to all the images of the sequence.

Finally, although our algorithm allows using both landmarks and deformation regularization, we show that registering using the consistency constraint provides satisfactory, unbiased results without requiring the use of a landmarks or a regularization term. This is especially useful when no information about the deformations exists that may be used to customize the regularization term and the number of deformation coefficients is sufficiently low. Using these improvements, we show the benefit of applying iteratively tri-wise bidirectional consistent registration to sequences of images and in particular to series of TEM and histological images.

Acknowledgments

Zhiyuan Lu and Marta Rivera-Alba are gratefully acknowledged for providing the Lamina TEM image sequence and bringing always interesting discussions. This work benefited from the use of *elastix*, software developed by Stefan Klein and Marius Staring, carried out at the Image Sciences Institute (ISI), on funding granted by the Netherlands Organization for Scientific Research (NWO). It is available at `elastix.isi.uu.nl`. Xabier Artaechevarria is especially acknowledged for providing continuous help and support on *elastix*.

5

3D Reconstruction of Histological Sections

"Who are you going to believe, me or your own eyes?"

Groucho Marx

Abstract

In this chapter, we present a novel method for the automatic 3D reconstruction of thick tissue blocks from 2D histological sections. The algorithm completes a high-content (multi-scale, multi-feature) imaging system for simultaneous morphological and molecular analysis of thick tissue samples. This computer-based system integrates image acquisition, annotation, registration and three-dimensional reconstruction. We present an experimental validation of this tool using both synthetic and real data. In particular, we present a 3D reconstruction of a entire mouse mammary gland.

5.1 Introduction

The mammary gland is a ductal tree that develops during puberty. In neonate mammals, mammary epithelium consists of a branched sprout contiguous with the nipple. During puberty, there is considerable growth of the ductal tree to invade and fill the fat pad where it is embedded. In the adult animal, ducts are formed by secretory, luminal epithelial cells. Contractile myoepithelial cells surround the ducts. The interrelationship between the three-dimensional structure of the mammary gland (macroarchitecture)

and its cellular composition (microarchitecture) has been only described in a qualitative way in studies on humans and animal models. This is mainly due to the lack of 3D imaging methods to simultaneously capture the morphology of the gland and the phenotype of its constituent cells, defined by the morphology and the expression of specific markers within the cells.

Some studies are based on whole mount preparations (Cleary et al., 2004; Bagheri-Yarmand et al., 2003; Giovanni et al., 2004; Westerlind et al., 2002). These studies provide a global picture of the development of the mammary gland along with information about the quantity and spatial distribution of its different morphological structures: primary and secondary ducts, lobular units, etc. Even before the use of digital image processing, a standard for the evaluation of whole mount samples was established (Russo and Russo, 1978a,b). The preparations were imaged with conventional analog cameras and analyzed by manual and rather tedious methods. The use of digital tools gave a significant boost to the analysis of whole mount preparations. Thanks to this technology, some studies in mammary development in rats with manual measures and counts of epithelial areas and lobular terminal units appeared (Ip et al., 1999).

The whole mount analysis allows a macroscopic analysis of the gland, but it is generally restricted to two dimensions. A further step is necessary and possible thanks to the 3D microscopy technologies, such as real-time stereo-microscopy or confocal microscopy. Stereo-microscopes have been used to visualize the morphology of mammary gland epithelial cells in rats (Hayward et al., 1996), to calculate the epithelial density of the gland (Hadsell et al., 2003; Hilakivi-Clarke et al., 1997), to measure the penetration of the ducts and the number of branches per millimeter of duct (Wiseman et al., 2003), etc. Confocal microscopy has been used to visualize the three-dimensional architecture of whole mounts of mammary glands in transgenic mice (Chang et al., 2004) and to reconstruct samples of human breast (Liu et al., 1997). These methods do not allow combining macro- and microscopic data to study how they relate to each other. Another advantage of the 3D microscopy methods is that the images do not need registration or annotation since the sample is not moved during acquisition. However, the analysis of the whole mammary gland at macroscopic level is not feasible.

All these microscopy modalities —confocal microscopy, two-photon excitation microscopy, etc.— do not provide enough resolution. In the best-case scenario, using the most modern technology, one can visualize 200-300 microns into the sample. However, the complexity of the mammary gland stroma affects both the light transmission and the staining performance and reduces the vision capability to 20-30 microns depth. Thus, a different tech-

nique with larger resolution is necessary.

In a recent and noteworthy extension of the previous method, Capek et al. (2009) approached this problem by physically sectioning the specimens in 40 micron sections and then acquiring image stacks that were stitched in the x-y plane and registered in the z —vertical— direction. This allows creating a complete digital version of the specimen. However, due to data management and analysis issues, this is only suitable for small tissue volumes. Another shortcoming of this method is that it relies on confocal imaging of fluorescent markers, which might be the best approach for high-resolution nuclear reconstruction, but is not the best staining strategy for low-resolution reconstruction of histological structures.

Our alternative to combine low resolution imaging of histological structures with high-resolution analysis of cellular expression relies on serial sectioning. Namely, after fixation, the tissue is embedded in paraffin and cut into thin slices (4-5 microns). The slides are stained to allow visualization of structures of interest. Even slices are stained with Hematoxylin & Eosin (H&E) to highlight the histological structures, and the intermediate odd sections stained by immunohistochemistry using antibodies against several cellular markers. The even sections are then imaged at low resolution and the odd section are imaged at high resolution. This way the cellular information can be traced back to the corresponding histological structures imaged in the contiguous sections. This requires being able to accurately reconstruct the tissue structures from the —low resolution— images of the even H&E stained sections. This chapter deals with the automatic reconstruction of entire tissue blocks in a way that could be later used to store the cellular level phenotypic information measured in the intermediate sections. This requires the system to be automatic, work at high resolution in the vertical direction and rely on elastic registration to account for non linear distortions, as it is described in the following paragraphs. Another important factor from the standpoint of the system usability is the integration of the acquisition, analysis and storage under a single platform, hiding the integration details to the end user.

As already described in Chapter 2, a topologically accurate rendition of tissues requires all the images of the sections to be correctly aligned, to ensure the continuity of structures crossing several sections. This is a very difficult task that involves correcting from both linear and non-linear distortions that can appear in the tissue. Using a manual, affine, non integrated approach, Capuco et al. (2002) manually registered and segmented histological sections —5 microns thick— with Adobe Photoshop and produced the 3D reconstruction of breast structures. Ohtake et al. (2001) used a similar method to re-

construct breast tumors from very thick sections —2 mm—. Streicher et al. (2000) presented a computerized method for three-dimensional visualization of embryonic gene expression and morphological structures from histological sections, but it is based on a rigid registration relying on markers (Streicher et al., 1997), manual segmentation and also dependent on different commercial tools and formats. There exist also non-commercial tools for 3D reconstruction of histological sections of other types of tissue and morphological structures, for instance *Reconstruct* (Fiala, 2005) and *TDR-3Dbase* (Verbeek et al., 1995). *Reconstruct* is used to render neuronal tissue and its registration and annotation steps are manual. In *TDR-3Dbase* all the steps are integrated but manual and the mesh reconstruction is very coarse.

Some other authors tried to combine the advantages of 3D microscopy with those of the histological sections by episcopic methods (Weninger et al., 1998; Weninger and Mohun, 2002). These methods do not required registration because the images are acquired at the same time of the sectioning process. However, they are quite limited in terms of resolution, because there is only one snapshot per image, i.e. not scanning, and in terms of staining, because there is only staining on the surface of the microtome. This limits the staining methods and prevents from the automation of the process. Again, these are non-integrated systems and depend on commercial tools.

MacKenzie-Graham et al. (2004) described another technique to produce renderings from histological sections in order to build a multi-modal (MRI, classical histology and immunohistochemistry) and multi-dimensional atlas of mice brain. They used thick sections (50 microns) and the registration method although automatic was limited to an affine transformation.

In this chapter we extended and combined our previous work with the system *R3D2* (see Chapters 2 and 3) in order to address those problems and accurately render images of consecutive sections of fully sectioned tissue blocks. In practice, our algorithm proceeds as follows: once the images are acquired from the microscope, they are automatically and rigidly registered. Next, the structures of interest are segmented and their resulting contours are automatically grouped. Finally, the registration is locally and/or elastically refined and the structures are reconstructed in 3D based on the grouped contours. We evaluated the system with an artificial model and then applied it to real mammary gland tissue blocks. We show the benefit of using these integrated techniques to finally generate realistic, smooth and compact 3D reconstructions of histological tissue at high resolution. These are indeed novel 3D views of such a biological tissue.

The structure of the chapter is as follows. First we describe the image acquisition technique in Section 5.2.1 and then we describe the methods

for rigid registration (Section 2.2.2), segmentation of structures of interest (Section 5.2.3), contours grouping (Section 5.2.4), local group registration (Section 5.2.5) and 3D rendering (Section 5.2.6). Next, we show experimental results, first with an artificial case in order to validate the algorithm (Section 5.3.1) and also with real histological data (Section 5.3.2). Finally, we discuss the conclusions of our approach in Section 5.4.

5.2 Methodology

5.2.1 Image Acquisition

As explained in Chapter 2, we used paraffin embedded tissue blocks containing either normal mouse mammary glands or human tissue biopsies of patients with ductal carcinoma in-situ (DCIS) of the breast. The blocks were fully sectioned at 5 microns thickness and stained with Hematoxyilin and Eosin (H&E), which highlights histological structures such as mammary ducts or tumors. All the sections were imaged at low resolution (2.5x) using a monochrome CCD camera without using any interference or absorption color filtering. The images were stored in either TIFF or ICS (Dean et al., 1990) format in sets of related images that we, again, refer to as **cases**.

5.2.2 Rigid Registration

The first step to a correct sections alignment is an affine approach using an automatic rigid-body registration method (see Chapter 2, Section 2.2.2 or Arganda-Carreras et al. (1-5 Sept. 2004)). This approach is not enough to produce proper 3D reconstructions of the tissue, but it facilitates the work of the following tasks (segmentation and contours grouping) and it can be refined later with local or non-rigid registration methods.

5.2.3 Segmentation of structures of interest

In order to automatically extract the contours of the features of interest we use a method (Fernandez-Gonzalez et al., 2004) that combines image processing techniques and two well-established schemes for interface propagation: the Fast-Marching method (Sethian, 1996) and the Level-Set method (Osher and Sethian, 1988; Osher and Fedkiw, 2002; Osher and Paragios, 2003). This approach starts by the background correction step. This is an important step, since the background pattern generated during image acquisition modifies the gradient of the image, and the speed function that it is used for

interface propagation depends on that gradient. Once the background has been corrected, the Fast-Marching method is run. This technique provides a good approximation of the boundaries of the objects that we are trying to segment in a very short time, since it assumes monotonic speed functions (always positive or always negative). Then the approximation provided by the Fast-Marching method is used as the initial condition for the Level-Set method. This is a computationally more expensive algorithm but it is run for just a few steps, enough to fit the front to the contours of the structures of interest, but not as many as to make the segmentation too time consuming.

5.2.4 Contours Grouping

In the segmentation step we annotate the structures of interest of our tissue: ducts, lymph nodes, etc. We group the contours that belong to the same structure so that they can be rendered together. We have developed an automatic grouping algorithm which proceeds in two steps. The first step assigns the same group number to the contours of consecutive sections if their projected bounding boxes —minimum squared areas containing the shapes— overlap. If there is not overlap the contour remains ungrouped. During this process, if the bounding box of a grouped contour overlaps an already grouped contour, then both contours receive the same super-group number. Following this idea we iteratively create a hierarchy of groups. In the second step, all the remaining ungrouped contours are assigned the group and super-group number of the closest grouped contour in the next section. See Algorithm 2 for a formal description.

5.2.5 Local Group Registration

As already mentioned before, the sectioning process can produce non-linear deformations in the tissue, such as folding, stretching, tearing... Occasionally also, some sections can be damaged beyond recovery and have to be disposed, thus introducing gaps in the sequence of sections of the case. All these effects may cause large misalignment between areas of the section that cannot be corrected by the initial rigid-body transformation.

In Chapter 2, Section 2.2.3, we introduced a local refinement based on the phase correlation method (PCM) by Kuglin and Hines (1975). It divided the sections in areas or sub-images and calculated a correction vector for each of those areas. However, some problems appeared when a contour was distributed in several of these areas. For that reason and now that we

Algorithm 2: Contours grouping algorithm

```
/*
Definitions:
BBox(c_x):  bounding box of contour c_x
GN(c_x):  group number of contour c_x
SGN(c_x):  super-group number of contour c_x
 */
1  N_g ← 0
2  forall sections S_i in the Case do
3      forall contours c_j in S_i do
4          BB_j ← BBox(c_j) projected in S_{i+1}
5          forall contours c_k in BB_j do
6              if [GN(c_j) ≠ ∅ and GN(c_k) ≠ ∅ and GN(c_j) ≠ GN(c_k)]
               then
7                  SGN(c_k) ← SGN(c_j)
8              else if GN(c_k) = ∅ then
9                  GN(c_k) ← GN(c_j)
10                 SGN(c_k) ← SGN(c_j)
11             else if GN(c_j) = ∅ then
12                 GN(c_j) ← GN(c_k)
13                 SGN(c_j) ← SGN(c_k)
14             else
15                 GN(c_j) ← GN(c_k) ← N_g
16                 SGN(c_j) ← SGN(c_k) ← N_g
17                 N_g ← N_g + 1
18             end
19         end
20     end
21 end
22 forall sections S_i in the Case do
23     forall contours c_j in S_i do
24         if GN(c_j) = ∅ then
25             c_closest ← closest contour in S_{i+1}
26             GN(c_j) ← GN(c_closest)
27             SGN(c_j) ← SGN(c_closest)
28         end
29     end
30 end
```

have automatically grouped all shapes in the case, we can extend the idea to match contours and areas. Therefore, our local registration algorithm generates now a common bounding box for each group of contours which were automatically detected in the previous step and calculates a correction vector for each of these groups. The correction vector is calculated using the cross-correlation between the bounding box in the target image and the corresponding bounding box in the source image. This source bounding box is defined from the rigid registration parameters if a previous rigid-body registration has been applied before to the image.

At the end of this process there will be a correction vector and a correlation coefficient for every group of contours in every section. The correlation coefficient is calculated between the original target sub-image and a new source sub-image, which is the result of applying the correction vector to the old source sub-image. Thus the correlation coefficient will provide a measure of the accuracy of the correction vector. The user can set here a minimum correlation threshold value. For values lower than this threshold the system will consider the areas as strongly distorted and it will call our consistent elastic registration routine (see Chapter 3 or Arganda-Carreras et al. (2006)) to correct the misalignment.

5.2.6 3D Reconstruction

The system reconstructs the 3D structures of interest based on the grouping (Section 5.2.4) of the segmented contours (Section 5.2.3). The contours are previously aligned following the registration results (Sections 5.2.2 and 5.2.5). The user can choose between rendering all contours belonging to the same group or to the same super-group as the same volume, and consequently with the same color. The surfaces of the volumes are created with a refined Delaunay triangulation (Boissonnat and Geiger, 1993). Some examples and validation experiments of the complete rendering process are shown in the next section. Alternatively, *R3D2* offers the option of creating a 3D binary image, containing the segmented and aligned contours in white and the background in black. This binary image can be used for further studies of the structures of interest such as generating their skeleton, counting and measuring their branches, volumes, etc. as it is shown in the next section.

5.3 Results

5.3.1 Validation of the method using a phantom

We validated our system by artificially simulating the most common problems found during the reconstruction of histological tissue. To this end, we create a model or *phantom* which, on one hand represents the type of structures we want to render and, on the other hand, can be manipulated to simulate the problems that appear with real data. Our phantom was an x-ray tomographic reconstruction of mice airways, with a tree-like structure similar to that of the mammary gland. We stored the model in a $444 \times 471 \times 568$ pixel 3D image. We calculated the isosurfaces of the structures of interest using *ImageJ 3D Viewer* (Schmid, 2008), a popular open source software which extracts the volume surface from the 3D image and allows storage in virtual reality modeling language (VRML) format. Figure 5.1 shows a view of the volume. We then used the model to study the robustness of our 3D reconstruction system to variations in the direction of tissue sectioning, the loss of sections and the presence of tissue distortions. Notice here that the structures of interest in this volume are smaller than in our histological tissue, but the size of the volume is also smaller thus preserving the proportion between structure sizes and the x-, y- and z- resolutions we expect from the histological samples. Although the tomographic volume is isotropic and the histological data is usually not, we assume the distance between sections is small enough to allow reconstructing those structures as we can do with the artificial model.

5.3.1.1 Direction of sectioning

Since *R3D2* does not work with input 3D images but 2D sections we first proceeded to create a set of slices from the model 3D image. We performed 3 different sectionings, in the x-, y- and z- axis, so we could test the performance of our system in any direction of cut. Thus, we obtained three sets of images which were processed as *R3D2* cases. For these three cases we followed the steps previously described in the Methodology: segmentation, grouping and rendering. At this point we did not perform any registration method because the sections preserved the alignment of the original 3D image.

We then compared the resulting isosurfaces with the original model surface. For this we used the Hausdorff distance (Rote, 1991), which measures

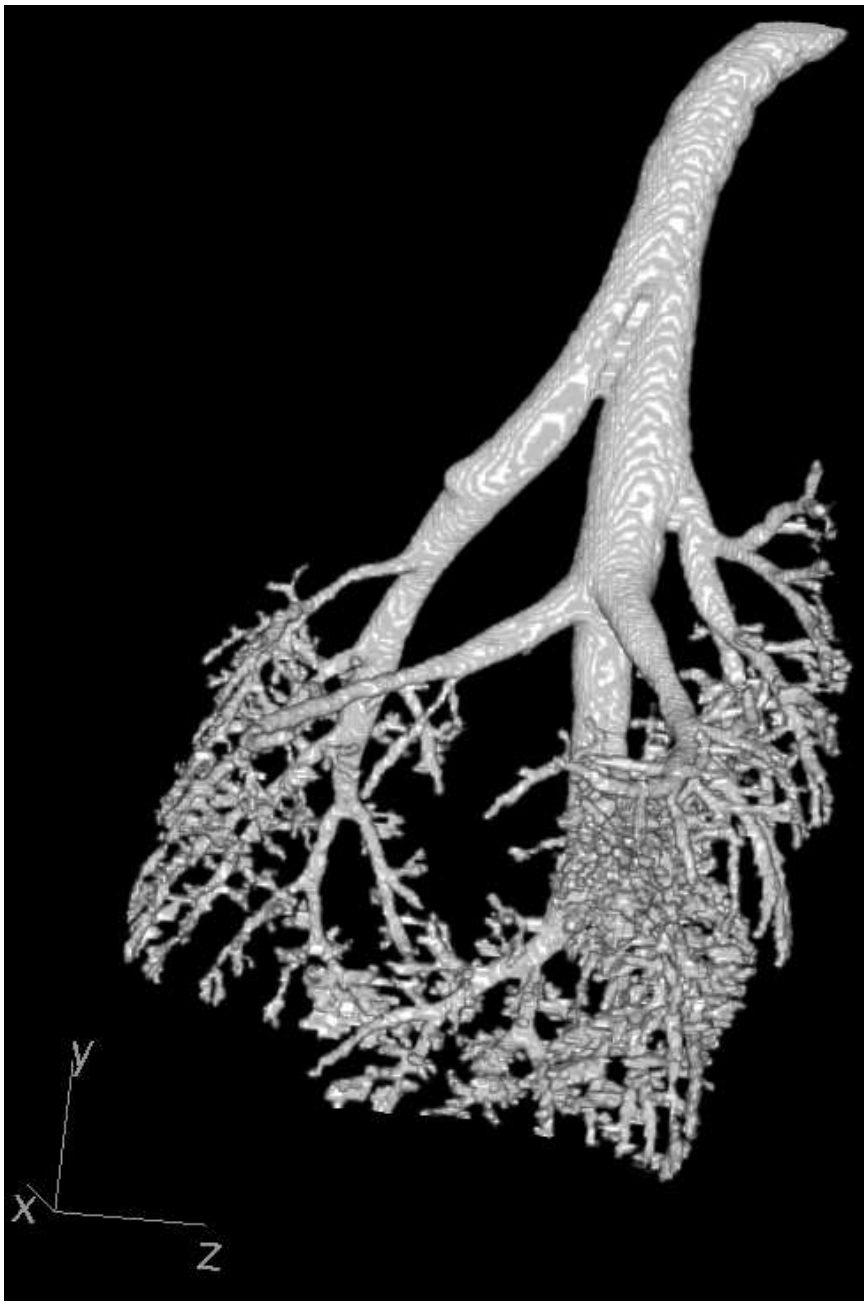

Figure 5.1: Model volume generated from x-ray tomography of mice airways to validate the reconstruction method.

Directions	X-	Y-	Z-
Mean	1.28	1.14	1.21
RMS	1.58	1.42	1.42
Max	15.11	19.79	8.9

Table 5.1: Symmetric distance in pixels (mean, root-mean-square and maximum) between the model surface and the *R3D2* reconstructions with x-, y- and z- directions of sectioning.

how far two compact non-empty subsets of a metric space are from each other. We used the software toolbox MESH (Aspert et al., 2002), to compute the minimum, maximum, mean and root-mean-square errors, between the surfaces and to visualize the differences between them. Table 5.1 we shows the mean symmetric distance Haussdorf between the model surface and the three surfaces generated by our method. As we can appreciate from the values, the system produces surfaces which are around 1 pixel away from the original model. If we take into account that our segmented contours are 1 pixel thick, we can conclude that *R3D2* recovers almost perfectly the model from any direction of sectioning. In Figure 5.2 we show an example of the case reconstruction with a color code on top of the *R3D2* surface representing the distance to the model. This way we can visualize the volumes matching. Blue areas represent perfect fit while green and yellow areas represent larger errors.

5.3.1.2 Missing Sections

Another problem of manual histological processing is the loss of sections that may happen during the cutting process. We wanted to test how robust our algorithm is against this problem that can lead to the loss or distortion of small structures of interest. To quantify the effect of missing sections we used the case sectioned in the z direction and generated 10 renderings. For the first rendering, all the sections are used. For the nth rendering, only one of every nth section are kept. Figure 5.3 shows the evolution of the symmetric error versus the percentage of sections used to generate the reconstruction. Using 100% of the sections we obtained 1.27 pixels of average error (mean symmetric Hausdorff distance), and this number gradually increased up to 3.11 pixels when we used only 10% of the sections. More representative of this degradation is the maximum distance error, which increases from 8.90

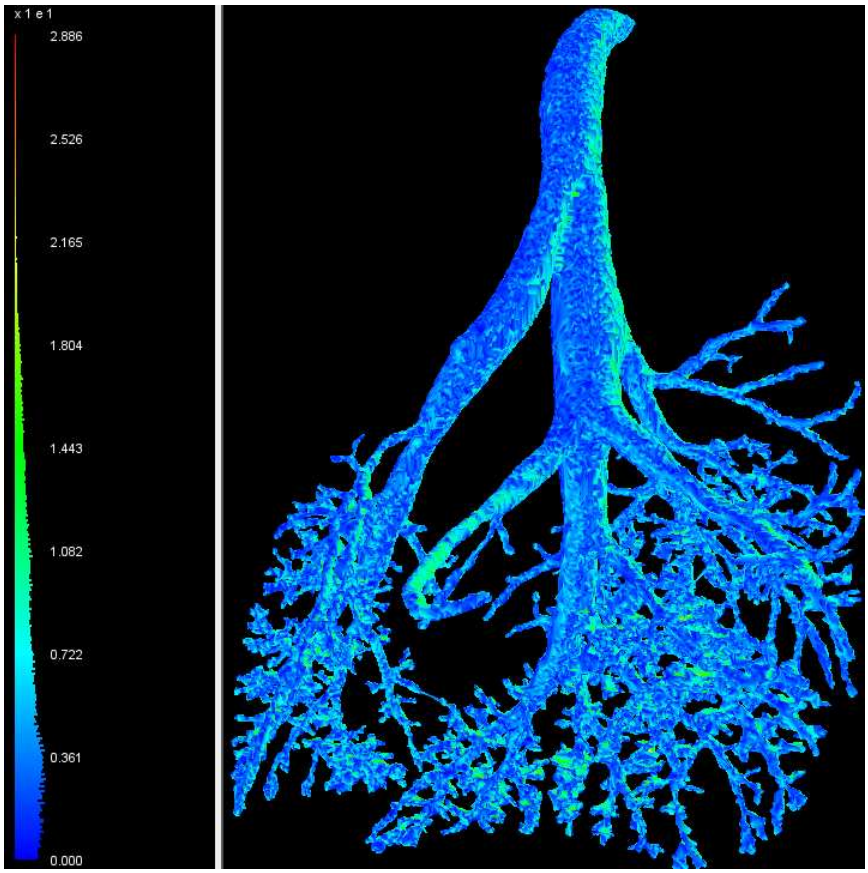

Figure 5.2: Visualization of Hausdorff distance. From left to right: histogram with color distance code scaled in microns (1 pixel = 6.8 microns) and *R3D2* reconstruction of the x- axis sectioned case colored with the distance to the model.

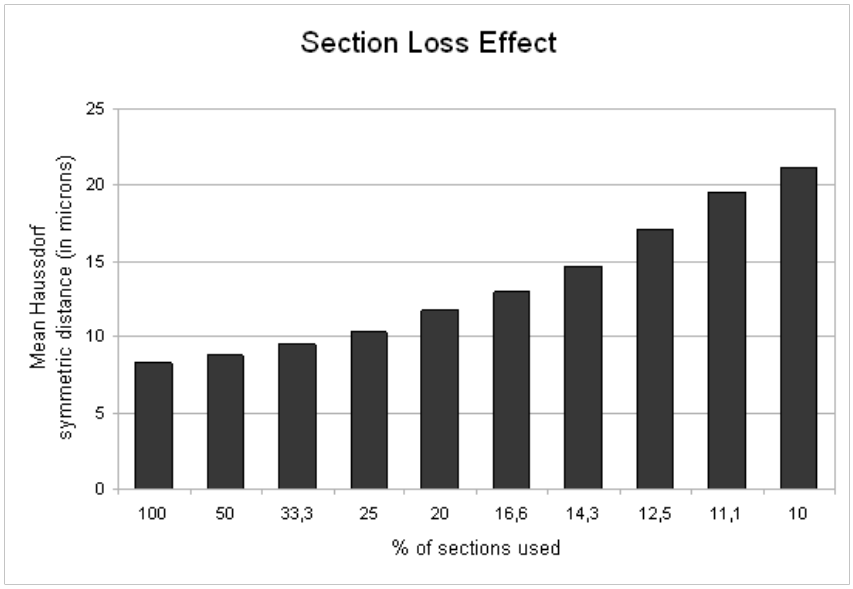

Figure 5.3: Distance error vs section loss.

when we used all the sections up to 40.92 in the 10% case. Figure 5.4 shows a zoom over the 3D renderings of the synthetic case (from using 100% of the sections down to using only 10%). We observe in the latter case that the main structure of the volume is maintained although the surface is gradually degraded. Indeed, we can visually infer from this experiment that using less than 25% of the sections prevents from extracting realistic measures based on the volume surface, since it loses too much detail with regard to the original model surface. However, we observe that the basic structure of the volume remains even when only a small percentage of the sections are used in the reconstruction.

5.3.1.3 Rigid and non-rigid deformations

The final validation step tested the robustness of our algorithm to correct for misalignment problems. To this end, we first applied random rigid deformations to all the sections of the model. Namely, we applied ± 20 pixels displacements and $\pm 15^{\circ}$ rotations to the sections, and then registered and reconstructed the model. We obtained a reconstructed volume similar to the original model but with different orientation. To be able to measure the surface distances, we then aligned the volumes using the basic Iterative Closest

Figure 5.4: Volume degradation. From top to bottom and from left to right, zoom over the 3D renderings of the synthetic case (from using 100% of the sections down to using only 10%). The different reconstructions are shown in red while the model is shown in translucent yellow.

Point Zhang (1993) method, which allowed us to match both reconstructions and calculate the Hausdorff distance between them. Even when the entire case was rigidly distorted, we obtained an acceptable mean symmetric distance of 3.48 pixels. This results confirms that our registration is robust against rigid distortions.

The final synthetic experiment combined rigid and non-rigid deformations. Thus, we applied the same type of random rigid transformations used in the previous experiment and added one elastic deformation (Arganda-Carreras et al., 2006) every 20 sections. To create the elastic deformations we used *SplineDeformationGenerator*[1]. The elastically deformed sections were corrected using our consistent elastic registration Arganda-Carreras et al. (2006) and then we proceeded to reconstruct the case. Again, we first matched the resulting volume and the model before calculating the symmetric distance between surfaces, which amounted to 3.57 pixels. This result proves the effectiveness of the registration method against non-linear distortions, since the distance is similar to the distance of the previous experiment.

5.3.2 Experiments with real data

Once the system was tested on synthetic data, we used it on real mammary gland tissue sections. An entire mouse mammary gland was fully sectioned and stained with H&E (even sections) and alternatively Estrogen Receptor (ER), Progesterone Receptor (PR) and Her2-neu (odd sections). Two hundred sections were produced with 5 microns thickness.

First, we used only the H&E sections. 6,106 structures of interest were segmented and 821 sub-groups were automatically detected and distributed under two big super-groups: the lymph node and the ductal network. Two views of the entire gland reconstruction are shown in Figure 5.5. The top image shows the result of the reconstruction before the rigid and local group registration process and the bottom image shows the same view after registration. The effect of the registration on the final meshes is really clear on this example, where the registered case shows much more compact and smoother volumes.

Next, in order to increase the volume quality, we segmented as well the structures of interest in the odd sections of the case and re-registered them refining the results with the local consistent elastic option. We then produced a more accurate volume and proceed to its analysis. First, we generated a binary image containing the ductal network and then calculated its skeleton

[1] *SplineDeformationGenerator* can be freely downloaded from `http://biocomp.cnb.csic.es/~iarganda/SplineDeformationGenerator/`

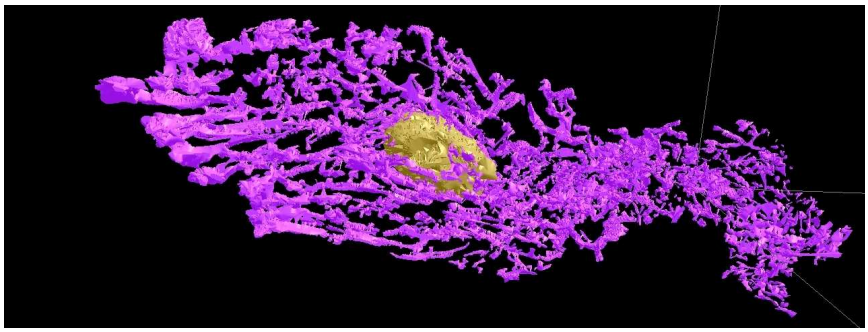

(a)

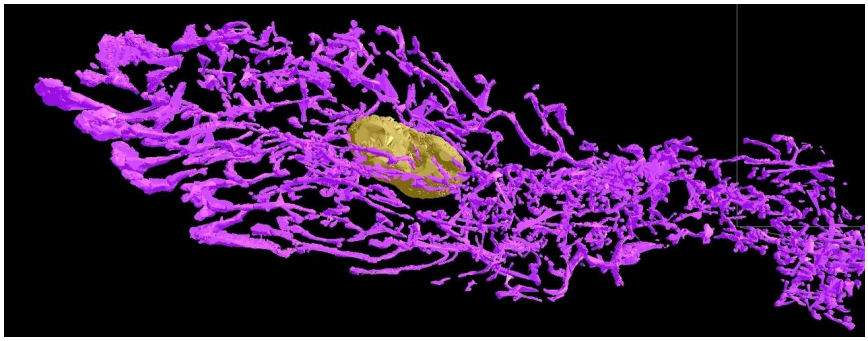

(b)

Figure 5.5: Two different 3D reconstructions of a whole mouse mammary gland: (5.5a) reconstruction before rigid and local group registration, (5.5b) reconstruction after the registration process.

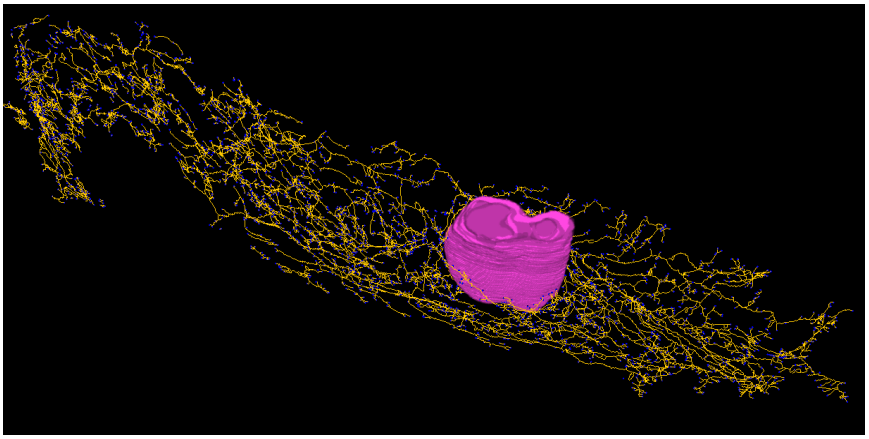

Figure 5.6: Mammary gland skeleton reconstruction view. The ductal network (yellow branches and blue terminal end points) is shown along with the lymph node volume (in fuchsia).

by applying a 3D thinning algorithm by Lee et al. (1994). This way, we obtained a more clear view of the ducts organization. In Figure 5.6 we show an example of the volume skeleton rendered with the lymph node volume to better appreciate the real distribution of the ductal network. Next, we analyzed the skeleton visiting its tree and measuring it. We found the ductal network consists of $6,209$ branches —regions between junctions and/or end points— averaging 191.99 microns, and $2,762$ junctions.

5.3.3 Study of cell distribution

As a direct application of the system, we can use the registered sections to study for instance the cell distribution in a duct. We can take 5 consecutive sections of the case and mark the membrane cells emphasized by their corresponding staining, project them into the same space using the registration results and have a look at their distribution. See Figure 5.7 for an example.

5.4 Conclusions

We have presented a method for the 3D reconstruction of mammary gland tissue blocks. The algorithm includes rigid and non-rigid image registration, automatic segmentation, contours grouping, and volume rendering. We validated the method using synthetic data, which allowed us to test it in chal-

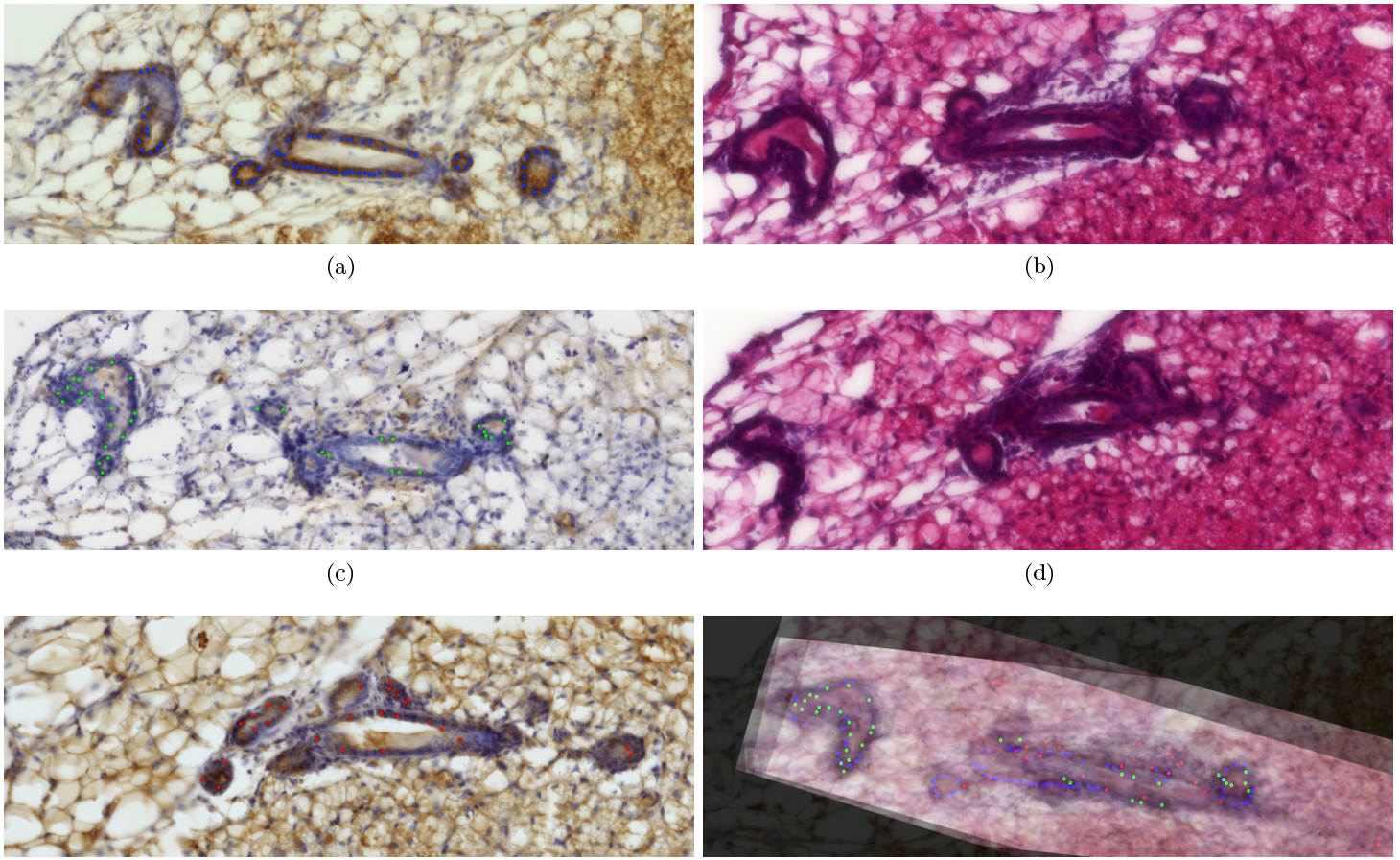

(a) (b) (c) (d) (e) (f)

Figure 5.7: Ductal cell distribution. From top to down: 40x zoom over 5 consecutive sections (staining order: (5.7a) ER —marked cells in blue—, (5.7b) H&E, (5.7c) PR —marked cells in green—, (5.7d) H&E, and (5.7e) Her2-neu —marked cells in red) and (5.7f) their registered projection emphasizing the cell distribution.

lenging situations such as different sectioning orientations, loss of sections and rigid and non-rigid misalignments. We finally applied the system to real data and showed renderings of entire mammary gland tissue blocks, the corresponding ductal network skeleton and its measures. We also showed the benefits of the system to study the membrane cell distribution at high resolution.

This algorithm completes the integrated and computer-based microscopy system *R3D2* for simultaneous morphological and molecular analysis of thick tissue samples. This system overcomes the penetration limitations of other microscopy modalities —confocal microscopy, two-photon excitation microscopy, etc.—, allows novel 3D views of the mammary gland morphology and is a complete and powerful tool to study any type of histological tissue.

Although *R3D2* is not open source software, many of the methods described and used in this work (elastic registration, 3D skeletonization...) have been developed as *ImageJ* plug-ins (Rasband, 1997-2009) and can be freely downloaded from `http://arantxa.ii.uam.es/~iarganda/software.html`.

Acknowledgments

The work presented here has been partially funded by the "UTE project CIMA" and the Department of Defense and University of California Breast Cancer Research Programs under contracts DAMD17-00-1-0227, DAMD17-00-1-0306 and 8WB-0150. Benjamin Schmid and Albert Cardona are especially acknowledged for providing continuous help and support on *ImageJ 3D Viewer*. Marta Rivera-Alba is gratefully acknowledged for her continuous biological and technical support.

Conclusions

"Reasoning draws a conclusion, but does not make the conclusion certain, unless the mind discovers it by the path of experience."

Roger Bacon

The most relevant steps to produce proper visualization of volumetric data are image registration, image segmentation and 3D triangulation of segmented data. In this thesis work we have included these steps in a complete and validated protocol to create realistic 3D reconstructions of serial sections data, mainly from histological sections but also from TEM sections. Moreover, we have studied in depth the field of medical image registration and we have presented novel methods to register any type of 2D images or image sequences. In this sense, the original contributions of this thesis are:

- The rigid and local registration methods (Chapter 2). The rigid method was published as *"Automatic Registration Of Serial Mammary Gland Sections"*, **I. Arganda-Carreras**, R. Fernandez-Gonzalez, C. Ortiz-de-Solorzano. The 26th International Conference of the IEEE Engineering in Medicine and Biology Society (EMBS), 1-5th September, 2004, San Francisco, California.

- The consistent elastic pairwise registration method (Chapter 3), published as *"Consistent and Elastic Registration of Histological Sections using Vector-Spline Regularization"*, **I. Arganda-Carreras,** C. O. S. Sorzano, R. Marabini, J. M. Carazo, C. Ortiz-de-Solorzano, and J. Kybic, Lecture Notes in Computer Science, Springer Berlin / Heidelberg, volume 4241/2006, CVAMIA: Computer Vision Approaches to Medical Image Analysis, pages 85-95, 2006.

- The application of consistent elastic registration to 2D gels (Appendix A), published as *"Elastic Image Registration of 2D gels for differential and repeatability studies"*, C.O.S. Sorzano, **I. Arganda-Carreras**, P. Thévenaz, A. Beloso, G. Morales, I. Valdés, C. Pérez-García, C. Castillo, E. Garrido, M. Unser. Proteomics. 2008 Jan; 8(1):62-5.

- The consistent elastic registration of 2D image sequences (Chapter 4), submitted as *"Non-rigid Consistent Registration of 2D Image Sequences"*. **I. Arganda-Carreras**, C.O.S. Sorzano, P. Thévenaz, A. Muñoz-Barrutia, J. Kybic, R. Marabini, J. M. Carazo, C. Ortiz-de-Solorzano. Medical Image Analysis (Submitted).

- The 3D reconstruction protocol, including the local group registration method and the automatic grouping algorithm (Chapter 5), published as *"3D Reconstruction of Histological Sections: Application to Mammary Gland Tissue"*. **I. Arganda-Carreras**, R. Fernandez-Gonzalez, A. Muñoz-Barrutia, C. Ortiz-de-Solorzano, Mic. Res. Tech. (Submitted).

On top of scientific publications, a further contribution of this thesis is the open source software *bUnwarpJ*, an *ImageJ* plugin for consistent and elastic image registration. Since its first release on July 20th 2006 and to this date, the *bUnwarpJ* website (`http://biocomp.cnb.csic.es/~iarganda/bUnwarpJ/`) has received more than 10,300 unique visits from all around the world, and the source code has been downloaded more than 1,200 times. The plugin details were published in:

- *"bUnwarpJ: Consistent and elastic registration in ImageJ. Methods and applications"*. **I. Arganda-Carreras**, C.O.S. Sorzano, C. Ortiz-de Solorzano, J. Kybic, In: ImageJ User & Developer Conference 2008.

Conclusiones

"El razonamiento extrae una conclusión, pero eso no hace la conclusión cierta, a menos que la mente la descubra por el camino de la experiencia."

Roger Bacon

Los pasos más importantes para producir una correcta visualización de datos volumétricos son el registro de imágenes, la segmentación de imágenes y la triangulación 3D de los contornos segmentados. En este trabajo de tesis hemos incluido estos pasos en un protocolo completo y validado para crear reconstrucciones 3D realísticas de secciones seriadas, principalmente de secciones histológicas pero también de secciones de microscopio electrónico de transmisión (TEM por sus siglas en inglés). Además hemos estudidado en profundidad el campo del registro de imagen médica y hemos presentado métodos nuevos para alinear todo tipo de imáges 2D o secuencias de imágenes 2D. En este sentido, las contribuciones originales de esta tesis son:

- Los métodos de registro rígido y local (Capítulo 2). El método de registro rígido fue publicado como *"Automatic Registration Of Serial Mammary Gland Sections"*, **I. Arganda-Carreras**, R. Fernandez-Gonzalez, C. Ortiz-de-Solorzano. The 26th International Conference of the IEEE Engineering in Medicine and Biology Society (EMBS), 1-5th September, 2004, San Francisco, California.

- El método de registro consistente y elástico de pares de imágenes (Capítulo 3), publicado como *"Consistent and Elastic Registration of Histological Sections using Vector-Spline Regularization"*, **I. Arganda-**

Carreras, C. O. S. Sorzano, R. Marabini, J. M. Carazo, C. Ortiz-de-Solorzano, and J. Kybic, Lecture Notes in Computer Science, Springer Berlin / Heidelberg, volume 4241/2006, CVAMIA: Computer Vision Approaches to Medical Image Analysis, pages 85-95, 2006.

- La aplicación del registro consistente y elástico a geles bidimensionales (Apéndice A), publicado como *"Elastic Image Registration of 2D gels for differential and repeatability studies"*, C.O.S. Sorzano, **I. Arganda-Carreras**, P. Thévenaz, A. Beloso, G. Morales, I. Valdés, C. Pérez-García, C. Castillo, E. Garrido, M. Unser. Proteomics. 2008 Jan; 8(1):62-5.

- El algoritmo de registro consistente y elástico de secuencias de imágenes 2D (Capítulo 4), enviado como *"Non-rigid Consistent Registration of 2D Image Sequences"*. **I. Arganda-Carreras**, C.O.S. Sorzano, P. Thévenaz, A. Muñoz-Barrutia, J. Kybic, R. Marabini, J. M. Carazo, C. Ortiz-de-Solorzano. Medical Image Analysis (Enviado).

- El protocolo de reconstrucción 3D, incluyendo el registro local por grupos y el algoritmo de agrupamiento automático (Capítulo 5), enviado como *"3D Reconstruction of Histological Sections: Application to Mammary Gland Tissue"*. **I. Arganda-Carreras**, R. Fernandez-Gonzalez, A. Muñoz-Barrutia, C. Ortiz-de-Solorzano. Mic. Res. Tech. (Enviado).

Por encima de las publicaciones científicas, una contribución indudable de esta tesis es el programa de código abierto *bUnwarpJ*, un plugin de *ImageJ* para registro elástico y consistente de imágenes. Desde su primera distribución el 20 de julio de 2006 y hasta la fecha, el lugar web de *bUnwarpJ* (`http://biocomp.cnb.csic.es/~iarganda/bUnwarpJ/`) ha recibido más de 10300 visitas únicas procedentes de todo el mundo, y su código fuente has sido descargado más de 1200 veces. Los detalles del plugin fueron publicados en la conferencia de *ImageJ* de 2008 como:

- *"bUnwarpJ: Consistent and elastic registration in ImageJ. Methods and applications"*. **I. Arganda-Carreras**, C.O.S. Sorzano, C. Ortiz-de Solorzano, J. Kybic, In: ImageJ User & Developer Conference 2008.

A

Application of pairwise registration: Elastic Registration of 2-D Gels for Differential and Repeatability Studies

This chapter is a technical brief where we describe and example of application that came as side effect of the registration method introduced in Chapter 3.

Abstract

One of the main applications of electrophoretic 2-D gels is the analysis of differential responses between different conditions. For this reason, specific spots are present in one of the images, but not in the other. In some other occasions, the same experiment is repeated between two and twelve times in order to increase statistical significance. In both situations, one of the major difficulties of these analysis is that 2-D gels are affected by spatial distortions due to run-time differences and dye-front deformations, resulting in images that are significantly dissimilar not only because of their content, but also because of their geometry. In this technical brief, we show how to use free, state-of-the-art image registration and fusion algorithms developed by us for solving the problem of comparing differential expression profiles, or computing an "average" image from a series of virtually identical gels.

A.1 Technical brief: consistent elastic registration of 2-D gels

2-D electrophoresis is a procedure to separate and identify the proteins expressed by an organ, tissue, or cell, at a given time and under certain conditions (Goerg et al., 2004). Proteins are first separated on the basis of their isoelectric point (pI) by isoelectric focusing (IEF) in an immobilized pH gradient (IPG) acrylamide strip. Then, proteins are separated in a perpendicular direction according to their mass by electrophoresis in a polyacrylamide gel in the presence of SDS (SDS-PAGE). Finally, a dye is applied with a selective affinity toward specific components of the proteins. The result is a bidimensional image in which small spots reveal the presence of those proteins that showed affinity to the dye and that had a specific mass and charge in the initial solution.

One of the problems of this technique is that, when comparing two different gels of similar biological content, there are important local spatial deformations that must be corrected if we want to identify biological differences or to compute an average gel from a series of biologically identical experiments. This geometrical correction is known in image processing as image registration.

Solving the registration problem can be done either by the help of landmarks (Raman et al., 2002) or the image content (Gustafsson et al., 2002; Rohr et al., 2004; Smilansky, 2001; Veeser et al., 2001; Sorzano et al., 2006). Sorzano et al. (2006) reported such preliminary results using an algorithm based on vector splines (Sorzano et al., 2005). This algorithm had a number of advantages over other image-based approaches such as versatility of the estimated deformation field, accurate image interpolation performed during the estimation of the deformation field, possibility of including both image information and landmarks at the same time, and possibility to impose smoothness to the deformation field through its divergence and rotational. Our registration algorithm is based on the use of cubic B-splines to represent the deformation field (this allows us to represent any continuous deformation field simply by reducing the spacing between splines). The algorithm minimizes in an efficient way (Levenberg-Marquardt minimization enhanced by a BFGS estimate of the local Hessian of the goal function) the quadratic error between a target image and a deformed source image. The deformation field can be constrained to be regular by penalizing its divergence and curl. Although the use of landmarks is not compulsory, in difficult cases (with very different image content) they can be very helpful to identify the correct

image deformation.

We extended the method (Arganda-Carreras et al., 2006) to compute "quasi-invertible" deformation fields so that image A can be mapped onto image B and vice versa. (The algorithm called *bUnwarpJ* can be freely downloaded from `http://biocomp.cnb.csic.es/~iarganda/bUnwarpJ`). This helps the optimizer to reduce the chance of getting trapped in a local minimum and opens the door to the simultaneous registration of any number of images.

In this technical brief, we show how to use *bUnwarpJ* to compare gels with different expressions and how to produce a single gel from a series of virtually identical gels. We show the applicability of our registration algorithm with 2-D gels used in the study of the Pseudomonas putida global Crc regulator. This protein is a global regulator of carbon metabolism in Pseudomonas. Morales et al. (2004) compared the proteome profile of a P. putida strain to that of an isogenic derivative in which the crc gene had been inactivated. Among others, the results showed that Crc is involved in the catabolic repression of hpd and hmgA genes from the homogentisate pathway, one of the central catabolic pathways for aromatic compounds. Based on four gels, a change in the expression of thirteen proteins of the metabolic pathway was identified (Morales et al., 2004). We registered the same gels and checked our results against those of Morales et al. (2004). We show in Figure A.1 the registration outcome as an RGB image, with one image assigned to the red channel and the other to the green channel. We used the same numbers as in the original paper to label the thirteen spots identified by Morales et al. (2004). As can be seen, all thirteen proteins can be properly and easily identified in our registration. Spots 5 and 6 are particularly interesting because they do not correspond to an inhibition process but to an overexpression. These two spots appear with an orange tint in Figure A.1, meaning that the registration algorithm correctly found the corresponding spots in the other image. We conclude that every protein with differential expression patterns that was identified by Morales et al. (2004) has been correctly picked out by our algorithm, too. We also picked out additional proteins that, according to our registration method, exhibit a differential expression pattern. Those, however, were not selected by Morales et al. (2004) because they were unrelated to the metabolic pathway under study.

We created 2-D gels from the cerebellum of rat brains to perform a repeatability study and to produce a single "average" gel. Proteins were first separated by IEF in a IPG strip (17 cm, pH: 3-10 non linear) and then by SDS-PAGE in 12% polyacrilamide gels ($180 \times 200 \times 1$ mm). Finally, the gels were stained with silver nitrate. We used the PROTEAN Plus Dodeca Cell

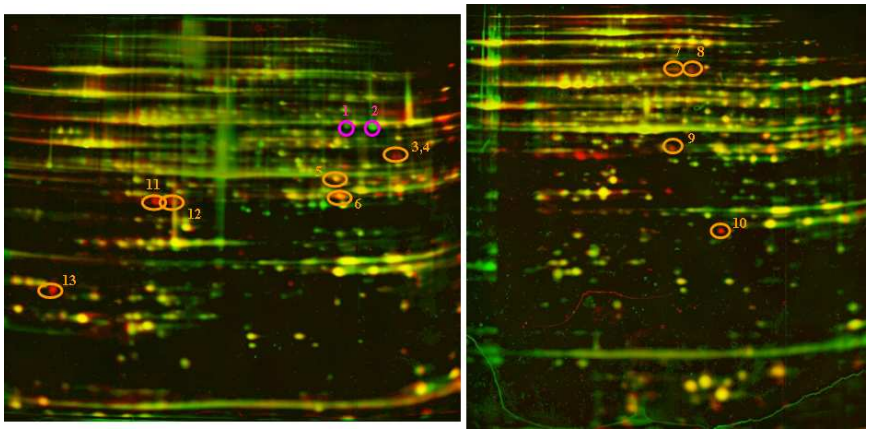

Figure A.1: Registration of two pairs of gels of P. putida. For each pair, one of the images was put in the red channel of an RGB color image and the other one was put in the green channel. Yellow spots correspond to proteins that are equally expressed in both gels. Red spots (3 and 4, 7–13) correspond to proteins that were expressed in the first gel but not in the second. Conversely, green spots (1 and 2) correspond to proteins expressed in the second gel but not in the first. Orange spots (5 and 6) correspond to overexpressed proteins.

(Bio-Rad) for the SDS-PAGE and the Dodeca Stainer (Bio-Rad) for the silver stain; those devices can run and stain 12 gels at a time, which ensures that gels are processed under the same conditions and improves reproducibility.

We used the software to mutually align all pairs of images. Then, we took one of them as reference and produced the corresponding warped images of the others. Instead of computing the pointwise arithmetic average, we followed an image fusion approach to retain as much information as possible from the original images (Forster et al., 2004). Image fusion combines the information from a set of images by keeping the most salient regions from each image under the hypothesis that information must show high local energy, which is met by a series of aligned 2-D gels. Saliency is measured in the wavelet domain: at each location the most salient wavelet coefficient is the one with highest module (wavelet coefficients are complex numbers). However, the most salient wavelet coefficient need not be selected, instead we use this concept in combination with two consistency checks: first, if two out of three corresponding subband coefficients are attributed to the same image, then the third one is taken from that image, too; second, if the majority of neighboring numbers in a 3×3 window in the final wavelet map are from a different image, then we take the "outlier" coefficient also from that image. Finally, an inverse wavelet transform is performed to reconstruct the image. The software for image fusion can be freely downloaded from `http://bigwww.epfl.ch/demo/edf`. We show in Figure A.2 the results of a simple average of the three images and the fused image after "quasi-invertbile" elastic registration. The fused image does not show multiple spots thanks to the elastic alignment and keeps the spots from the image where they are more salient thanks to the image-fusion algorithm. This produces a fused image in which the spots are as contrasted and resolved as possible (the median of the absolute difference between the fused image and the three images is 3.8%). As a drawback undesired lines (like the ones in the rectangle of Figure A.2a) are also kept in the fused image. These lines are distorted because they have to be mapped onto flat regions with no features, and the distorted lines fit equally in any orientation. If protein spots were available around, the regularity and continuity of the deformation field would prevent too much distortion (Sorzano et al., 2006).

The two experiments reported in this chapter show that free, open-source, publicly available, state-of-the-art image-processing algorithms for image registration and fusion can be used to compare gels with differential expression profiles and to build a single "average" gel from a series of virtually identical gels. This can be done in a low cost personal computer (PC or Mac) with a computational cost of less than 3 or 4 minutes.

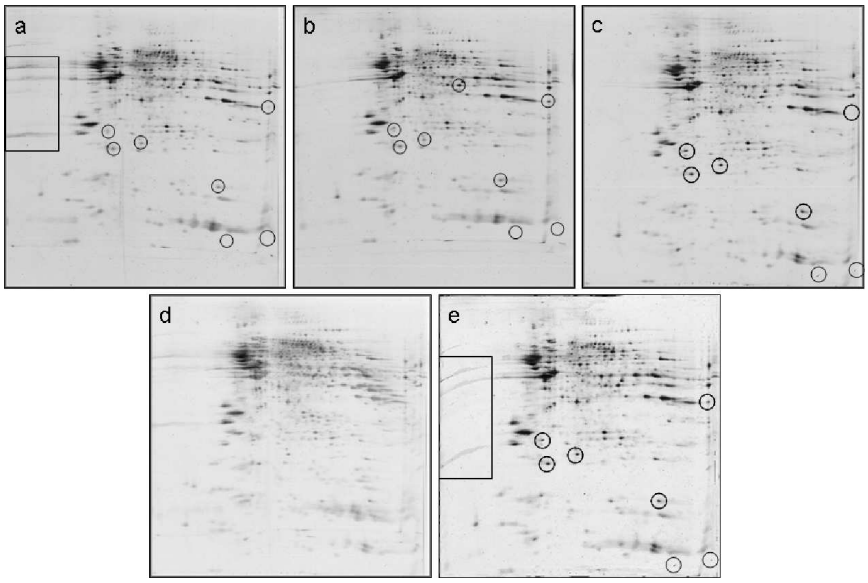

Figure A.2: (a–c) Three 2-D gels with identical biological content, taken under similar conditions; (d) arithmetic average before alignment; (e) image fusion after alignment by *bUnwarpJ*. Despite the physical handling of multiple gels at a time, which improves repeatability, we see in (d) that some spots still do not coincide. Image registration and fusion are required to obtain (e), where we observe a much better resolved average gel combining the information present in all three gels.

B

Appendix for Chapter 4

In this chapter we provide operators and derivative calculations to complete Chapter 4.

B.1 Operators and Explicit Derivatives

We calculate the derivatives of the similarity and consistency terms with respect to the deformation coefficients c in Appendix B.1.1 and B.1.2. Thanks to using B-splines to represent the images and the deformations, the derivatives can be calculated explicitly. Then we define the reduction and expansion operators needed to move through the resolution pyramids in Appendix B.1.3.

B.1.1 Data Term Derivatives

The derivative of the similarity term E_{S}^{ij} between images I_i and I_j with respect to the coefficients c of the deformation field $c_{a,k,l}^{r,s}$ can be easily inferred from the corresponding definitions of E_{S}^{ij} (see (4.3)) and $c_{a,k,l}^{r,s}$ (see (4.7)). Thus,

$$\frac{\partial E_{\mathrm{S}}^{ij}}{\partial c_{a,k,l}^{rs}} = -2 \sum_{\mathbf{x}\in\Omega_{ij}} \left[\left(I_j(\mathbf{x}) - I_i(g^{ij}(\mathbf{x})) \right) \frac{\partial I_i(g^{ij}(\mathbf{x}))}{\partial c_{a,k,l}^{rs}} \right], \tag{B.1}$$

where $a \in \{1,2\}$, $i,j,r,s \in \{1,2,3\}$ and $k,l \in \mathbb{Z}^2$.
The last term in the expression above equals

$$\begin{aligned}\frac{\partial I_i(g^{ij}(\mathbf{x}))}{\partial c^{rs}_{a,k,l}} &= \frac{\partial I_i(g^{ij}(\mathbf{x}))}{\partial g^{ij}(\mathbf{x})} \cdot \frac{\partial g^{ij}(\mathbf{x})}{\partial c^{rs}_{a,k,l}} \\ &= \frac{\partial I_i(g^{ij}(\mathbf{x}))}{\partial g^{ij}_1(\mathbf{x})} \frac{\partial g^{ij}_1(\mathbf{x})}{\partial c^{rs}_{a,k,l}} \\ &\quad + \frac{\partial I_i(g^{ij}(\mathbf{x}))}{\partial g^{ij}_2(\mathbf{x})} \frac{\partial g^{ij}_2(\mathbf{x})}{\partial c^{rs}_{a,k,l}}, \end{aligned} \tag{B.2}$$

where $\cdot$ denotes the scalar product. Finally, we need to evaluate $\frac{\partial g^{ij}_b(\mathbf{x})}{\partial c^{rs}_{a,k,l}}$.

If $i = r$ and $j = s$ ($ij = \{12, 21, 23, 32\}$), we can write

$$\begin{aligned}\frac{\partial g^{ij}_b(\mathbf{x})}{\partial c^{ij}_{a,k,l}} &= \frac{\partial g^{ij}_b(x, y)}{\partial c^{ij}_{a,k,l}} \\ &= \begin{cases} \beta^3\left(\frac{x}{s_x} - k\right)\beta^3\left(\frac{y}{s_y} - l\right) & \text{if } a = b \\ 0 & \text{if } a \neq b \end{cases} \end{aligned} \tag{B.3}$$

with $b \in \{1, 2\}$.

In other cases, that is, if $i \neq r$ and $j \neq s$ and $|i - j| = 2$ (i.e., $ij = \{13\}$ and $rs = \{12, 23\}$ or $ij = \{31\}$ and $rs = \{21, 32\}$), the expressions are slightly more complicated. For instance, for $ij = \{13\}$ and $rs = \{12\}$, we get

$$\begin{aligned}\frac{\partial g^{13}_b(\mathbf{x})}{\partial c^{12}_{a,k,l}} &= \frac{\partial g^{23}_b(g^{12}_b(x, y))}{\partial c^{12}_{a,k,l}} \\ &= \left.\frac{\partial g^{23}_b}{\partial x}\right|_{(x',y')} \left.\frac{\partial g^{12}_b}{\partial c^{12}_{a,k,l}}\right|_{(x,y)} \\ &\quad + \left.\frac{\partial g^{23}_b}{\partial y}\right|_{(x',y')} \left.\frac{\partial g^{12}_{|b-2|+1}}{\partial c^{rs}_{a,k,l}}\right|_{(x,y)}, \end{aligned} \tag{B.4}$$

where $(x', y') = g^{12}_b(x, y)$ and $\frac{\partial g^{12}_b(\mathbf{x})}{\partial c^{12}_{a,k,l}}$ is calculated as given in (B.3).

For $ij = \{13\}$ and $rs = \{23\}$, we can write

$$\frac{\partial g_b^{13}(\mathbf{x})}{\partial c_{a,k,l}^{23}} = \frac{\partial g_b^{23}(g_b^{12}(x,y))}{\partial c_{a,k,l}^{23}} = \left.\frac{\partial g_b^{23}}{\partial c_{a,k,l}^{23}}\right|_{(x',y')} + \left.\frac{\partial g_{|b-2|+1}^{23}}{\partial c_{a,k,l}^{23}}\right|_{(x',y')}, \tag{B.5}$$

where $(x',y') = g_b^{12}(x,y)$ and $\frac{\partial g_b^{23}(\mathbf{x}')}{\partial c_{a,k,l}^{23}}$ is calculated as in (B.3).

The corresponding derivatives for $ij = \{31\}$ and $rs = \{21, 32\}$, are obtained by symmetry from the ones already calculated.

B.1.2 Consistency Term Derivatives

The consistency energy functional E_{C}^{ij} needs to be evaluated only for the intermediate deformation fields, which simplifies the number of the derivatives to calculate. We have

$$\frac{\partial E_{\mathrm{C}}^{ij}}{\partial c_{a,k,l}^{rs}} = -2 \sum_{\mathbf{x}\in\Omega_{i,j}} \left(\mathbf{x} - g^{ji}(g^{ij}(\mathbf{x}))\right) \left(\frac{\partial g^{ji}(g^{ij}(\mathbf{x}))}{\partial c_{a,k,l}^{rs}}\right). \tag{B.6}$$

For $i = r$ and $j = s$, we can write for the last term

$$\begin{aligned}
\frac{\partial g^{ji}(g^{ij}(\mathbf{x}))}{\partial c_{a,k,l}^{ij}} &= \frac{\partial g^{ji}(g^{ij}(\mathbf{x}))}{\partial g^{ij}(\mathbf{x})} \cdot \frac{\partial g^{ij}(\mathbf{x})}{\partial c_{a,k,l}^{ij}} \\
&= \frac{\partial g^{ji}(g^{ij}(\mathbf{x}))}{\partial g_1^{ij}(\mathbf{x})} \frac{\partial g_1^{ij}(\mathbf{x})}{\partial c_{a,k,l}^{ij}} \\
&\quad + \frac{\partial g^{ji}(g^{ij}(\mathbf{x}))}{\partial g_2^{ij}(\mathbf{x})} \frac{\partial g_2^{ij}(\mathbf{x})}{\partial c_{a,k,l}^{ij}} \\
&= \left.\frac{\partial g^{ji}}{\partial x}\right|_{(x',y')} \left.\frac{\partial g_1^{ij}}{\partial c_{a,k,l}^{ij}}\right|_{(x,y)} \\
&\quad + \left.\frac{\partial g^{ji}}{\partial y}\right|_{(x',y')} \left.\frac{\partial g_2^{ij}}{\partial c_{a,k,l}^{ij}}\right|_{(x,y)},
\end{aligned} \tag{B.7}$$

where $(x',y') = g_1^{ij}(x,y)$ and $\frac{\partial g_b^{ij}}{\partial c_{a,k,l}^{ij}}$ is calculated from (B.3).

For $i = s$ and $j = r$, the evaluation is straight-forward also from (B.3).

$$\begin{aligned}\frac{\partial g^{ji}(g^{ij}(\mathbf{x}))}{\partial c^{ji}_{a,k,l}} &= \frac{\partial g^{ji}(\mathbf{x}')}{\partial c^{ji}_{a,k,l}} \\ &= \frac{\partial g^{ji}_1(\mathbf{x}')}{\partial c^{ji}_{a,k,l}} + \frac{\partial g^{ji}_2(\mathbf{x}')}{\partial c^{ji}_{a,k,l}},\end{aligned} \tag{B.8}$$

where $(x', y') = g^{ij}(x, y)$ and $\frac{\partial g^{ji}_b}{\partial c^{ji}_{a,k,l}}$ is calculated from (B.3).

B.1.3 Reduction and Expansion Operators

The expansion operator maps a coarser level of the pyramid onto a finer grid, and the reduction operator makes the complementary action. Following the idea of Unser et al. (1993), we define the expansion and reduction operators needed to implement the image and deformation pyramids. When the image dimensions are not a power 2 we divide by 2 and truncate to the closest integer. We can write the expansion operator as:

$$c_{-1}(k) = \left(u_2^3 * \uparrow_2 (c_0)\right)(k), \tag{B.9}$$

where c_0 are the initial coefficients, u_2^3 is the binomial filter defined by

$$u_2^3(k) = \begin{cases} 2^{-3}\begin{pmatrix} 4 \\ k+2 \end{pmatrix} & |k| \leq 2 \\ 0 & \text{other,} \end{cases}, \tag{B.10}$$

the $*$ operator represents a discrete convolution such that $(u * v)(k) = \sum_{l\in\mathbb{Z}} u(l)v(k-l)$ and the operator $\uparrow_2 (\cdot)$ upsamples its argument by two.

The reduction operator can be expressed as:

$$c_1(k) = \left(\frac{1}{2}\left(b^7\right)^{-1} * \downarrow_2 (u_2^3 * b^7 * c_0)\right)(k), \tag{B.11}$$

where $b^n(k) = \beta^n(x)|_{x=k}$ for $n = 3, 7$, and the operator $\downarrow_2 (\cdot)$ downsamples its argument by two. Since u_2^3 and b^7 are FIR filters, the main difficulty to evaluate (B.11) stems from the fact that $\left(b^7\right)^{-1}$ is an IIR filter.

As images are always finite, some data extrapolation is necessary to calculate the infinite sum involved in filtering with $\left(b^7\right)^{-1}$. We have chosen to extend the images using the widely extended mirror-on-bounds symmetric boundary conditions. If $f_0(k) \forall k \in [0 \dots N-1]$ is the 1D signal we want to

process and $f(k)$ is the mirrored signal with symmetric boundary conditions then

$$f(k) \underset{k\in\mathbb{Z}}{=} \begin{cases} f_0(-k) & k < 0 \\ f_0(k) & k \in [0 \dots N-1] \\ f_0(2N-2-k) & k > N-1 \end{cases}, \tag{B.12}$$

Let us next give the definition of the mirror-on-bounds anti-symmetric boundary conditions in 1D. Let $f(k)$ be the mirrored signal with anti-symmetric boundary conditions $\forall x \in \mathbb{R}$:

$$\begin{cases} f(x) - f(0) &= f(0) - f(-x) \\ f(x+N-1) - f(N-1) &= f(N-1) \\ & \quad -f(N-1-x) \end{cases}. \tag{B.13}$$

The direct B-spline filter $\left(b^7\right)^{-1}$ is an all-pole system that can be implemented efficiently using a cascade of first-order causal and anti-causal recursive filters (Unser et al., 1993). Next, we describe the explicit procedure for the calculation using the same reasoning as described by Unser (1999).

By sampling the seventh degree B-spline at integers values we find that

$$\begin{aligned} b^7(z) = \quad & \left(z^3 + 120z^2 + 1191z + 2416\right. \\ & \left. +1191z^{-1} + 120z^{-2} + z^{-3}\right) \quad \left(\frac{1}{5040}\right). \end{aligned} \tag{B.14}$$

Thus, the filter to implement is

$$(b^7)^{-1}(k) \leftrightarrow \frac{1}{b^7(z)} = 5040 \prod_{i=1}^{3} \left(\frac{1}{z_i z^{-1}}\right)\left(\frac{-z_i}{1-z_i z}\right), \tag{B.15}$$

with $z_1 = -0.53528$, $z_2 = -0.122558$ and $z_3 = -0.00914869$. This three-pole filter can be implemented as three sequential one-pole filters. Given the input signal values $\{f(k)\}_{k=0,\dots,N-1}$ and defining $c^-(k) = \frac{c(k)}{5040}$. The right hand side factorization leads to the following recursive algorithm

$$c^+(k) = f(k) + z_i c^+(k-1),\ (k = 1, \dots, N-1), \tag{B.16}$$

$$c^-(k) = z_i(c^-(k+1) - c^+(k)),\ (k = N-2, \dots, 0), \tag{B.17}$$

where z_i is the corresponding pole. Notice that the first filter is casual, running from left to right and the second filter is anticausal running from right to left. Therefore, we need to specify the appropriate starting values for both recursions, i.e., $c^+(0)$ and $c^-(N-1)$. To ensure that the procedure is reversible, we impose the requirement that $f(k)$ can be recovered exactly by convolving $c(k)$ with b^7 using the same type of boundary conditions. The starting values to be used for symmetric mirror boundary conditions are given by Unser (1999). We have calculated the corresponding values for anti-symmetric mirror boundary conditions using the same reasoning. The initial value for the first recursion is given by

$$\begin{aligned} c^+(0) &= \left(\frac{1}{1-z_i^{2N-2}}\right)\left(\frac{1+z_i}{1-z_i}\right) \\ &\quad \Big(f(0) - z_i^{N-1} f(N-1)\Big) + \\ &\quad + \sum_{n\in[1\ldots N-2]} \left(z_i^{(2N-2-n)} - z_i^n\right) f(n) \end{aligned} \tag{B.18}$$

Note that here $f(k)$ indicates the results of the previous recursions and not the original samples as it was above in (B.12) and (B.13). Correspondingly, the initialization for the second recursion is

$$\begin{aligned} c^-(N-1) &= \left(\frac{-z_i}{(1-z_i)^2}\right) \\ &\quad \left(c^+(N-1) - z_i c^+(N-2)\right). \end{aligned} \tag{B.19}$$

Bibliography

Andronache, A., Cattin, P., Szekely, G., 2006. Local intensity mapping for hierarchical non-rigid registration of multi-modal images using the cross-correlation coefficient. In: Pluim, JPW and Likar, B and Gerritsen, FA (Ed.), Biomedical Image Registration, Proceedings. Vol. 4057 of Lecture Notes in Computer Science. Springer-Verlag Berlin, pp. 26–33, 3rd International Workshop on Biomedical Image Registration, Utrecht, Netherlands, July 09-11, 2006.

Arganda-Carreras, I., Fernandez-Gonzalez, R., Ortiz-de Solorzano, C., 1-5 Sept. 2004. Automatic registration of serial mammary gland sections. Engineering in Medicine and Biology Society, 2004. IEMBS '04. 26th Annual International Conference of the IEEE 1, 1691–1694 Vol.3.

Arganda-Carreras, I., Sorzano, C. O. S., Marabini, R., Carazo, J.-M., Ortiz-de Solorzano, C., Kybic, J., May 2006. Consistent and elastic registration of histological sections using vector-spline regularization. In: Computer Vision Approaches to Medical Image Analysis. Vol. 4241 of Lecture Notes in Computer Science. Springer Berlin/Heidelberg, pp. 85–95.

Arganda-Carreras, I., Sorzano, C. O. S., Ortiz-de Solorzano, C., Kybic, J., 2008. bUnwarpJ: Consistent and elastic registration in ImageJ. Methods and applications. In: ImageJ User & Developer Conference.

Aspert, N., Santa-Cruz, D., Ebrahimi, T., 2002. MESH: Measuring errors between surfaces using the Hausdorff distance. In: Proceedings of the

IEEE International Conference on Multimedia and Expo. Vol. I. pp. 705 – 708, http://mesh.epfl.ch.

Auer, M., Regitnig, P., Holzapfel, G. A., April 2005. An automatic nonrigid registration for stained histological sections. IEEE Transactions on Image Processing 14 (4), 475–486.

Avants, B. B., Schoenemann, P. T., Gee, J. C., June 2006. Lagrangian frame diffeomorphic image registration: Morphometric comparison of human and chimpanzee cortex. Medical Image Analysis 10, 397–412.

Bagheri-Yarmand, R., Vadlamudi, R. K., Kumar, R., May 2003. Activating transcription factor 4 overexpression inhibits proliferation and differentiation of mammary epithelium resulting in impaired lactation and accelerated involution. J Biol Chem 278 (19), 17421–17429.
URL http://dx.doi.org/10.1074/jbc.M300761200

Bhatia, K. K., Hajnal, J. V., Puri, B. K., Edwards, A. D., Rueckert, D., 2004. Consistent groupwise non-rigid registration for atlas construction. In: IEEE International Symposium on Biomedical Imaging. IEEE, pp. 908–911.

Boissonnat, J.-D., Geiger, B., February 1993. 3-Dimensional Reconstruction of Complex Shapes based on the Delaunay Triangulation. In: Acharya, RS and Goldgof, DB (Ed.), Biomedical Image Processing and Biomedical Visualization. Vol. 1905 of Procedings of the Society of Photo-optical Instrumentation Engineers (SPIE). SPIE - Int Soc Optical Engineering, pp. 964–975.

Bookstein, F. L., 1989. Principal warps: Thin-plate splines and the decomposition of deformations. IEEE Transactions on Pattern Analysis and Machine Intelligence 11 (6), 567–585.

Borgefors, G., 1988. Hierarchical chamfer matching: A parametric edge matching algorithm. IEEE Transactions on Pattern Analysis and Machine Intelligence 10 (6), 849–865.

Bossert, O., April 2005. A robust method for alignment of histological images. Computer Methods and Programs in Biomedicine 78 (1), 35–38.
URL http://dx.doi.org/10.1016/j.cmpb.2004.12.002

Brey, E. M., King, T. W., Johnston, C., McIntire, L. V., Reece, G. P., Patrick, C. W., May 2002. A technique for quantitative three-dimensional

analysis of microvascular structure. Microvascular Research 63 (3), 279–294.
URL http://dx.doi.org/10.1006/mvre.2002.2395

Brown, M., Szeliski, R., Winder, S., 20–25 June 2005. Multi-image matching using multi-scale oriented patches. In: Proc. IEEE Computer Society Conference on Computer Vision and Pattern Recognition CVPR 2005. Vol. 1. pp. 510–517.

Capek, M., Bruza, P., Janácek, J., Karen, P., Kubínová, L., Vagnerová, R., February 2009. Volume reconstruction of large tissue specimens from serial physical sections using confocal microscopy and correction of cutting deformations by elastic registration. Microscopy Research and Technique 72 (2), 110–119.
URL http://dx.doi.org/10.1002/jemt.20652

Capuco, A. V., Ellis, S., Wood, D. L., Akers, R. M., Garrett, W., June 2002. Postnatal mammary ductal growth: three-dimensional imaging of cell proliferation, effects of estrogen treatment, and expression of steroid receptors in prepubertal calves. Tissue Cell 34 (3), 143–154.

Chang, S.-H., Liu, C. H., Conway, R., Han, D. K., Nithipatikom, K., Trifan, O. C., Lane, T. F., Hla, T., January 2004. Role of prostaglandin E2-dependent angiogenic switch in cyclooxygenase 2-induced breast cancer progression. Proceedings of the National Academy of Sciences of the United States of America 101 (2), 591–596.
URL http://dx.doi.org/10.1073/pnas.2535911100

Christensen, G. E., He, J., 2001. Consistent nonlinear elastic image registration. In: Mathematical Methods in Biomedical Image Analysis. IEEE, pp. 37–43.

Christensen, G. E., Johnson, H. J., 2001. Consistent image registration. IEEE Transactions in Medical Imaging 20 (7), 568–582.

Cleary, M. P., Juneja, S. C., Phillips, F. C., Hu, X., Grande, J. P., Maihle, N. J., Feb 2004. Leptin receptor-deficient mmtv-tgf-alpha/lepr(db)lepr(db) female mice do not develop oncogene-induced mammary tumors. Exp Biol Med (Maywood) 229 (2), 182–193.

Cootes, T., Marsland, S., Twining, C., Smith, K., Taylor, C., 2004. Groupwise diffeomorphic non-rigid registration for automatic model building. In: Pajdla, T and Matas, J (Ed.), Computer Vision - ECCV 2004, PT 4. Vol.

2034 of Lecture Notes in Computer Science. Business Informat Grp as; Camea spol sro; Casablanca INT sro; ECVision; Microsoft Res; Miracle Network sro; Neovision sro; Toyota, Springer-Verlag Berlin, Heidelberg Platz 3, D-14197 Berling, Germany, pp. 316–327, 8th European Conference on Computer Vision, Prague, Czech Republic, May 11-14, 2004.

Csapo, I., Holland, C. M., Guttmann, C. R., 2007. Image registration framework for large-scale longitudinal MRI data sets: Strategy and validation. Magnetic Resonance Imaging 25 (6), 889–893.

Dawant, B. M., 2002. Non-rigid registration of medical images: purpose and methods, a short survey. In: IEEE International Symposium on Biomedical Imaging. IEEE, pp. 465–468.

Dean, P., Mascio, L., Ow, D., Sudar, D., Mullikin, J., 1990. Proposed standard for image cytometry data files. Cytometry 11 (5), 561–569.

Deverell, M. H., Bailey, N., Whimster, W. F., November 1989. Tissue distortion in three-dimensional reconstruction of wax or plastic embedded microscopic structures. Pathology Research and Practice 185 (5), 598–601.

Eriksson, A. P., Astrom, K., 2006. Bijective image registration using thin-plate splines. In: ICPR '06: Proceedings of the 18th International Conference on Pattern Recognition. IEEE Computer Society, Washington, DC, USA, pp. 798–801.

Fernandez-Gonzalez, R., 2006. Quantitative in situ characterization of a putative stem cell population in the mouse mammary gland. Ph.D. thesis, Joint Graduate Program in Bioengineering. University of California, San Francisco and University of California, Berkeley.

Fernandez-Gonzalez, R., Deschamps, T., Idica, A., Malladi, R., Ortiz-de-Solorzano, C., 2004. Automatic segmentation of histological structures in mammary gland tissue sections. Journal of Biomedical Optics 9 (3), 444–453.
URL `http://link.aip.org/link/?JBO/9/444/1`

Fernandez-Gonzalez, R., Jones, A., Garcia-Rodriguez, E., Chen, P. Y., Idica, A., Locket, S. J., Barcellos-Hoff, M. H., Ortiz-de-Solorzano, C., 2002. A system for combined three-dimensional morphological and molecular analysis of thick tissue specimens. Microscopy Research and Technique 59 (6), 522–530.

Fiala, J. C., April 2005. Reconstruct: a free editor for serial section microscopy. Journal of Microscopy 218 (Pt 1), 52–61.
URL http://dx.doi.org/10.1111/j.1365-2818.2005.01466.x

Forster, B., Ville, D. V. D., Berent, J., Sage, D., Unser, M., September 2004. Complex wavelets for extended depth-of-field: a new method for the fusion of multichannel microscopy images. Microscopy Research and Technique 65 (1-2), 33–42.
URL http://dx.doi.org/10.1002/jemt.20092

Geng, X., Kumar, D., Christensen, G. E., 2005. Transitive inverse-consistent manifold registration. In: Christensen, G. E., Sonka, M. (Eds.), Information Processing in Medical Imaging. Vol. 3565 of Lecture Notes in Computer Science. Springer, pp. 468–479.

Giovanni, C. D., Nicoletti, G., Landuzzi, L., Astolfi, A., Croci, S., Comes, A., Ferrini, S., Meazza, R., Iezzi, M., Carlo, E. D., Musiani, P., Cavallo, F., Nanni, P., Lollini, P.-L., Jun 2004. Immunoprevention of her-2/neu transgenic mammary carcinoma through an interleukin 12-engineered allogeneic cell vaccine. Cancer Res 64 (11), 4001–4009.
URL http://dx.doi.org/10.1158/0008-5472.CAN-03-2984

Glasbey, C., Mardia, K., April 1998. A review of image-warping methods. Journal of Applied Statistics 25 (2), 155–171.

Goerg, A., Weiss, W., Dunn, M. J., December 2004. Current two-dimensional electrophoresis technology for proteomics. Proteomics 4 (12), 3665–3685.
URL http://dx.doi.org/10.1002/pmic.200401031

Grenander, U., Miller, M., December 1998. Computational anatomy: An emerging discipline. Quarterly of Applied Mathematics 56 (4), 617–694, International Symposium on Current and Future Challenges in Aoolied Mathematics, to Mark the 50th Anniversary of the Division-of-Applied-Mathematics, Providence, Rhode Island, 1998.

Gustafsson, J. S., Blomberg, A., Rudemo, M., June 2002. Warping two-dimensional electrophoresis gel images to correct for geometric distortions of the spot pattern. Electrophoresis 23 (11), 1731–1744.
URL http://dx.doi.org/3.0.CO;2-

Haas, A., Fischer, M. S., 1997. Three-dimensional reconstruction of histological sections using modern product-design software. The Anatomical Record 249 (4), 510–516.

URL http://dx.doi.org/10.1002/(SICI)1097-0185(199712)249:4<510::AID-AR11>3.0.CO;2-R

Hadsell, D. L., Bonnette, S., George, J., Torres, D., Klimentidis, Y., Klementidis, Y., Gao, S., Haney, P. M., Summy-Long, J., Soloff, M. S., Parlow, A. F., Sirito, M., Sawadogo, M., November 2003. Diminished milk synthesis in upstream stimulatory factor 2 null mice is associated with decreased circulating oxytocin and decreased mammary gland expression of eukaryotic initiation factors 4E and 4G. Molecular Endocrinology 17 (11), 2251–2267.
URL http://dx.doi.org/10.1210/me.2002-0031

Hajnal, J. V., Hawkes, D. J., Hill, D. L. G., 2001. Medical Image Registration. CRC Press.

Hayward, S. W., Brody, J. R., Cunha, G. R., July 1996. An edgewise look at basal epithelial cells: three-dimensional views of the rat prostate, mammary gland and salivary gland. Differentiation 60 (4), 219–227.

Hilakivi-Clarke, L., Clarke, R., Onojafe, I., Raygada, M., Cho, E., Lippman, M., August 1997. A maternal diet high in n - 6 polyunsaturated fats alters mammary gland development, puberty onset, and breast cancer risk among female rat offspring. Proceedings of the National Academy of Sciences of the United States of America 94 (17), 9372–9377.

Hofstadler-Deiques, C., Walter, M., Mierlo, F., Ruduit, R., 2005. Software system for three-dimensional volumetric reconstruction of histological sections: A case study for the snake chondrocranium. The Anatomical Record Part A: Discoveries in Molecular, Cellular, and Evolutionary Biology 286A (2), 938–944.
URL http://dx.doi.org/10.1002/ar.a.20227

Huang, J., Abendschein, D., Dávila-Román, V. G., Amini, A. A., 1999. Spatio-temporal tracking of myocardial deformation with a 4 D B-spline model from tagged MRI. IEEE Transactions on Medical Imaging 18 (10), 957–972.

Hult, R., 1995. 3D reconstruction of insect ganglia. Ph.D. thesis, Centre for Image Analysis, Uppsala.

Ip, C., Banni, S., Angioni, E., Carta, G., McGinley, J., Thompson, H. J., Barbano, D., Bauman, D., 1999. Conjugated linoleic acid-enriched butter

fat alters mammary gland morphogenesis and reduces cancer risk in rats. Journal of Nutrition 129, 2135–2142.

Johnson, H. J., Christensen, G. E., May 2002. Consistent landmark and intensity-based image registration. IEEE Transactions on Medical Imaging 21 (5), 450–461.
URL http://dx.doi.org/10.1109/TMI.2002.1009381

Kuglin, C. D., Hines, D. C., September 1975. The phase correlation image alignment method. In: Proc. IEEE 1975 Conference on Cybernetics and Society. pp. 163–165.

Kybic, J., Unser, M., 2003. Fast parametric elastic image registration. IEEE Transactions on Image Processing 12 (11), 1427–1442.

Ledesma-Carbayo, M. J., Kybic, J., Desco, M., Santos, A., Sühling, M., Hunziker, P. R., Unser, M., 2005. Spatio-temporal nonrigid registration for ultrasound cardiac motion estimation. IEEE Transactions on Medical Imaging 24 (9), 1113–1126.

Lee, T.-C., Kashyap, R. L., Chu, C.-N., 1994. Building skeleton models via 3-D medial surface/axis thinning algorithms. CVGIP: Graphical Models and Image Processing 56 (6), 462–478.

Lester, H., Arridge, S. R., 1999. A survey of hierarchical non-linear medical image registration. Pattern Recognition 32 (1), 129–149.

Liu, S., Weaver, D. L., Taatjes, D. J., April 1997. Three-dimensional reconstruction by confocal laser scanning microscopy in routine pathologic specimens of benign and malignant lesions of the human breast. Histochemistry and Cell Biology 107 (4), 267–278.

Loeckx, D., Maes, F., Vandermeulen, D., Suetens, P., 2004. Nonrigid image registration using free-form deformations with a local rigidity constraint. In: Barillot, C., Haynor, D. R., Hellier, P. (Eds.), Medical Image Computing and Computer-Assisted Intervention - MICCAI 2004. Vol. 3216 of Lecture Notes in Computer Science. Springer, pp. 639–646.

Lowe, D. G., 2004. Distinctive image features from scale-invariant keypoints. International Journal of Computer Vision 60 (2), 91–110.

Ma, L., Chen, Y., Moore, K. L., 2003. Flexible camera calibration using a new analytical radial undistortion formula with application to mobile

robot localization. 2003 IEEE International Symposium on Inteligence Control cs.CV/0307045, 799–804.

MacKenzie-Graham, A., Lee, E.-F., Dinov, I. D., Bota, M., Shattuck, D. W., Ruffins, S., Yuan, H., Konstantinidis, F., Pitiot, A., Ding, Y., Hu, G., Jacobs, R. E., Toga, A. W., February 2004. A multimodal, multidimensional atlas of the C57BL/6J mouse brain. Journal of Anatomy 204 (2), 93–102.
URL http://dx.doi.org/10.1111/j.1469-7580.2004.00264.x

Maes, F., Collignon, A., Vandermeulen, D., Marchal, G., Suetens, P., April 1997. Multimodality image registration by maximization of mutual information. IEEE Transactions on Medical Imaging 16 (2), 187–198.
URL http://dx.doi.org/10.1109/42.563664

Maintz, J., Viergever, M., 1998. A survey of medical image registration. Medical Image Analysis 2 (1), 1–36.

Malandain, G., Bardinet, E., Nelissen, K., Vanduffel, W., September 2004. Fusion of autoradiographs with an mr volume using 2-D and 3-D linear transformations. Neuroimage 23 (1), 111–127.
URL http://dx.doi.org/10.1016/j.neuroimage.2004.04.038

Marquardt, D. W., 1963. An Algorithm for Least-Squares Estimation of Nonlinear Parameters. Journal of the Society for Industrial and Applied Mathematics 11 (2), 431–441.

Marsland, S., Twining, C., Taylor, C., 2003. Groupwise non-rigid registration using polyharmonic clamped-plate splines. In: Medical Image Computing and Computer-Aided Intervention (MICCAI'03). No. 2879 in Lecture Notes in Computer Science. Springer-Verlag, pp. 771–779.
URL http://www-ist.massey.ac.nz/smarsland/PUBS/MICCAI03.pdf

Matula, P., Kozubek, M., Matula, P., 2004. Applications of image registration in human genome research. In: Sonka, M and Kakadiaris, IA and Kybic, J (Ed.), Computer Vision and Mathematical Methdos in Medical and Biomedical Image Analysis. Vol. 3117 of Lecture Notes in Computer Science. Springer-Verlag Berlin, Heidelberg Platz 3, D-14197 Berling, Germany, pp. 376–384.

Maurer, Jr., C., Aboutanos, G., Dawant, B., Maciunas, R., Fitzpatrick, J., December 1996. Registration of 3-D images using weighted geometrical features. IEEE Transactions on Medical Imaging 15 (6), 836–849.

Morales, G., Linares, J., Beloso, A., Albar, J., Martinez, J., Rojo, F., March 2004. The Pseudomonas putida Crc global regulator controls the expression of genes from several chromosomal catabolic pathways for aromatic compounds. Journal of Bacteriology 186 (5), 1337–1344.

Ohtake, T., Kimijima, I., Fukushima, T., Yasuda, M., Sekikawa, K., Takenoshita, S., Abe, R., June 2001. Computer-assisted complete three-dimensional reconstruction of the mammary ductal/lobular systems: implications of ductal anastomoses for breast-conserving surgery. Cancer 91 (12), 2263–2272.

Osher, S., Paragios, N., 2003. Geometric Level Set Methods in Imaging,Vision,and Graphics. Springer-Verlag New York, Inc., Secaucus, NJ, USA.

Osher, S., Sethian, J. A., 1988. Fronts propagating with curvature-dependent speed: Algorithms based on Hamilton-Jacobi formulations. Journal of Computational Physics 79, 12–49.
URL citeseer.ist.psu.edu/osher88fronts.html

Osher, S. J., Fedkiw, R. P., October 2002. Level Set Methods and Dynamic Implicit Surfaces. Springer.
URL http://www.amazon.ca/exec/obidos/redirect?tag=citeulike09-20\&path=ASIN/0387954821

Otsu, N., January 1979. A threshold selection method from gray-level histograms. IEEE Transactions on Systems, Man and Cybernetics 9 (1), 62–66.

Ourselin, S., Roche, A., Subsol, G., Pennec, X., Ayache, N., January 2001. Reconstructing a 3D structure from serial histological sections. Image and Vision Computing 19 (1-2, Sp. Iss. SI), 25–31, International Workshop on Biomedical Image Registration, Bled, Slovenia, August, 1999.

Pitiot, A., Bardinet, E., Thompson, P. M., Malandain, G., June 2006. Piecewise affine registration of biological images for volume reconstruction. Medical Image Analysis 10 (3), 465–483.
URL http://dx.doi.org/10.1016/j.media.2005.03.008

Pitiot, A., Malandain, G., Bardinet, E., Thompson, P., 2003. Piecewise affine registration of biological images. In: Gee, JC and Maintz, JBA and Vannier, MW (Ed.), Biomedical Image Registration. Vol. 2717 of Lecture Notes in Computer Science. Springer-Verlag Berlin, pp. 91–101, 2nd

International Workshop on Biomedical Image Registration, Philadelphia, Pennsylvania, June 23-24, 2003.

Pluim, J. P. W., Likar, B., Gerritsen, F. A. (Eds.), 2006. Biomedical Image Registration, Third International Workshop, WBIR 2006, Utrecht, The Netherlands, July 9-11, 2006, Proceedings. Vol. 4057 of Lecture Notes in Computer Science. Springer.

Pluim, J. P. W., Maintz, J. B. A., Viergever, M. A., 2003. Mutual information based registration of medical images: A survey. IEEE Transactions on Medical Imaging 22 (8), 986–1004.

Press, W. H., Teukolsky, S. A., Vetterling, W. T., Flannery, B. P., 1992. Numerical Recipes in C, 2nd Edition. Cambridge University Press.

Radeva, P., Amini, A. A., Huang, J., 1997. Deformable B-Solids and implicit snakes for 3D localization and Tracking of SPAMM MRI data. Computer Vision and Image Understanding 66 (2), 163–178.

Raman, B., Cheung, A., Marten, M. R., July 2002. Quantitative comparison and evaluation of two commercially available, two-dimensional electrophoresis image analysis software packages, Z3 and melanie. Electrophoresis 23 (14), 2194–2202.
URL http://dx.doi.org/3.0.CO;2-

Rasband, W., 1997-2009. ImageJ. U. S. National Institutes of Health, Bethesda, Maryland, USA.
URL http://rsb.info.nih.gov/ij/

Rohr, K., 2000. Elastic registration of multimodal medical images: A survey. Künstliche Intelligenz 14 (3), 11–17.

Rohr, K., Cathier, P., Worz, S., 15–18 April 2004. Elastic registration of gel electrophoresis images based on landmarks and intensities. In: Proc. IEEE International Symposium on Biomedical Imaging: Nano to Macro. pp. 1451–1454.

Rohr, K., Stiehl, H. S., Sprengel, R., Beil, W., Buzug, T. M., Weese, J., Kuhn, M. H., 1996. Point-based elastic registration of medical image data using approximating thin-plate splines. In: Höhne, K. H., Kikinis, R. (Eds.), Proceedings of the 4th International Conference on Visualization in Biomedical Computing. Vol. 1131 of Lecture Notes In Computer Science. Springer, pp. 297–306.

Rote, G., May 17 1991. Computing the minimum Hausdorff distance between 2 point sets on a line under translation. Information Processing Letters 38 (3), 123–127.

Rueckert, D., Aljabar, P., Heckemann, R. A., Hajnal, J. V., Hammers, A., 2006. Diffeomorphic registration using B-Splines. In: Larsen, R., Nielsen, M., Sporring, J. (Eds.), Medical Image Computing and Computer-Assisted Intervention - MICCAI 2006. Vol. 4191 of Lecture Notes in Computer Science. Springer, pp. 702–709.

Rueckert, D., Sonoda, L. I., Hayes, C., Hill, D. L. G., Leach, M. O., Hawkes, D. J., 1999. Non-rigid registration using free-form deformations: Application to breast MR images. IEEE Transactions on Medical Imaging 18 (8), 712–721.

Russo, I. H., Russo, J., December 1978a. Developmental stage of rat mammary-gland as determinant of it susceptibility to 7,12-dimethylbenz[a]anthracene. Journal of the National Cancer Institute 61 (6), 1439–49.

Russo, J., Russo, I. H., December 1978b. DNA labeling index and structure of rat mammary-gland as determinants of its susceptibility to carcinogenesis. Journal of the National Cancer Institute 61 (6), 1451–9.

Schmid, B., November 2008. Hardware-accelerated 3D visualization for ImageJ. In: ImageJ User & Developer Conference.

Schormann, T., Dabringhaus, A., Zilles, K., 1995. Statistics of deformations in histology and application to improved alignment with MRI. IEEE Transactions on Medical Imaging 14 (1), 25–35.
URL http://dx.doi.org/10.1109/42.370399

Sethian, J., 1996. A fast marching level set method for monotonically advancing fronts. In: Proceedings of the National Academy of Sciences of the United States of America. Vol. 93. pp. 1591–1595.
URL citeseer.ist.psu.edu/sethian95fast.html

Skouson, M. B., Guo, Q., Liang, Z.-P., 2001. A bound on mutual information for image registration. IEEE Transactions on Medical Imaging 20 (8), 843–846.

Smilansky, Z., May 2001. Automatic registration for images of two-dimensional protein gels. Electrophoresis 22 (9), 1616–1626.
URL http://dx.doi.org/3.0.CO;2-Z

Sorzano, C. O. S., Thévenaz, P., Unser, M., April 2005. Elastic registration of biological images using vector-spline regularization. IEEE Transactions on Biomedical Engineering 52 (4), 652–663.

Sorzano, C. O. S., Thevenaz, P., Valdes, I., Beloso, A., Unser, M., 2006. Elastic image registration with applications to proteomics. In: Cristobal, G and Javidi, B and Vallmitjana, S (Ed.), Information Optics. Vol. 860 of AIP Conference Proceedings. 2 Huntington Quadrangle, STE 1NO1, Melville, NY 11747-4501 USA, pp. 300–309, 5th International Workshop on Information Optics, Toledo, Spain, June 05-07, 2006.

Streicher, J., Donat, M. A., Strauss, B., Spörle, R., Schughart, K., Müller, G. B., June 2000. Computer-based three-dimensional visualization of developmental gene expression. Nature Genetics 25 (2), 147–152.
URL http://dx.doi.org/10.1038/75989

Streicher, J., Weninger, W. J., Müller, G. B., August 1997. External marker-based automatic congruencing: a new method of 3D reconstruction from serial sections. Anatomical Record 248 (4), 583–602.

Szeliski, R., Shum, H.-Y., 1996. Motion estimation with quadtree splines. IEEE Transactions on Pattern Analysis and Machine Intelligence 18 (12), 1199–1210.

Thévenaz, P., Ruttimann, U. E., Unser, M., 1998. A pyramid approach to subpixel registration based on intensity. IEEE Transactions on Image Processing 7 (1), 27–41.

Thirion, J. P., September 1998. Image matching as a diffusion process: an analogy with maxwell's demons. Medical Image Analysis 2 (3), 243–260.

Twining, C., Cootes, T., Marsland, S., Schestowitz, R., Petrovic, V., Taylor, C., 2005. A unified information-theoretic approach to groupwise non-rigid registration and model building. In: Christensen, G., Sonka, M. (Eds.), 19th International Conference on Information Processing in Medical Images (IPMI'05). Vol. 3565 of Lecture Notes in Computer Science. Springer-Verlag, pp. 1–14.

Twining, C., Marsland, S., Taylor, C., 2004. Groupwise non-rigid registration: The minimum description length approach. In: British Machine Vision Conference (BMVC'04).
URL http://www-ist.massey.ac.nz/smarsland/PUBS/BMVC04.pdf

Unser, M., November 1999. Splines: A perfect fit for signal and image processing. IEEE Signal Processing Magazine 16 (6), 22–38, IEEE Signal Processing Society's 2000 magazine award.

Unser, M., Aldroubi, A., Eden, M., 1991. Fast B-spline transforms for continuous image representation and interpolation. IEEE Transactions on Pattern Analysis and Machine Intelligence 13 (3), 277–285.

Unser, M., Aldroubi, A., Eden, M., April 1993. The L_2-polynomial spline pyramid. IEEE Transactions on Pattern Analysis and Machine Intelligence 15 (4), 364–379.

Veeser, S., Dunn, M. J., Yang, G. Z., July 2001. Multiresolution image registration for two-dimensional gel electrophoresis. Proteomics 1 (7), 856–870.
URL http://dx.doi.org/3.0.CO;2-R

Verbeek, F. J., Huijsmans, D. P., Baeten, R. J., Schoutsen, N. J., Lamers, W. H., April 1995. Design and implementation of a database and program for 3D reconstruction from serial sections: a data-driven approach. Microscopy Research and Technique 30 (6), 496–512.
URL http://dx.doi.org/10.1002/jemt.1070300607

Vercauteren, T., Pennec, X., Perchant, A., Ayache, N., 2007. Non-parametric diffeomorphic image registration with the demons algorithm. In: Medical Image Computing and Computer-Assisted Intervention - MICCAI 2007. Vol. 4792 of Lecture Notes in Computer Science. pp. 319–326.

Vollmer, J., Mencl, R., Müller, H., 1999. Improved laplacian smoothing of noisy surface meshes. Computer Graphics Forum 18 (3), 131–138.

Weninger, W. J., Meng, S., Streicher, J., Mï¿œller, G. B., May 1998. A new episcopic method for rapid 3-D reconstruction: applications in anatomy and embryology. Anatomy and Embriolgoy-Berlin 197 (5), 341–348.

Weninger, W. J., Mohun, T., January 2002. Phenotyping transgenic embryos: a rapid 3-D screening method based on episcopic fluorescence image capturing. Nature Genetics 30 (1), 59–65.
URL http://dx.doi.org/10.1038/ng785

Westerlind, K. C., McCarty, H. L., Gibson, K. J., Strange, R., Jun 2002. Effect of exercise on the rat mammary gland: implications for carcinogenesis. Acta Physiol Scand 175 (2), 147–156.

Wirtz, S., Fischer, B., Modersitzki, J., Schmitt, O., February 2004. Superfast elastic registration of histologic images of a whole rat brain for three-dimensional reconstruction. In: Medical Imaging 2004: Image Processing. Proceedings of the SPIE.

Wirtz, S., Papenberg, N., Fischer, B., Schmitt, O., February 2005. Robust and staining-invariant elastic registration of a series of images from histologic slices. In: Medical Imaging 2005: Image Processing. Vol. 5747 of Proceedings of the SPIE. pp. 1256–1262.

Wiseman, B. S., Sternlicht, M. D., Lund, L. R., Alexander, C. M., Mott, J., Bissell, M. J., Soloway, P., Itohara, S., Werb, Z., September 2003. Site-specific inductive and inhibitory activities of MMP-2 and MMP-3 orchestrate mammary gland branching morphogenesis. Journal of Cell Biology 162 (6), 1123–1133.
URL http://dx.doi.org/10.1083/jcb.200302090

Woods, R. P., Grafton, S. T., Watson, J. D., Sicotte, N. L., Mazziotta, J. C., 1998. Automated image registration: Ii. intersubject validation of linear and nonlinear models. Journal of Computer Assisted Tomography 22 (1), 153–165.

Xiao, G., Brady, J. M., Noble, J. A., Burcher, M., English, R. E., 2002. Non-rigid registration of 3-D free-hand ultrasound images of the breast. IEEE Transactions on Medical Imaging 21 (4), 405–412.

Xie, Z., Farin, G. E., 2004. Image registration using hierarchical B-splines. IEEE Transactions on Visualization and Computer Graphics 10 (1), 85–94.

Yagou, H., Belyaev, A. G., Weiz, D., 2002. Mesh median filter for smoothing 3-D polygonal surfaces. In: Proceedings of the First International Symposium on Cyber Worlds. IEEE Computer Society, pp. 488–498.

Yushkevich, P. A., Avants, B. B., Ng, L., Hawrylycz, M., Burstein, P. D., 0005, H. Z., Gee, J. C., 2006. 3D mouse brain reconstruction from histology using a coarse-to-fine approach. In: Pluim et al. (2006), pp. 230–237.

Zhang, Z., 1993. Point matching for registration of free-form surfaces. In: Chetverikov, D., Kropatsch, W. G. (Eds.), Computer Analysis of Images and Patterns. Vol. 719 of Lecture Notes in Computer Science. Springer, pp. 460–467.

Zheng, G., Zhang, X., Jonic, S., Thévenaz, P., Unser, M., Nolte, L.-P., 2006. Point similarity measures based on MRF modeling of difference images for spline-based 2D-3D rigid registration of X-Ray fluoroscopy to CT images. In: Pluim et al. (2006), pp. 186–194.

Zitová, B., Flusser, J., 2003. Image registration methods: a survey. Image and Vision Computing 21 (11), 977 – 1000.
URL http://www.sciencedirect.com/science/article/B6V09-49D25S6-3/2/b95e1823beee3564404b565b95dc8770

Nomenclature

BFGS Broyden-Fletcher-Goldfarb-Shanno

CPR Consistent Pairwise Registration

CSR Consistent Sequential Registration

CT Computed Tomography

CT Computed Tomography

CTR Consistent Tri-wise Registration

ER Estrogen Receptor

H&E Hematoxylin and Eosin

HCMA Hierarchical Chamfer Matching Algorithm

MRI Magnetic Resonance Imaging

MRI Magnetic Resonance Imaging

PCM Phase Correlation Method

PET Positron Emission Tomography

PET Positron Emission Tomography

PR Progesterone Receptor

TEM Transmission Electron Microscope

TPS Thin-plate splines

UER Unidirectional Elastic Registration

UPR Unidirectional Pairwise Registration

VDD Vercauteren's Diffeomorphic Demons